



Ludwig-Maximilians-Universität München

Masterarbeit an der Fakultät für Physik

**Studies on Velocity Measurements with the
ATLAS Calorimeters for the Search for Heavy
Long-Lived Particles**

**Studien zur Geschwindigkeitsmessung mit den
ATLAS Kalorimetern für die Suche nach
schweren langlebigen Teilchen**

vorgelegt von

Michael Adersberger

geboren in Prien am Chiemsee

München, den 22.06.2015

Abstract

An interesting target for model independent searches for new particles with the ATLAS experiment at the Large Hadron Collider are stable massive particles. Stable massive particles are expected to be produced with velocities significantly lower than the speed of light. The velocity is therefore a good discriminator between exotic and Standard Model particles, as these are produced with almost the speed-of-light. One sub-detector suitable for the measurement of velocities with a Time-of-Flight method is the ATLAS tile calorimeter. Several improvements on the β measurement are presented and the resolution could be improved by 17%. The influence of the improved β estimation on a search for stable massive particles is tested by revising a previous search for stable R -hadrons [1]. For this analysis $\int Ldt = 18.8 \text{ fb}^{-1}$ of data taken at a center-of-mass energy $\sqrt{s} = 8 \text{ TeV}$ are used. No excess over the expected background is found for all considered signal regions. The results are used to set an upper limit on the production cross section of sparticles at a Confidence Level of 95%. Comparing this with the theoretical predicted cross sections a lower limit on the mass of gluinos, sbottoms and stops can be estimated. The mass limits obtained are 1241 GeV for gluinos, 800 GeV for stops and 760 GeV for sbottoms.

Zusammenfassung

Die Suche nach langlebigen stabilen Teilchen mit dem ATLAS Detektor am Large Hadron Collider ist vielversprechend, da sie modellunabhängig ist. Es wird erwartet, dass schwere stabile langlebige Teilchen mit deutlich niedrigeren Geschwindigkeiten als der Lichtgeschwindigkeit produziert werden. Man kann daher die Geschwindigkeit benutzen, um exotische Teilchen von Standard Modell Teilchen zu unterscheiden, da diese mit annähernd Lichtgeschwindigkeit produziert werden. Das ATLAS Tile Kalorimeter kann genutzt werden, um anhand einer Flugzeitmessung die Geschwindigkeit der Teilchen zu bestimmen. Mehrere mögliche Verbesserungen für die Geschwindigkeitsmessungen mit dem Tile Calorimeter werden in dieser Arbeit vorgestellt, welche die Geschwindigkeitsmessung insgesamt um 17% verbessern. Die Auswirkungen dieser Verbesserungen auf die Suche nach stabilen Teilchen wird getestet, indem eine bestehende Suche nach schweren stabilen R -Hadronen mit den eingebauten Korrekturen wiederholt wird. Für diese Analyse wird ein $\int L dt = 18.8 \text{ fb}^{-1}$ an Daten verwendet, die bei einer Schwerpunktsenergie von $\sqrt{s} = 8 \text{ TeV}$ aufgenommen wurden. Es wurden keine Hinweise auf neue Teilchen gefunden. Die Ergebnisse werden verwendet, um eine obere Grenze auf den Wirkungsquerschnitt der betrachteten Teilchenmodelle auf dem 95% Konfidenzniveau zu setzen. Vergleicht man diese mit dem vorhergesagten theoretischen Wirkungsquerschnitten, so kann eine untere Grenze für die Masse der jeweiligen Teilchen errechnet werden. Die unteren Grenzen für die Massen der betrachteten Teilchen, die sich aus dieser Analyse ergeben, sind: 1241 GeV für Gluinos, 800 GeV für Stops und 760 GeV für Sbottoms.

Contents

1	Introduction	1
2	Theoretical Motivation	3
2.1	Standard Model of Particle Physics	3
2.1.1	Description of the Standard Model	3
2.1.2	Motivation for Theories Beyond the Standard Model	4
2.2	Beyond Standard Model Theories	7
2.2.1	Supersymmetry	7
2.2.2	Universal Extra Dimensions	9
2.3	Long-lived Particles	9
2.3.1	Lifetime in Quantum Field Theories	10
2.3.2	Longevity of Particles	11
2.3.3	Examples for Long-Lived Particles	12
2.4	Summary	14
3	The Experiment	15
3.1	Experimental Setup	15
3.1.1	The Large Hadron Collider	15
3.1.2	The ATLAS Detector	18
3.2	Production and Interaction of Long-Lived Particles	20
3.2.1	Production	20
3.3	Signatures of Particles in the Detector	23
3.3.1	Standard Model Particles	23
3.3.2	Heavy Long-Lived Particles	25
3.4	Observables for the Search for Stable Massive Particles	27
3.4.1	Energy-loss	27
3.4.2	Time-of-Flight	30
3.5	Summary	34

4	Search for Stable Massive Particles	35
4.1	Data and Simulated Event Samples	35
4.1.1	Data Event Samples	35
4.1.2	Simulated Samples	36
4.2	Studies on β Estimation	38
4.2.1	$Z \rightarrow \mu\mu$ candidate selection	38
4.2.2	Cell-Time Smearing	38
4.2.3	Cell-Time Correction	41
4.2.4	Dimension Correction	45
4.2.5	Distance Corrected Smearing	54
4.2.6	Primary Vertex Shift Correction	55
4.2.7	Cell Time Uncertainty	56
4.2.8	Cell-Time Calibrations	59
4.2.9	Liquid Argon Calorimeter β estimation	61
4.2.10	Summary	61
4.3	Muon Agnostic Analysis	63
4.3.1	Event Selection	63
4.3.2	Candidate Pre-selection	64
4.3.3	Final Selection	67
4.3.4	Background Estimation	69
4.3.5	Systematic Uncertainties	72
4.3.6	Results and Interpretation	75
5	Conclusion and Outlook	81
5.1	Conclusion	81
5.2	Outlook	82

Chapter 1

Introduction

The aim of physics is to describe nature with quantitative models and regularities. One of the best empirically validated models in physics is the Standard Model (SM) of particle physics. The SM was able to predict several particles before their actual discovery. The last piece of the particle puzzle predicted by the SM was discovered in 2012, the Higgs boson [2]. So far everything seems to work fine, but the SM has several issues. For example it is not possible to construct a consistent Quantum Field Theory (QFT) of gravitation. So the question is, what comes next? Most theories addressing the limitations of the SM predict new particles. But as no evidence for particles beyond the SM was found so far, plenty of new theories arise. This leads to a need for model independent searches. One model independent search covering a wide range of new theories is the search for heavy Long-Lived Particles (LLP).

The searches described in this thesis were performed with data from the ATLAS experiment at the Large Hadron Collider (LHC) in Geneva, Switzerland. One particular scenario of heavy LLPs are Stable Massive Particles (SMP), which have lifetimes sufficiently large to traverse the whole detector. An important property of SMPs is, that they are expected to be produced with significantly lower velocities than the speed of light. As all SM particles are produced almost with the speed-of-light, the velocity is a suitable discriminator between SMPs and SM particles. One subsystem of the ATLAS detector suitable for velocity measurements with the Time-of-Flight (ToF) method is the ATLAS Tile Calorimeter (TileCal).

Several studies on the improvement of the velocity measurement with the TileCal are presented. A method suggested in Ref. [3] is tested to correct for a bias for large values of the estimated time measured with the TileCal. The TileCal is segmented into cells, which have quite large dimensions. In previous searches the center of the cell was used to measure the distance in the ToF method. I developed a method that uses the length of the track in the cell to reconstruct the actual position for the time measurement. This is compared with a fit method described

in Ref. [3]. Furthermore the distance correction can be used to correct the cell time to be measured at the same distances from the interaction point for each TileCal cell. The influence on the smearing of the time is tested, which is necessary to have a good agreement between Monte Carlo simulated events and data. Also the influence on the parametrization of the uncertainty of the measured time as a function of energy deposit in the cell is studied. Including the z_0 position of the particle tracks in the distance correction is tested. The influence of the suggested methods on the timing calibration used in previous searches for SMPs is discussed. Furthermore a study on velocity measurements including the Liquid Argon (LAr) calorimeters is presented. The influence of the corrected β estimation on the searches for SMPs is tested by redoing a published search for stable R -hadrons [1].

Chapter 2

Theoretical Motivation

This chapter is a short summary of the main theoretical motivations for the search for long-lived particles. The first section describes the Standard Model of particle physics and the need for physics beyond. There is a large variety of theories trying to solve the issues of the SM. Many of these theories predict LLPs. Supersymmetry (SUSY), as the most prominent example and Universal Extra Dimensions (UED), as a further example, are discussed in the second part. The last section gives a definition of longevity in the context of particle physics. Also some examples of LLPs in the SM as well as in theories Beyond the Standard Model (BSM) are given.

2.1 Standard Model of Particle Physics

2.1.1 Description of the Standard Model

The SM is a Quantum Field Theory, in which the particles are described by the according fields. The particles of the SM can be divided into three groups: Quarks, which are the constituents of the hadrons e.g. protons or neutrons; Leptons, e.g. electrons or neutrinos; and the gauge bosons as mediator particles of the forces, e.g. photons. Furthermore each lepton or quark has an anti-particle which has the same mass but differs in all charge-like quantum numbers by a factor of minus one. The quarks and leptons can be divided into three generations. For the quarks each generation consists of an up- and a downtype particle with charge $2/3 e$ and $-1/3 e$, respectively. Each lepton generation is formed from a charged particle e.g. e^- and an uncharged inherent neutrino e.g. ν_e . The particles of the higher generations can be seen as a high mass copy of the particles of the lower generation.

One important mathematical principle of the SM is, that the forces occur in the theory due to gauge symmetries. Each gauge symmetry comes together with at least one particle as mediator of the force. For the

$SU(3) \times SU(2) \times U(1)$ symmetry of the SM, the according particles are the photon, the Z and W^\pm bosons for the electro weak interaction and the gluons for the strong interaction. Important conserved quantum numbers are electric charge, weak isospin and color. The color quantum number is only carried by quarks and gluons, whereby gluons carry two colors. In measurements no unbound colored particles have been observed. To accomplish this in the theory the quark confinement was introduced. The quark confinement predicts, that observable particles are colorless or bound in hadrons with no overall color¹.

The last piece of the SM puzzle is the Higgs boson. This particle arises from the Higgs mechanism, which enables a mass term for the gauge bosons of the weak interaction through a spontaneous symmetry breaking of the Higgs field. The leptons and quarks obtain their mass through a Yukawa coupling to the Higgs field. A theoretical explanation of the Higgs mechanism and the SM of particle physics can be found in Ref. [4]. The particle content of the SM is summarized in Tab. 2.1. From now on the usual convention in particle physics $c = \hbar = 1$ will be used.

¹The color quantum number is represented by the three colors red, blue and green. A combination of all three colors leads to colorlessness as well as a color and an anti-color.

Name	Label	Mass [MeV]	Charge [e]	Color
Leptons				
Electron	e	0.511	-1	-
Electron-neutrino	ν_e	$< 2 \cdot 10^{-6}$	0	-
Muon	μ	105.66	-1	-
Muon-neutrino	ν_μ	< 0.2	0	-
Tauon	τ	1776	-1	-
Tauon-neutrino	ν_τ	< 18	0	-
Quarks				
Up	u	2	2/3	r,g,b
Down	d	5	-1/3	r,g,b
Charm	c	1275	2/3	r,g,b
Strange	s	95	-1/3	r,g,b
Top	t	$173 \cdot 10^3$	2/3	r,g,b
Bottom	b	$4 \cdot 10^3$	-1/3	r,g,b
Gauge bosons				
Gluon	g	0	0	(r,g,b) $\times 2$
Photon	γ	0	0	-
W	W^\pm	80385	± 1	-
Z	Z^0	91188	0	-
Higgs	H	$126 \cdot 10^3$	0	-

Table 2.1: The particle content of the SM with mass, charge and color of the particles, taken from Ref. [5]. The anti-particles differ by opposite sign in all charge like quantum numbers.

2.1.2 Motivation for Theories Beyond the Standard Model

The SM represents one of the best empirically proven theories so far. It for example predicted the existence of W and Z bosons, gluon, top and charm quarks before their discovery. But the SM has nevertheless some issues discussed in the following :

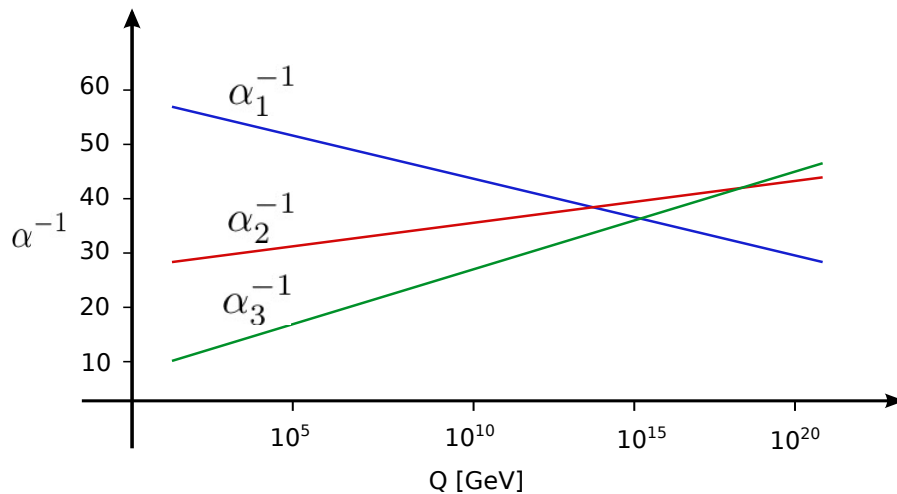


Figure 2.1: The extrapolation of the coupling constants to the scale of GUT for the energy transfer in an interaction. It can be seen that the different couplings do not intersect in one point.

Gravitation

Including gravitation, described by the general relativity, in the SM is not possible. The reason for that is, that it is not possible to formulate a consistent QFT of gravitation. Thus it is not possible to easily merge the empirically well proven theory at large scales, the general relativity, and the empirically well proven theory at small scales, the SM of particle physics.

Baryon Asymmetrie

Assuming that we are at no prominent place in the Universe, the laws of nature on earth are equal to the laws of nature anywhere else. The observation, that everything surrounding us is built of matter, not anti-matter, leads to the assumption, that matter is dominant in the whole universe. This is in conflict with the natural assumption that the universe is neutral within all conserved charges and that the Big Bang produced equal amounts of matter and anti-matter. The solution would be charge parity violating processes out of the thermal equilibrium². These processes occur in the SM, but are by orders of magnitude too weak to explain the measured baryon asymmetry in the Universe.

²These conditions are called Sakharov conditions [6].

Unification of Forces

The aim of a Grand Unified Theory (GUT) is to merge the EM, weak and strong interaction into one force at a high energy-transfer scale (GUT scale) described by a single GUT symmetry. The larger GUT symmetry is at a lower scale spontaneously broken to the $SU(3) \times SU(2) \times U(1)$ group of the SM. This larger GUT symmetry can be described with a unified coupling constant. But this is not realized within the SM, because the SM couplings do not intersect in one point, as illustrated in Fig. 2.1. The

motivation for a unification of forces is, that EM and weak interaction are already described with the Electroweak theory. The unification would further reduce the free parameters of the SM and automatically predict the quantization of the electric charge.

Dark Matter

The standard model of cosmology provides several predictions for the Universe. For example the existence of the cosmic microwave background or the expansion of the Universe. These predictions are empirically well proven and give a high evidence to this theory. Furthermore from measurements a prediction on the composition of energy in the Universe can be given: Dark energy (69.2 %), dark matter (26.0 %) and SM matter (4.8 %) [7]. Dark energy is not understood and there is no commonly accepted theory, explaining it. Slightly better is the understanding of dark matter, as the interactions with observable matter give hints for the presence of dark matter, e.g. in gravitation lens effects or in the motion of galaxies. This gives an idea of dark matter consisting of massive particles interacting only weakly (weakly interacting massive particles WIMPs). But also for dark matter no commonly accepted theory exist. Merely five percent of the Universe consists of known matter described by the SM of particle physics.

Fine-tuning

The Higgs mass in the SM is given by

$$m_h^2 = m_0^2 - \frac{|\lambda_f|^2}{8\pi^2} \Lambda^2 + \mathcal{O} \left(\ln \frac{\Lambda^2}{m_f^2} \right). \quad (2.1)$$

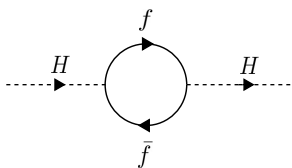


Figure 2.2: First order quantum loop correction Feynman diagram of a virtual fermion f to the Higgs boson H .

The second term represents a first order quantum loop correction, displayed in Fig. 2.2. The corrections to the Higgs mass are of the order Λ^2 . Λ represents the renormalization cut-off scale, the scale at which the validity of the theory ends. This is usually set to the GUT scale, which is of the order 10^{16} GeV [5]. For the observed Higgs mass at 126 GeV, m_0^2 and the quantum loop correction have to cancel each other to more than 20 digits exact, which is found to be an unnatural fine-tuning.

There are also further issues of the SM, which will be not further described here. The intention of this section was mainly to justify the need for BSM theories, although the SM represents an empirically well proven theory.

2.2 Beyond Standard Model Theories

This section describes BSM theories, which are of particular interest for the search for LLPs. The first part is on SUSY as the most prominent theory beyond the SM. Also UED are introduced as a further BSM example. There are other BSM models predicting LLPs, e.g. magnetic monopole [8] or Q-ball [9], but, as the searches for LLPs are model independent, only these two examples are discussed here. A detailed description of interesting BSM theories in the context of LLPs is given in Ref. [10].

2.2.1 Supersymmetry

SUSY is the best understood concept in BSM theories so far and is favored by most theorists, because it implies solutions for some of the previously mentioned issues of the SM. The only, but probably worst, problem is, that nature does not seem to favor it, as no evidence for the according SUSY particles was found so far.

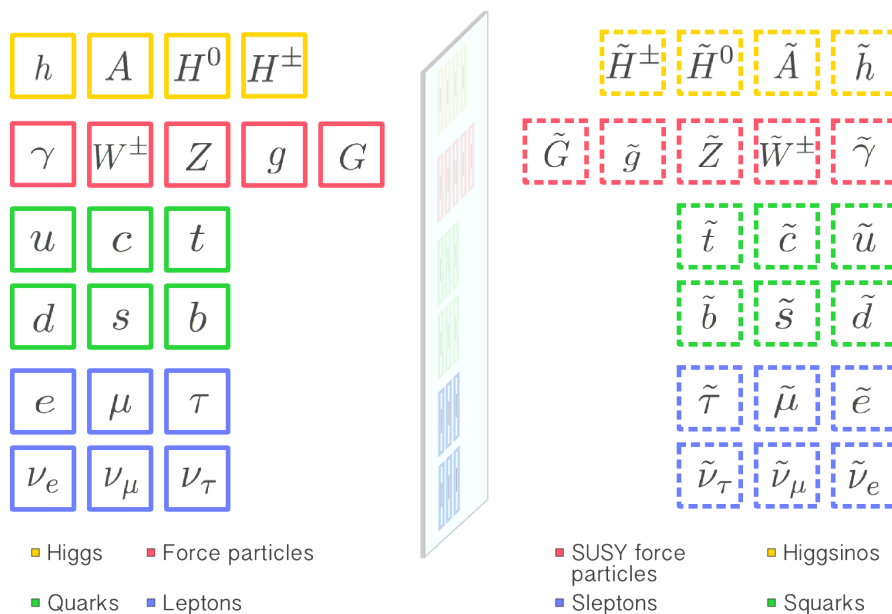


Figure 2.3: Particle content of the Minimal Supersymmetric Standard Model (MSSM).

SUSY is a hypothetic new symmetry, which allows a transformation between fermions and bosons. Each fermion/boson builds a supermultiplet with a bosonic/fermionic superpartner. The superpartners have equal mass and quantum numbers. The bosonic partners of the fermions are labeled with an "s" in front of the name, e.g. sbottom. Whereas the fermionic superpartners of the bosons get an "ino" at the end, e.g. "higgsino". The symbols of the sparticles all carry a " $\tilde{\sim}$ " above, e.g. the higgsino \tilde{h} . A minimum of twice the SM particles would be predicted by a supersymmetric SM. The interaction eigenstates of the superpartners of the gauge and Higgs fields are able to mix with each other to the observable mass

eigenstates. The charged mass eigenstates are called charginos, whereas the uncharged are called neutralino. Furthermore, additional particles in the Higgs sector are needed to obtain mass terms for all fermions. For the Minimal Supersymmetric Standard Model (MSSM) five Higgs bosons are needed.

The interaction eigenstates of the MSSM are shown in Fig. 2.3. One issue being solved in a supersymmetric model is the fine tuning problem. The loop corrections to the bare Higgs mass of the fermions are canceled by the loop corrections of their bosonic superpartners and vice versa. The Feynman graphs for these processes are shown in Fig. 2.4. The correction term for a fermion is given by

$$\Delta m_H^2 = \frac{\lambda_f^2}{16\pi^2} [-2\Lambda^2 + 6m_f^2 \ln(\Lambda/m_f)]. \quad (2.2)$$

Whereas the correction term of a boson is given by Eq. 2.3.

$$\Delta m_H^2 = \frac{\lambda_b}{16\pi^2} [2\Lambda^2 - 6m_b^2 \ln(\Lambda/m_b)] \quad (2.3)$$

For the coupling constants, $\lambda_f^2 = \lambda_b$ holds due to the symmetry between bosons and fermions. For the case of an unbroken SUSY the masses of the particles and sparticles are equivalent, thus the correction terms would perfectly cancel. As previously mentioned no direct experimental evidence for SUSY particles was found so far. This means that the masses have to differ. The solution is to require SUSY to be broken. This symmetry breaking can be spontaneous as in the Higgs sector, but there are also other possibilities, especially if gravity is included. In a broken SUSY, the masses of the supersymmetric partners are at a scale $\Lambda_{SUSY} > \Lambda_{weak}$. This leads to a remaining contribution of the loop corrections to the Higgs mass given by

$$\Delta(m_H^2) = \mathcal{O}\left(\frac{\alpha}{4\pi}\right) |m_b^2 + m_f^2|. \quad (2.4)$$

It can be concluded, that the mass difference between particles and sparticles should not be too large to still solve the unnaturalness of the fine-tuning. The masses of the sparticles should therefore not be larger than a few TeV. Thus if SUSY is a basic feature of nature, new particles should have masses reachable for modern accelerators.

In principle lepton/baryon numbers are violated in SUSY models, what is in conflict with the observation of a stable proton. To accomplish stability for the proton R -parity conservation can be required. R is defined by Eq. 2.5.

$$R = (-1)^{3B+L+2S}, \quad (2.5)$$

where B is the baryon number, L the lepton number and S the spin of the particle. Thus SM particles carry $R = +1$, whereas SUSY particles

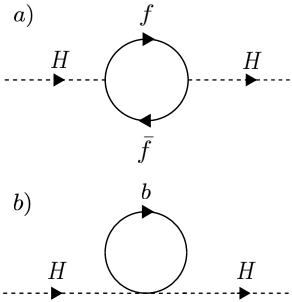


Figure 2.4: Loop corrections to the Higgs mass from a fermion (a) and a boson (b).

carry $R = -1$. If R -parity is conserved the proton is stable and also the lightest supersymmetric particle (LSP). If the LSP is uncharged, it is a good candidate for dark matter.

By defining SUSY as a local symmetry gravitation can be introduced with the graviton as mediator. But still the problem of a consistent formulation of the quantum gravitation remains. A further issue of the SM that could be solved within a SUSY model is the baryon asymmetry. The reason for that is, that strong CP violation could arise in the SUSY sector. Furthermore also the unification of the coupling constants could be realized due to the influence of the sparticles at the TeV scale. All in all, SUSY is a promising concept in BSM theories, which is able to solve many issues of the SM. On the other hand it has to be mentioned, that a broken SUSY results in 105 free parameters. These can be reduced in constrained scenarios, but it still states an enormous parameter space for new theories. A detailed description of SUSY can be found for example in Ref. [11].

2.2.2 Universal Extra Dimensions

With the introduction of a fourth or even fifth space-like dimension for the fields of the SM, it is possible to unify gravitation and gauge theories, though quantum gravitation still remains inconsistent. All observations until now predict only three space-like and one time-like dimension. This can be solved with the introduction of compactification [12]. Compactification means that the extra dimension are microscopically curled up and were thus not observable so far. A catchy analogue is the observation of a straw from a big distance. From this point of view the straw looks like a line. Only with the observation from a sufficient near distance the differentiation between a straw and a line is possible. The particles can be explain as standing waves on the compactified extra dimensions. This leads to the Kaluza-Klein (KK) tower of possible discrete mass eigenstates. Furthermore momentum conservation in the extra dimension introduces the conserved KK quantum number stating the excitation level. To obtain the chiral SM with zero modes, KK number violation by loop effects is allowed, but a KK parity still remains. This leads to a lightest KK particle as good candidate for dark matter. For further information see Ref. [13].

2.3 Long-lived Particles

To understand the meaning of long-lived in the context of particle physics, this section first describes the meaning of lifetime. Also the calculation of lifetime with the equations of QFT will be briefly described. In the

second part a recipe to identify long-lived particles in the SM as well as in not too exotic³ BSM theories will be presented. Finally some examples for LLPs in the SM as well as in BSM theories are given.

³This recipe breaks if fundamental laws of physics are broken e.g. energy conservation.

2.3.1 Lifetime in Quantum Field Theories

From the macroscopic world it would be assumed that lifetime is something well determined. So if there is a unstable fundamental particle at rest it will decay after a time t . But this is not the case, the decay of particles has an intrinsically random element. The lifetime has to be defined as a mean lifetime of the particle. The number N of remaining particles of one type after a period of time dt can be calculated with Eq. 2.6. This is statistical interpretation and thus only holds for a large number of particles N . The decay rate (or width) Γ is the probability per unit time that a particle will decay.

$$dN = -\Gamma N(t)dt \quad (2.6)$$

By solving this differential equation, the number of remaining particles is given by

$$N(t) = N_0 e^{-\Gamma t}. \quad (2.7)$$

The mean lifetime τ , as the subject of interest, is given as the reciprocal of the decay rate

$$\tau = \frac{1}{\Gamma}. \quad (2.8)$$

The total decay width is given as the sum over all allowed decays

$$\Gamma_{tot} = \sum_{i=1}^n \Gamma_i. \quad (2.9)$$

The decay width can be calculated with the relativistic form of Enrico Fermi's Golden Rule for decays Eq. 2.10, which is taken from Ref. [4].

$$\Gamma = \frac{S}{2\hbar_1} \int |\mathcal{M}|^2 (2\pi)^4 \delta(p_1 - p_2 - p_3 - \dots - p_n) \times \prod_{j=2}^n 2\pi \delta(p_j^2 - m_j^2 c^2) \theta(p_j^0) \frac{d^4 p_j}{(2\pi)^4} \quad (2.10)$$

This equation can be split in two parts: On the one hand the amplitude \mathcal{M} , which describes all dynamical information of the processes. It can be obtained by the calculation of the according Feynman diagrams. On the other hand the integration over all possible phase space states of all participants. This part is purely kinematic and represents the fact that a process is more likely, if it has larger phase space for possible final states. The contributions of the QFT used are thus mainly to the amplitude.

2.3.2 Longevity of Particles

A particle is defined to be long-lived, if the mean lifetime of the particle is sufficient to be directly detected with the detector. This means, that the lifetime has to be long enough to produce at least a displaced vertex. In this context it is essential that in high energy physics the particles are produced with high momenta which includes that relativistic effects have to be considered. The lifetime t_0 is then elongated by the time dilation

$$t = t_0\gamma, \quad (2.11)$$

where

$$\gamma = \frac{1}{\sqrt{1 - \beta^2}} \text{ and } \beta = \frac{v}{c}. \quad (2.12)$$

The ATLAS inner detector is able to reconstruct displaced vertices with a minimum radial distance $c\tau = 1$ mm [14]. For particles decaying at rest this corresponds to a lifetime of about 3 ns. We adopt $t_0 \geq 3$ ns as criterion for LLPs. The spectrum of LLPs also includes particles that have lifetimes sufficient to pass the hole detector. These particles are called stable, although some of them may decay after leaving the detector.

There are several reasons for long lifetime acting mainly as a combination.

- Lightest particle with a (almost) conserved quantum number
- Few decay channels
- Heavy intermediate particle(s)
- Soft coupling to lighter particles
- (Almost) mass degenerated with decay products

The decay of the lightest particle LP with a conserved quantum number is not possible or strongly suppressed for an almost conserved quantum number. The reason for that is quantum number and energy conservation. A hypothetically decay into a heavier particle would result in a mass/energy gain. Also few decay channels can contribute to a long lifetime of a particle, because the decay width is the sum over all decay channels Eq. 2.9. Considering this, a good candidate for a LLP in a BSM theory is always the second lightest particle with a conserved quantum number, as it could only decay into the LP. A further reason for longevity could be the decay over a heavy intermediate particle. The according Feynman diagram is illustrated in Fig. 2.5. In the case, that the mass of the intermediate particle exceeds the mass difference between particles A and B , the process should be forbidden. This is not the case, because the intermediate particle is not permanent existent and hence

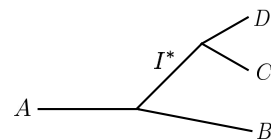


Figure 2.5: Feynman diagram for a toy theory decay of a particle A into the particle B , C and D over a virtual heavy intermediate particle I^* .

able to get energy from the vacuum for a short period of time due to the time-energy uncertainty

$$\Delta t \Delta E \geq \frac{1}{2}. \quad (2.13)$$

The more energy the particle has to "borrow" from the vacuum, the less likely becomes the process. In a BSM theory this can be realized especially if there is a huge mass gap between the new particles. A soft coupling to the decay products minimizes the matrix element in Eq. 2.10, what states another reason for long lifetime. This indicator gets particularly important, if the gravitation and the according graviton arise in the new theory, because of the orders of magnitude lower strength of the gravitation Tab. 2.2. The last hint for longevity, is an (almost) mass degenerated state with its decay products. A (almost) mass degenerated state means, that (almost) no energy remains for the momenta of the decay products. This leads to a small phase space for the integration in Eq. 2.10 contributing to a long lifetime of the particle. The focus in BSM theories is again on the second lightest particle with a (almost) conserved quantum number. If this particle is almost mass degenerated with the LP, it would have a long lifetime.

In conclusion, a long lifetime of particles arises in QFTs because of the combination of several different reasons.

Force	Strength
Strong	10
EM	10^{-2}
Weak	10^{-13}
Gravitation	10^{-42}

Table 2.2: The strength of the forces is only a rough estimate given in Ref. [4]. In general their strength is dependent on the distance between the sources and their nature.

2.3.3 Examples for Long-Lived Particles

Standard Model

Long lifetime of particles is nothing unknown, because also the SM includes several particles which have lifetimes sufficient to be counted as LLPs. Following the recipe leading to long lifetime given above, some examples in the SM will be presented.

The electron is a good example for the lightest particle with a conserved quantum number, the lepton number. The electron is thus stable. A further example for longevity in the SM is the muon. As it is the second lightest particle it should naively decay relatively instantaneous to the electron. But the lifetime of the muon is quite long, $2.196 \cdot 10^{-6}$ s. The long lifetime arises, because the only decay channel, the decay to an electron plus neutrinos Fig. 2.6, is strongly suppressed. In principle also decays of the W boson to quarks would be possible, but the mass of the lightest hadronized particle, the pion, is higher than the muon mass. The hadronic decaying channels are thus kinematically forbidden. The decay to the electron is suppressed due to the soft coupling to the W boson as an interaction particle of the weak force and the high mass of the virtually produced W boson.

Also in the baryonic sector long lifetime occurs in the SM. The lightest particle with a conserved quantum number here is the proton and thus

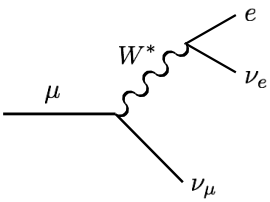


Figure 2.6: Feynman diagram of the decay of a muon into an electron over a virtual W^* boson.

stable. Again the second lightest particle with the conserved quantum number, the neutron, has a long lifetime. The only kinematically allowed decay of the neutron is the beta decay into a proton, an electron and an electron neutrino, the according Feynman diagram is shown in Fig. 2.7. This decay channel is again suppressed due to the high mass of the W boson and the soft coupling of the weak interaction. It is further suppressed due to the small mass difference between the neutron (939.6 MeV) and the proton (938.3 MeV), leading to a 10^9 times longer lifetime compared to the muon.

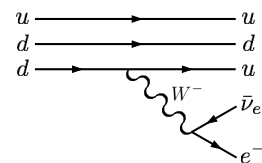


Figure 2.7: Feynman diagram of a β decay of a neutron.

Name	Label	Charge [e]	Lifetime [s]
Stable			
Electron/Positron	e	± 1	∞
(Anti-)Proton	p	± 1	∞
(Anti-)Neutrino	ν_i	0	$\infty?$
Photon	γ	0	∞
Metastable			
Neutron	n	0	880.1
(Anti-)Muon	μ	± 1	$2.2 \cdot 10^{-6}$
Long-lived neutral Kaon	K_L^0	0	$5.1 \cdot 10^{-8}$
Charged Pion	π^\pm	0	$2.6 \cdot 10^{-8}$
Charged Kaon	K^\pm	± 1	$1.2 \cdot 10^{-8}$

Table 2.3: Lifetimes of selected SM particles taken from Ref. [5].

A summary of the stable and metastable particles of the SM, with a lifetime sufficient to be counted as LLPs for searches with the ATLAS detector is shown in Tab. 2.3.

Supersymmetry

The SUSY parameter space offers a wide range of possible scenarios. Many of these scenarios predict long-lived particles. Particular scenarios of interest are those offering a charged LLP, as they produce clear signatures in the detectors. The reference models used for the analysis Sec. 4.3 are scenarios with a sbottom, a stop or a gluino as long lived particle. These arise as R -hadrons due to the color confinement. R -hadrons are squarks or gluinos which hadronize with SM particles. In scenarios with a $\tilde{\chi}_1^0$ as lightest supersymmetric particle (LSP) and dark matter candidate, a sbottom or a stop can be the next-to-lightest supersymmetric particle (NLSP). If the mass difference between the LSP and the NLSP is small enough, the NLSP can mimic the neutron in the SM and thus have a long lifetime.

The scenario for a long-lived gluino is the Split-Supersymmetry [15], where the masses of the scalars, except the ordinary Higgs, are at a high mass scale⁴, whereas the gluino mass stays at the weak scale, illustrated in Fig. 2.8. As the gluinos only couple to colored particles they only decay over a virtual internal squark. This scenario is similar to the muon

⁴The hierarchy problem is not solved in such a scenario.

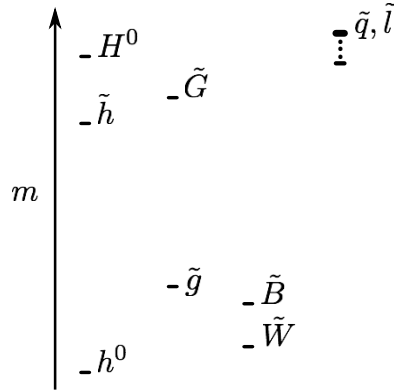


Figure 2.8: Qualitative mass spectrum of a Split-Supersymmetry scenario. The mass of the gluino is in the low mass region, whereas the squarks are in the high mass region.

in the SM and thus strongly suppressed due to the large mass difference between the gluino and the squark.

Universal Extra Dimensions

In the simplest scenarios of UED the Kaluza-Klein modes are basically high mass copies of the SM particles. Therefore KK modes of the lightest SM particles could be long lived. Also further scenarios should be considered where boundary terms in the extra dimensions are allowed. These terms can be treated as free parameters of the theory. This leads to further scenarios for long-lived particles, e.g. a stable graviton as lightest KK particle and a long-lived next-to-lightest particle due to the soft coupling strength of the gravitation.

2.4 Summary

In conclusion this chapter motivated the need for a theory beyond the SM. As no further particles have been observed so far, a large variety of possible new theories evolves. This leads to a need for model independent searches. A good target for such a search are LLPs as they arise in a wide range of theories in a large parameter space. It was further motivated that the new particles have high masses, which should be within the reach of the LHC as the most powerful particle collider so far.

Chapter 3

The Experiment

This chapter describes the Large Hadron Collider (LHC) with the ATLAS experiment. This is followed by a discussion of the production of heavy LLPs at the LHC. The signatures of SM particles as well as different signatures of heavy LLPs in the detector will be presented in the third section. The last section introduces important observables for the search for heavy charged LLPs. A description of the energy-loss measurement with the ATLAS pixel detector is given. Furthermore the time-of-flight measurement and the according timing extraction from the calorimeter signal is presented.

3.1 Experimental Setup

3.1.1 The Large Hadron Collider

To be able to discover hypothetical new particles with masses higher than those of SM particles, an accelerator colliding particles with an enormous energy at a gigantic rate is needed. The high energy is needed to produce the high-mass particles, whereas the rate is needed to compensate the lower cross sections for higher momentum transfers. The LHC, as the most powerful accelerator so far, is able to handle these challenges.

The LHC is a synchrotron situated in the 26.7 km tunnel of the previous Large Electron Positron Collider (LEP) near Geneva, Swiss. LEP was due to the high synchrotron radiation of the electrons/positrons not able to reach energies needed for the current searches for new particles. The LHC is a proton-proton collider. This enables the design for a 14 TeV center-of-mass energy in the proton-proton system, due to the lower synchrotron radiation of protons. The disadvantage of a proton collider is, that protons are not fundamental. Protons consist of three types of partons; valence quarks, gluons and sea quarks. The valence quarks are two up and one down quark. The gluons are the mediator of the strong force,

holding the valence quarks together. The gluons are able to produce pairs of virtual quarks, which immediately annihilate. This permanent production and annihilation of quarks leads to a sea of quarks, accordingly called sea quarks. These constituent particles have no well defined momentum. Only a probability for a given particle to carry a certain fraction of the proton momentum at a given energy scale can be given with the Parton Distribution Functions (PDFs), shown in Fig. 3.1. The PDFs have been precisely measured with dedicated experiments [16]. As

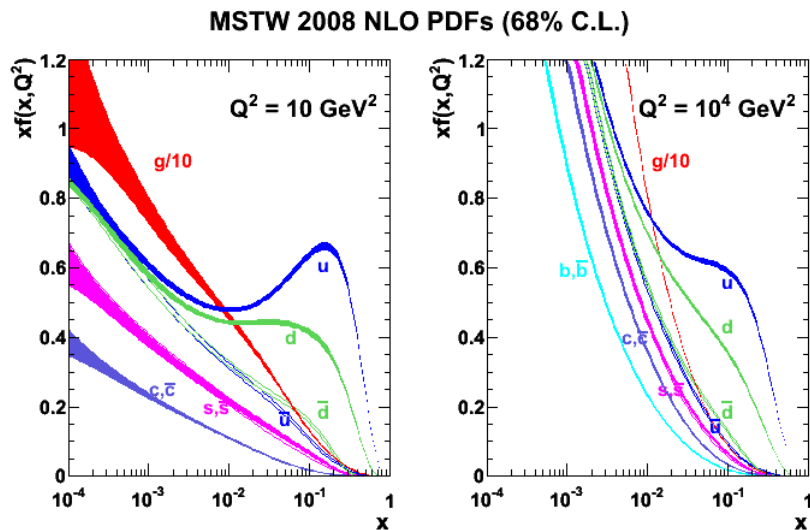


Figure 3.1: The parton distributions for the LHC [17].

the momenta of the incident partons are not well defined for a hadron collider the center-of-mass energy in the parton-parton system is unknown. Undetectable particles are evidenced by missing energy which is not possible if the incident energy is unknown. To compensate this the momenta in the transverse plane can be considered. Due to the beam direction along the z -axis the momenta of the colliding partons are also along the z -axis. From the momentum conservation in each direction follows, that the momenta of the produced particles in the transverse plane should be zero. The rest mass of the SM particles is negligible against their momentum in high energy physics. Therefore the missing transverse energy $\cancel{E}_T = -\sum_i (p_T)_i$, where $(p_T)_i$ are the momenta of all involved particles, can be used to evidence undetectable particles.

A further disadvantage of a proton collider is the large background due to QCD-processes, as all partons carry color.

The particle beam is subdivided into bunches. The design time between two bunch crossings is 25 ns. The collision rate in a collider is given by the luminosity

$$L = f \frac{n_1 n_2}{4\pi\sigma_x\sigma_y}, \quad (3.1)$$

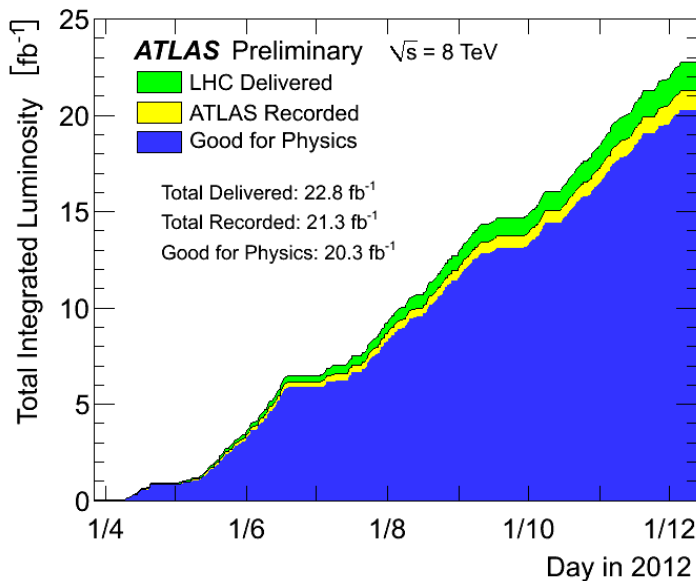


Figure 3.2: The integrated luminosity delivered by the LHC as well as the taken data and the data good for physics from the ATLAS experiment are shown against the date in 2012 Ref. [20].

where f is the bunch-crossing frequency, $n_{1,2}$ are the numbers of protons in the colliding bunches and $\sigma_{x,y}$ are widths of the beams in x - and y -direction. The integrated luminosity $\int L dt$ is proportional to the number N of events observed for each process

$$N = \sigma \int L dt, \quad (3.2)$$

with the proportionality constant σ , the cross section of the process. The LHC is designed for a peak luminosity of $1 \times 10^{34} \text{ cm}^{-2}\text{s}^{-1}$. This states an enormous rate and is only surpassed by the b-factories KEKB [18] and PEP-II [19] running at lower energies.

During one bunch-crossing several protons can interact. The measurements of the particles from the interesting interactions can be therefore corrupted by particles from further interactions. This is called in-time pile-up. As the readout windows of several sub-detectors exceed the bunch spacing, also the so called out-of-time pile-up can corrupt the measurements, which are particles from different bunch-crossings.

As these conditions state a new milestone in the field of particle accelerators many new challenges arise and have to be solved. The luminosity as well as the beam energy are therefore increased stepwise. The data for this analysis were taken in 2012 at a center-of-mass energy $\sqrt{s} = 8 \text{ TeV}$ with a bunch spacing of 50 ns. The amount of data good for physics taken in 2012 at the ATLAS detector were $\int L dt = 20.3 \text{ fb}^{-1}$, see Fig. 3.2. With data good for physics is meant that no malfunctions of the detector corrupted the data.

The numbers not explicit mentioned in this section as well as further details on the LHC can be found in Ref. [21].

3.1.2 The ATLAS Detector

The ATLAS detector is, just like CMS, a general-purpose particle detector at the LHC. The ATLAS detector is used for particle identification as well as for precision measurement of the particle observables, as for example momentum or energy. This has to be dealt with under the extreme conditions of rate and center-of-mass energy provided by the LHC.

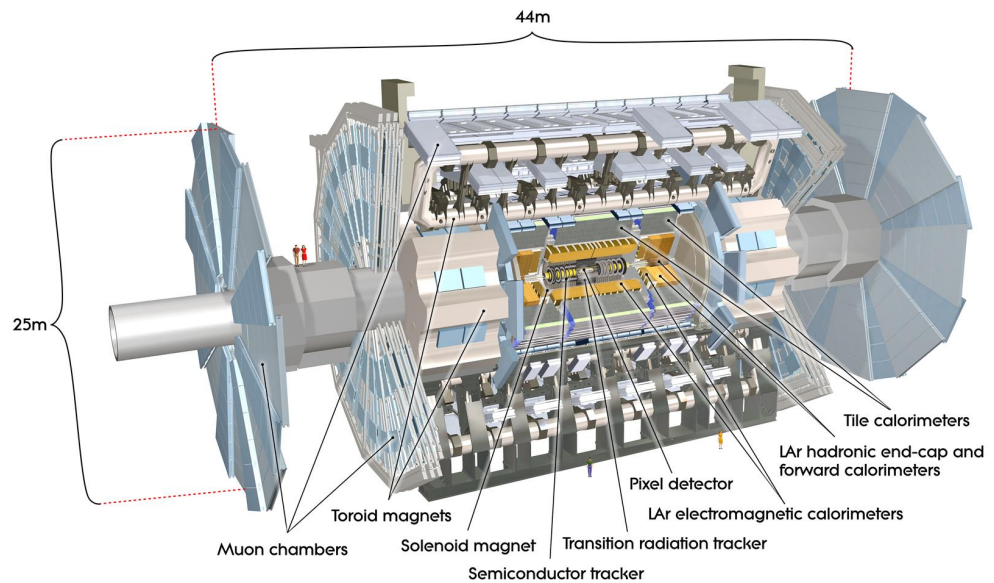


Figure 3.3: The ATLAS detector with labeled subsystems, taken from Ref. [22]. The ATLAS detector is the largest general-purpose particle detector built so far with a length of 44 m and a height of 25 m .

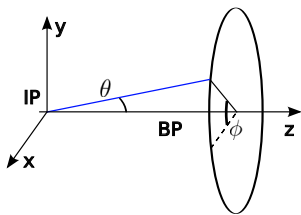


Figure 3.4: The coordinate system for the ATLAS detector with the nominal Interaction Point (IP) and the Beam Pipe (BP).

The ATLAS detector is built as a series of cylindrical layers of different detector systems in the barrel region and with similar structured circular plate layers in the end-cap region, see Fig 3.3. The innermost system is the Inner Detector (ID). The next components are the Electromagnetic (EM) and hadronic calorimeters. The outermost system is the muon spectrometer. A right-handed coordinate system can be placed in the ATLAS detector, illustrated in Fig. 3.4. The x -axis points to the center of the LHC, the y -axis points upwards and the z -axis follows the beam pipe. A polar coordinate system can be used as well, where the z -axis remains on the beampipe, the polar angle ϕ describes the angle in the x - y -plane to the x -axis and the azimuthal angle θ is the angle to the beam pipe. In collider physics the pseudorapidity η is used for the azimuthal direction instead of the angle θ . η is defined

$$\eta = -\ln \left[\tan \left(\frac{\theta}{2} \right) \right]. \quad (3.3)$$

The advantage of η is, that differences in pseudorapidity $\Delta\eta$ are Lorentz invariant. A further advantage is, that the particle rate is almost constant as a function of η . A detailed description of the ATLAS detector as

well as the numbers mentioned in this section, if not explicitly referenced otherwise, can be found in Ref. [22].

The different detector systems and subsystems are explained in the following passage.

The Inner Detector

The main task of the ID is the measurement of momentum. It is therefore immersed in a solenoidal magnetic field. The magnetic field bends the tracks of the particles due to their charge and momentum. Hence the goal is a precision position measurement of the particle tracks. The innermost component is the silicon pixel tracker followed by a silicon microstrip tracker (SCT). More details about the pixel detector are given in Sec. 3.4.1 as it can be used for the measurement of the energy-loss which is an important observable for the search for heavy LLPS. The silicon trackers provide high-rate capability as well as high-accuracy position measurement due to the small size of the pixels and stripes. The outermost component is the Transition Radiation Tracker (TRT) consisting of gas filled drift tubes. The TRT has a worse spatial precision, but states, as it fills a larger volume, a good compromise between cost and precision. Beside the momentum measurement the precision measurement can also be used to reconstruct secondary or displaced vertices. This can be for example used for b-quark identification.

The Electromagnetic Calorimeters

The electromagnetic calorimeter is a Lead-Liquid Argon (LAr) detector with the aim of precision energy measurement for electromagnetically interacting particles. A sampling calorimeter consists of periodic layers of absorber and sampling material. Particles produce electromagnetic particle shower in the absorber material, due to Bremsstrahlung and pair production¹. The energy deposit is measured in the sampling material. This allows a precise reconstruction of the incident particle energy. The absorber and the electrodes, used for the readout of the LAr, have an accordion-shaped geometry offering a crackless design in ϕ .

The Hadronic Calorimeters

The hadronic calorimeters are the tile calorimeter in the barrel region and LAr calorimeters in the two end-caps. The principle of hadronic calorimeters is very similar to EM calorimeters. The difference is, that the hadronic particle showers are produced due to strong interactions. The shower are therefor wider and longer and hence exceed the EM calorimeters. The tile calorimeter (TileCal) consists of steel as absorber material and scintillating tiles as active medium, whereas the LAr hadronic calorimeters use copper as absorber and LAr as active medium. More

¹Pair production is the conversion of a photon into an electron-positron pair nearby a nuclei or electron needed for momentum conservation. Bremsstrahlung is the radiation of photons from a high-energetic electron or positron in the electromagnetic field of atomic nuclei.

details on the TileCal and in particular about the timing information reconstruction are given in Sec. 3.4.2.

The Muon Spectrometer

The outermost and largest component of the ATLAS detector is the muon spectrometer. It is used for an independent precision momentum measurement for muons as they are the only charged SM particles able to leave the calorimeters. The muon spectrometer is therefore immersed in a toroidal magnetic field. Also in the muon spectrometer the momentum is reconstructed from the bend of the track in the magnetic field. The barrel region is equipped with Monitored Drift Tubes (MDT) for accurate position measurement and Resistive-Plate Chambers (RPC) for timing measurement. The timing information is essential for the trigger system and can be also used for time-of-flight measurements. In the end-cap regions MDTs, Thin-Gap Chambers (TGC) and Cathode Strip Chambers (CSC) are used.

3.2 Production and Interaction of Long-Lived Particles

This section describes the production mechanisms and the kinematic properties of LLPs at the LHC. Also the interaction of LLPs and in particular R -hadrons with the detector material will be discussed.

3.2.1 Production

LLPs are expected to be mostly pair-produced. The reason for that is the proportionality $\sigma(ab \rightarrow X) \propto \Gamma(X \rightarrow ab)$, which is model independent². This means that the production rate of a single LLP X from two SM particles a and b is proportional to the decay width to the same SM particles. The particle can hence either have no significant production rate and a long lifetime or a high production rate and a short lifetime, and therefore does not count as a LLP. The dominant production is either the rapid decay of a heavy particle to two LLPs or the direct pair production. For R -parity conserving models only direct pair production is allowed. The considered production processes are hence gg -fusion, $q\bar{q}$ -annihilation (shown in Fig. 3.6) and qg -annihilation.

The parton-level differential cross section for this processes can be obtained from the Lagrangian of the model, the masses of the particles and the couplings. The latter two are free parameters or result from free parameters of the chosen theory. The double-differential distributions

²It is only dependent on mass, spin and color.

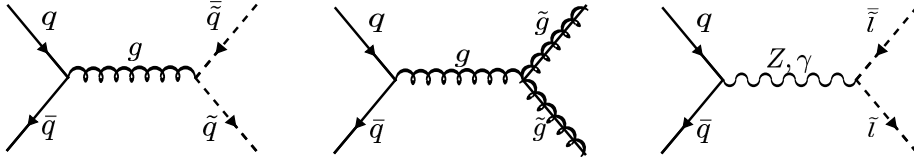


Figure 3.5: Examples for Feynman graphs of the leading production processes for LLPs. The processes shown are pair production of squarks (left), gluinos (middle) and sleptons (right) via $q\bar{q}$ -annihilation. Also gg -fusion or qg -annihilation are possible.

$d^2\sigma/(dp_T dy)$ are estimated through the convolution of the partonic differential distributions with the parton density distributions. The total cross section is obtained from the integration over rapidity y and transverse momentum p_T [23].

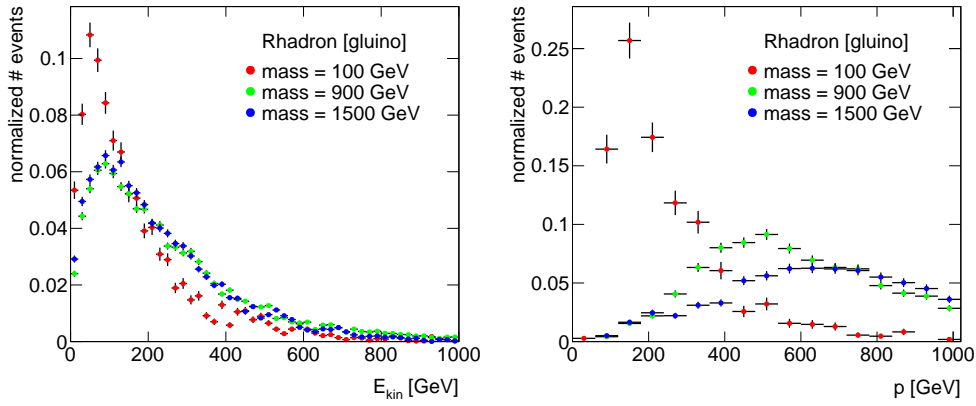


Figure 3.6: The left diagram shows the Rhadron kinetic energy (E_{kin}) spectrum for different gluino mass points. The momentum distributions for different gluino mass points are shown in the right diagram.

The left diagram in Fig. 3.6 shows the kinetic energy distributions of gluino R -hadrons for different gluino masses. The spectra get slightly broader for higher masses. This is understandable as E_{kin} states the energy abundance after the production of the particle mass

$$E_{kin} = E - mc^2. \quad (3.4)$$

The energy available is given by the momenta of the two partons, as their mass is negligible. The parton momenta follow the PDFs for the given particle types. The kinetic energy spread follows the slope of the PDF in the region where the partons carry momenta to produce the two heavy LLPs. A flat PDF in this region means, that the possibility for parton carrying the minimum momentum is similar to the possibility of carrying more momentum, resulting in more E_{kin} for the LLPs. In the region where the fraction of the momentum is more than ~ 0.2 , the valence quarks have higher possibilities to carry these momenta. The quarks have more flat PDFs than the gluons which are dominant in the region of lower momentum fraction. This is in good agreement with the E_{kin} spectra, as they are broader for $m > 0.2 \times 4$ TeV.

The momentum with respect to E_{kin} and the rest mass m_0 can be calculated as

$$p = E_{kin} \sqrt{1 + 2 \frac{m_0}{E_{kin}}}. \quad (3.5)$$

The momentum as a function of the rest mass for a fixed $E_{kin} = 100$ GeV is shown in Fig. 3.7. $E_{kin} = 100$ GeV is chosen as the approximate peak energy of the E_{kin} spectra. Following Fig. 3.7 for the masses of 100 GeV, 900 GeV and 1500 GeV a momentum of 150 GeV, 450 GeV and 550 GeV is expected. This is in good agreement with the peaks of the momentum distributions for the different gluino masses in Fig. 3.6 (right). For particles with masses in the order of the kinetic energy the velocities differ significantly from the speed of light. This is an important property of heavy LLPs as they are expected to have mean velocities between 0.4 c and 0.9 c depending on the rest mass of the particle. Exemplary β distributions for stau particles, R -hadrons and muons are shown in Fig. 3.8.

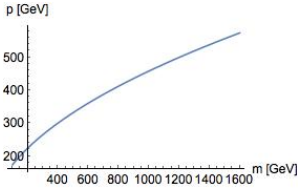


Figure 3.7: Momentum as a function of the rest mass for $E_{kin} = 100$ GeV.

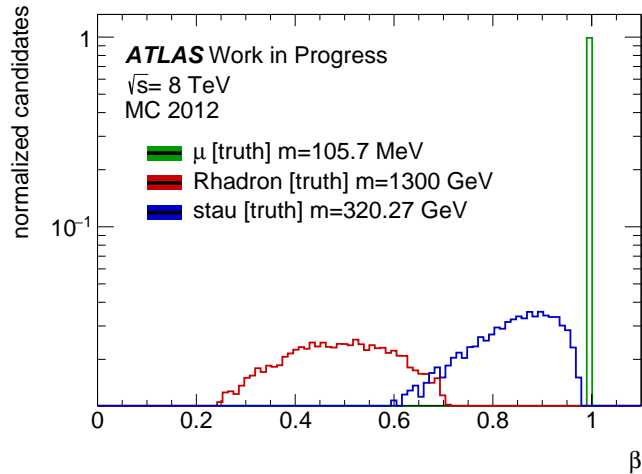


Figure 3.8: The β distributions for $\tilde{\tau}$ particles, \tilde{g} Rhadrons and muons.

It can be seen that muons are produced with almost the speed of light. The heavy LLPs have broad velocity distributions, where the mean value depends on the mass of the particle. For gluino Rhadrons with a mass of 1300 GeV the velocities range from 25% to 70% of the speed of light. LLPs are therefore clearly distinguishable from muons, as the main SM background.

Colored LLPs have to fulfill the quark confinement and therefore hadronize. The possible states for gluinos are "mesonic" $\tilde{g}q_1\bar{q}_2$, "baryonic" $\tilde{g}q_1q_2q_3$ and "glueball" $\tilde{g}g$ states. For squarks the possible states are "mesonic" $\tilde{q}\bar{q}_1$ and "baryonic" $\tilde{q}q_1q_2$ states. Of particular interest for the search for heavy LLPs is the composition of charge and uncharged hadronized states, as uncharged R -hadrons would not leave a signal in the tracking system. One model describing hadronization is the Lund string fragmentation model [24]. In this model the confinement is represented

by a string with constant tension. The colored quarks/squarks are at the endpoints of the string. Thorough the movement away from the IP the string is pulled out. This means that energy is transferred to the string. If the energy of the string is sufficient, a quark pair ($q\bar{q}$) can be produced. This can repeat for the strings between the new quarks and the incident quarks. A jet of hadrons forms. The assumption of a universal composition of light-flavor quarks produced in the hadronization can be used. From LEP data the constraints on the composition is $u : d : s \approx 1 : 1 : 0.3$, where diquarks are further suppressed [25]. "Mesonic" states occur more often as less quarks have to be produced. Important for the interpretation of the results of the MAg search is the difference between the composition of charged and uncharged sbottom and stop R -hadron states. From the composition of light quarks produced in the hadronization, the fractions f of R -hadron states for stop as exotic particle are $f(R_{t\bar{d}}^+) = 39.6\%$, $f(R_{t\bar{u}}^0) = 39.6\%$ and $f(R_{t\bar{s}}^+) = 11.8\%$. The missing 9% are "baryonic" states. The fractions for sbottom R -hadron states are basically the same. The only difference between sbottom and stop R -hadron states is, that for sbottom $R_{b\bar{u}}^-$ is charged, whereas $R_{b\bar{d}}^0$ and $R_{b\bar{s}}^0$ are uncharged. Consequently sbottoms tend to hadronize more often to neutral R -hadron states than stops.

Concluding, LLPs are expected to be mainly pair-produced in the ATLAS detector. They are expected to have high momenta, which together with the high mass leads to a low velocity of the particles. As all SM particles are lighter than the hypothetic LLPs, the velocity states a good discriminator between LLPs and SM background. Colored sparticles hadronize with light SM particles. As the light SM quarks are two down-type and one up-type quark, the down-type sbottom more often hadronizes to neutral states than the up-type stop.

3.3 Signatures of Particles in the Detector

As LLPs have lifetimes sufficient to directly interact with the detector, it is essential to understand how their signatures in the detector can look like for different possible scenarios. In the first section the SM particle signatures in the detector are explained. In the second section important LLP signatures in the detector are described.

3.3.1 Standard Model Particles

The different signatures of the SM particles are shown in Fig. 3.9.

The Electron is a charged lepton. It produces bent tracks in the ID due to its charge. As it interacts via the EM interaction, the electron showers and gets stopped in the EM calorimeter.

The Photon is the mediator particle of the EM force. As it is uncharged

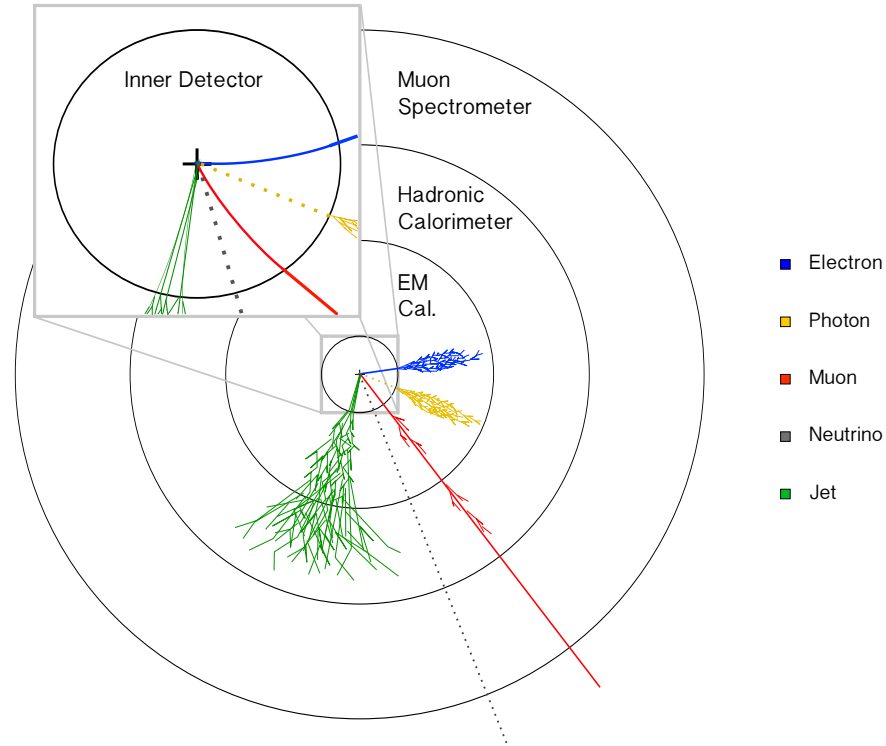


Figure 3.9: The signatures of SM particles in the detector. Quarks hadronize due to the quark confinement leading to jet objects in the detector. Dashed lines indicate particles which are not detectable.

no track in the ID is expected. Photons interact electromagnetically and therefore produce particle showers in the EM calorimeters. The signature is thus large energy deposits in the EM calorimeters with no associated track in the ID.

The Muon is a high-mass copy of the electron. It therefore produces a track in the ID. The main energy loss of leptons at high velocities happens via Bremsstrahlung. This process describes the radiation of a photon due to the acceleration of the lepton in the fields of nuclei. The acceleration is indirectly proportional to the mass of the particle. As the muon mass is 200 times larger than the electron mass, the muon is not stopped in the calorimeters. The muon has also an associated track in the muon spectrometer allowing a precision momentum measurement. It is the only charged SM particle able to leave the detector.

The Neutrino is an uncharged lepton it neither interacts by EM nor by strong force. The weak and gravitational interactions are negligible in a general-purpose detector. Hence the neutrino leaves the detector undetected. The only possibility to evidence the production of neutrinos is \cancel{E}_T .

The Jet consists of the hadrons produced due to the hadronization of colored particles. The charged hadrons in the jet produce a bundle of tracks in the ID. The directions of these particles are roughly the same due to the boost of the incident quark. The hadrons produce particle

showers in the EM as well as in the hadronic calorimeter.

3.3.2 Heavy Long-Lived Particles

LLPs are able to directly interact with the detector. But as they may arise with very different lifetimes and properties they can leave different signatures in the detector. Fig. 3.10 shows signatures considered in searches with the ATLAS detector.

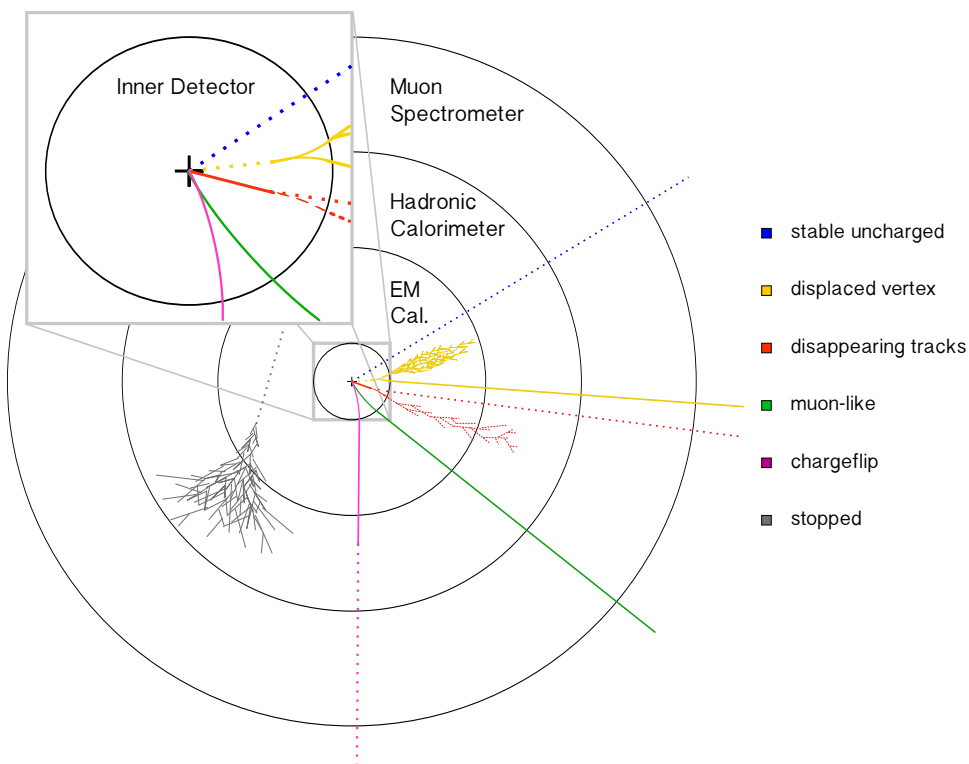


Figure 3.10: Signatures of LLPs in the detector. Most of the mentioned scenarios also provide slightly different signatures due to different final state particles. For this cases one specific is displayed, whereas the others are mentioned in the text. Dashed lines indicate particles which are not detectable.

Stable uncharged LLPs do not interact with the detector and are basically a high mass copy of the neutrino. These particles are good candidates for dark matter, as they do not interact over the EM or strong force. The searches are based on the associated final state particles and missing transverse energy. This means that they depend on the production mechanism and are thus model dependent

A **Displaced Vertex** occurs if the LLP decays a significant distance away from the primary interaction point. The considered displaced vertices have to be within the pixel detector. In these scenarios the LLPs are uncharged and have lifetimes between pico- and nanoseconds. The considered decay products in the search for SUSY particles are charged lepton pairs with one neutrino, as displayed in Fig. 3.10, or at least five charged particles. The latest published results and further information can be found in Ref. [26].

Disappearing Tracks are the signatures of charged LLPs decaying in the ID to undetectable daughter particles. These signatures occur for models with an almost mass degenerated charged NLSP with an uncharged LSP. The decay of the NLSP produces therefore the undetectable LSP and a soft³ pion. The pion is not reconstructed due to the small momentum. Ending tracks have thus no associated hits in the outer tracking region and in the calorimeters. A detailed description of the searches performed with the ATLAS detector can be found in Ref. [27].

Muon-like are signatures of charged Stable Massive Particles (SMP) able to fly through the hole detector. SMPs can be either colorless particles, such as sleptons and charginos, or R -hadrons. Colorless SMPs are comparable to heavy muons and are therefore not stopped in the calorimeters due to their high masses. R -hadrons interact differently with the detector as they are able to interact via the strong force. An important property of R -hadrons is that the heavy exotic particle does not significantly contribute to the interaction with the detector material. The reason for that is, that the interaction of a parton (mass m_{par}) with a quark of a nucleus is suppressed by $1/m_{par}^2$. Most of the interaction is thus performed by the light SM particles, whereas the exotic particle acts as spectator. Hence stable R -hadrons are also able to leave the detector.

Chargeflips are a particular feature of R -hadrons. They can occur due to the interaction of the SM particles with the detector material. This can lead to an exchange of particles. If the exchanged quarks carry different charges, the charge of the R -hadron changes. The process displayed in Fig. 3.10 is a charged to uncharged flip. Also the reverse process is possible, but not addressed in dedicated ATLAS searches. The latter two scenarios, muon-like and chargeflip, are the considered signatures for the Muon Agnostic (MAg) analysis, which does not include information from the muon spectrometer in the search for SMPs. The nominal ATLAS analysis can be found in Ref. [1].

Stopped R -hadrons are a further interesting scenario for the search for long lived particles. Some fraction of the produced R -hadrons may lose all their kinetic energy mainly through ionization energy loss in the detector material and get stopped. These particles can decay later into the LSP and hadronic jets. The strategy for the search for stopped R -hadrons is to look for large activity in the calorimeters in the time between two bunch crossings. Further information and the latest results can be found in Ref. [28].

Concluding heavy LLPs leave many different signatures in the detector partially having no significant SM background. This allows several model independent searches stating an important piece in the puzzle of the search for new particles.

³Soft means with low momentum due to the small mass difference.

3.4 Observables for the Search for Stable Massive Particles

Beside the signatures in the detector, heavy LLPs also differ in several observables significantly from SM particles. The most important for the search for SMPs are the energy loss and the velocity. The most suitable subdetector for energy loss measurements is the pixel detector. The energy loss measurement and the $\beta\gamma$ reconstruction will be described in the first section. The second section is about the time-of-flight velocity measurement with the TileCal.

3.4.1 Energy-loss

First a motivation for dE/dx as observable for the search for charged SMPs is given. This is followed by a description of the pixel detector and the motivation for the usage for the dE/dx measurement. The last part is about the dE/dx reconstruction and the $\beta\gamma$ estimation. The numbers mentioned in this section are taken from Ref. [22].

Motivation

Charged particles are able to lose energy in material due to the interaction with the nuclei or the bound electrons. The interaction with the nuclei is called non-ionising energy loss, whereas the interaction with the electrons is called ionisation energy loss, due to the liberation of the bound electrons through the interaction. The dominant process for relativistic particles is the ionisation energy loss, described by the Bethe-Bloch formular

$$\left\langle \frac{dE}{dx} \right\rangle = \frac{4\pi e^4 Z_1^2}{m_e c^2 \beta^2} n \left(\frac{1}{2} \ln \left(\frac{2m_e c^2 \beta^2 \gamma^2 T_{max}}{I_e^2} \right) - \beta^2 - \frac{\delta}{2} \right), \quad (3.6)$$

with m_e the mass and e the charge of the electron, n the volume density of electrons in the material, the velocity $\beta\gamma$ of the particle traversing the material, I_e the mean ionisation potential of the material and T_{max} the maximum energy transfer to a free electron in a single collision

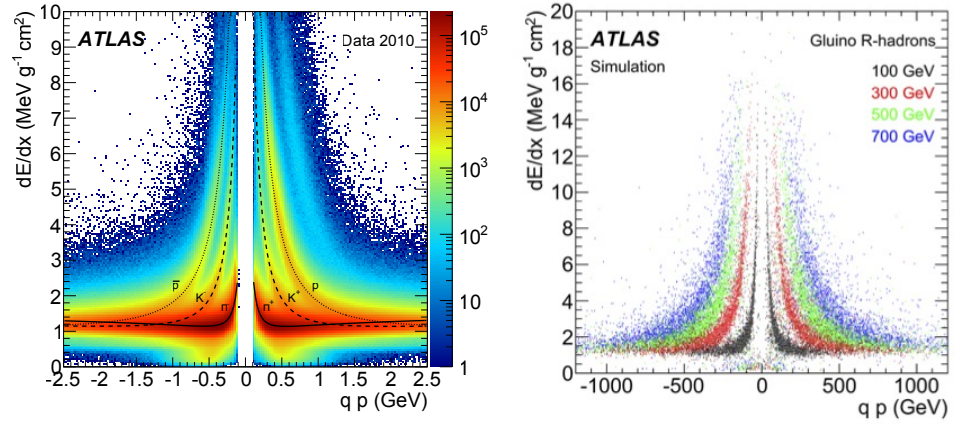
$$T_{max} = \frac{2m_e c^2 \beta^2 \gamma^2}{1 + 2\gamma \frac{m_e}{M} + \left(\frac{m_e}{M}\right)^2}, \quad (3.7)$$

which reduces to Eq. 3.8 for heavy particles.

$$T_{max} = 2m_e c^2 \beta^2 \gamma^2 \quad (3.8)$$

Following this, a high dE/dx is expected for slow LLPs. This can be seen in Fig. 3.11.

Figure 3.11: The energy loss reconstructed with the pixel detector for tracks as a function of momentum times charge (left). The most probable value distributions of pions (solid), kaons (dashed) and protons (dotted) are superimposed. The expected distributions for Rhadrons with several \tilde{g} masses are shown in the right diagram [1].



The dE/dx observable can be used to distinguish SM particles from heavy charged SMPs. As Eq. 3.6 is only dependent on material specific quantities, dE/dx can further be used for a $\beta\gamma$ estimation. This together with the momentum measurement through the bend of the track in the ID allows a mass estimation for the particle. The mass can be calculated using

$$m_{\beta\gamma} = \frac{p}{\beta\gamma}. \quad (3.9)$$

The mass is the quantity of interest as it is a property of the particle and a free parameter in the Lagrangian of the possible new theories. It therefore reduces the parameter space for possible new theories and might allow predictions for further particles.

Pixel Detector

The pixel detector consists of three concentric layers with 1456 modules in the barrel region and 3 layers on each side in the end-caps with 288 modules. The Insertable B-Layer (IBL) was placed as additional fourth layer during the long shutdown 2013-15 inside the existing layers. It is placed on the renewed beam pipe, for details consult Ref. [29]. The IBL is equipped with 224 modules. The modules have a size of $19 \times 63 \text{ mm}^2$ and consist of 46080 pixels. The size of a single pixel is $50 \times 400 \mu\text{m}^2$. The pixels are linked via bump bonds to the front-end readout chips. The bare signal is preamplified in the readout chip to a signal with a width proportional to the deposited charge in the pixel. The number of 25 ns clock cycles, where the signal exceeds a programmable threshold (time-over-threshold ToT) is digitized and stored as 8 bit signal.

The pixel detector produces a stable ToT signal for a wide range of charge deposits. This allows the most precise dE/dx measurement of

the ATLAS subsystems. It is further well suitable as it is the innermost component of the detector and thus particles would not have lost a significant amount of energy on their way from the IP to the pixel detector. Also the small thickness of the pixels is an advantage as it ensures a constant dE/dx for all pixel layers.

$\beta\gamma$ Estimation

Particles mostly deposit their whole charge not in one single pixel. Hence the charge deposit in a pixel layer is calculated as the sum over a cluster of pixels. The energy loss can be calculated from the cluster charge deposit Q , the average energy needed for the production of an electron-hole pair, $W = 3.68$ eV [30], the thickness of the silicon d , the angle of incident α and the silicon density ρ with

$$\frac{dE}{dx} = \frac{QW \cos \alpha}{epd}. \quad (3.10)$$

The dE/dx measurements for each cluster follow a Landau distribution, as shown in Fig. 3.12.

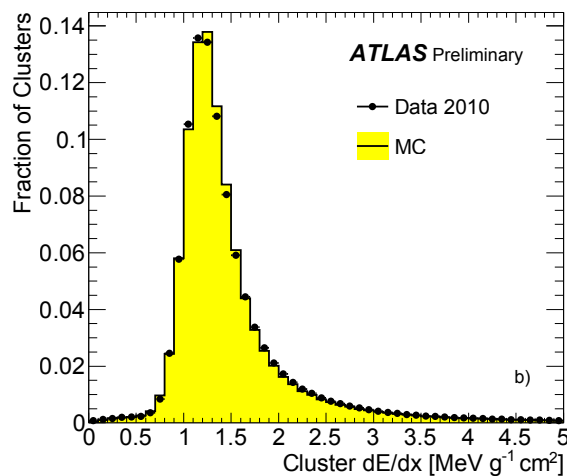


Figure 3.12: The cluster dE/dx measurements for 2010 Data and Monte Carlo [31].

An average of three associated pixel clusters was obtained for the tracks, according to the three detector layers. Due to this small statistics, averaging of the measurements would give the most probable value of the Landau distribution instead of the overall mean described by the Bethe-Bloch formula. To ensure that no measurements from the tail of the Landau distribution smear the dE/dx measurement, the truncated dE/dx averaging is used. The truncated mean is calculated from the 70 % lowest energy loss measurements. For the pixel dE/dx this means, that mostly the measurement with highest energy deposit is excluded from the averaging.

For the $\beta\gamma$ estimation it is essential to know, that the averaging gives the Most Probable Value (MPV) not the mean, because this means that the Bethe-Bloch formula could not be used. Instead the five parameter function Eq. 3.11 is used.

$$MPV_{dE/dx}(\beta\gamma) = \frac{p_1}{\beta^{p_3}} \ln(1 + (|p_2|\beta\gamma)^{p_5}) - p_4 \quad (3.11)$$

The free parameters $p_1 \dots p_5$ are fixed by the fit to the MPV distributions for kaons, pions and protons in Fig. 3.11 left. A detailed description of this parametrization can be found in Ref. [31]. $\beta\gamma$ is obtained by inverting Eq. 3.11.

For the new run in 2015 the dE/dx measurement will improve as with the IBL an average of four measurements per track is expected.

3.4.2 Time-of-Flight

This section describes the time-of-flight velocity measurement with the TileCal. The first part gives a motivation for usage of the TileCal for time-of-flight measurement. This is followed by a description of the timing extraction from the TileCal signal. The last part is about the β estimation.

Motivation

The TileCal is a subsystem suitable for time-of-flight measurements. The most precise time-of-flight measurements can be done with the muon spectrometer. For the full-detector analysis described in Ref. [1] both the TileCal and the muon spectrometer are used for a combined β estimation. The MAg search, described in Sec. 4.3, aims to be sensitive to R -hadrons undergoing a chargeflip from charged to uncharged. It therefore does not include informations from the muon spectrometer, as uncharged R -hadrons would not be detected there. Hence the time-of-flight measurement with the TileCal is the best available for the MAg analysis.

Also with the β measurements a mass estimation is possible. Again an additional momentum measurement is necessary for the mass estimate. Eq. 3.12 is used to calculate the mass from the velocity β and the momentum p .

$$m_\beta = p \sqrt{\frac{1}{\beta^2} - 1} \quad (3.12)$$

The TileCal β estimate is important as it states a complementary velocity measurement to the $\beta\gamma$ estimate from the pixel dE/dx.

Tile Calorimeter

The TileCal is the barrel subdetector of the hadronic calorimeters. It consists of three cylindric sections, the barrel and the two extended barrels. Each barrel consists of 64 modules in ϕ with a size of $\Delta\phi = 0.1$ rad. The layout of a TileCal module is shown in Fig. 3.13. Steel is used as absorber and scintillating tiles as active medium. The absorber and tile plates are placed staggered in r -direction and periodic in z -direction. The tiles are read out on both sides with wave-length shifting fibers. The fibers root to different photomultipliers (PMT) placed on the upper side in r -direction. The modules are substructured through the grouping of fibers to specific PMTs. These substructures are referred to as cells. The layout of the cells is shown in Fig. 3.14. The dimensions and shapes of

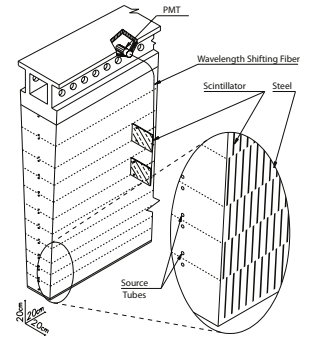


Figure 3.13: Design of a ATLAS Tile Calorimeter module [22].

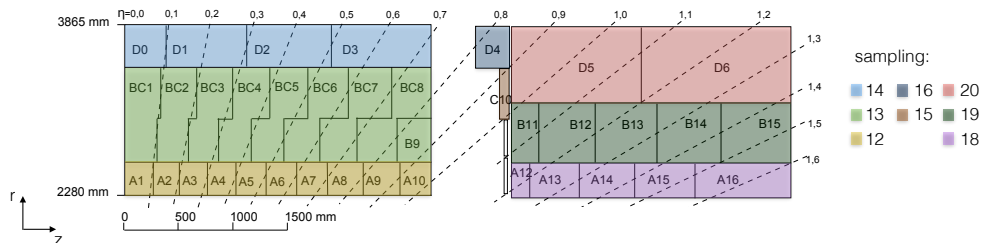


Figure 3.14: Layout of the TileCal cells and their labeling. The design of the cells in negative z -direction is symmetric.

the cells are different. The innermost cell A1 for example has a size of $\sim 25 \times 25$ cm, whereas the outermost cell D6 has a size of $\sim 1 \times 1.5$ m. The shape of the cells of sampling scheme 13 (see Fig. 3.14) are basically two shifted rectangular cells. This shape is chosen to have a quasi-projective geometry. The η extension of the cells is similar, with $\Delta\eta \approx 0.1$ for the barrel cells and $\Delta\eta \approx 0.2$ for the extended barrel cells. The signal from the PMTs is amplified and shaped in the front-end electronics. The FWHM of the signal pulse is fixed to about 50 ns [32]. The front-end-electronics produces a high and a low gain pulse. Each signal is digitized by an Analogue to Digital Converter (ADC). The signals are sampled every 25 ns and the values are stored in the Tile Data Management Unit chip until the event is accepted by the first-level trigger. The samplings are synchronized with the 40 MHz system clock, whereby the fourth sampling corresponds to the point in time where a particle, produced at the nominal IP and traveling with the speed of light, arrives at the center of a cell. The high-gain signal is used for the signal reconstruction, except the ADC saturate. For that case the low-gain signal is used.

Signal Reconstruction

The signal reconstruction has the aim to estimate the three main characteristics of a signal pulse: amplitude, pedestal and phase (Fig 3.15).

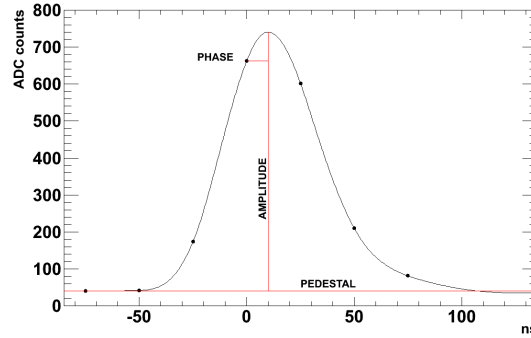


Figure 3.15: The TileCal signal pulse with the seven samplings (dots) [32].

⁴The processing time for one signal reconstruction has to be below 10 μ s.

The algorithm used has to handle two challenges. It has to be fast⁴ and it has to be stable against electronic noise and pileup fluctuations. The algorithm used is the Optimal Filtering (OF). The OF uses weighted linear combinations of the seven samplings S_i to calculate the amplitude A , the pedestal p and the phase τ (Eqs. 3.13).

$$A = \sum_{i=1}^n a_i S_i, \quad A\tau = \sum_{i=1}^n b_i S_i \quad \text{and} \quad p = \sum_{i=1}^n c_i S_i \quad (3.13)$$

The weights a_i , b_i and c_i are obtained by minimizing the variance of the parameters against the electronic noise and pileup fluctuations. Further a knowledge of the signal pulse shape is needed. The pulse shape was precisely measured with test beams and validated with collision data.

The quantity of interest for the search for SMPs is the phase from now on called cell time t_{cell} , which is the time difference of the peak of the pulse to the fourth sampling. It is therefore a measure for the relative time to a particle originating from the IP, traveling with the speed of light and arriving at the cell center. This allows to calculate the time-of-flight of the particle with Eq. 3.14, where d is the distance from the IP to the center of the cell.

$$t_{ToF} = t_{cell} + \frac{d}{c} \quad (3.14)$$

One problem of this measurement is, that the OF algorithm is optimized for small phases: $t_{cell} < 10$ ns. SMPs, as they are expected to be significantly slower than the speed of light, are able to arrive within the full readout window of 75 ns. For example a particle with 0.2 c would arrive at an outer cell, with a distance to the IP of 5 m, 66.7 ns after a particle traveling with the speed of light. The OF algorithm does not reconstruct the correct cell time for larger values of the t_{cell} . The reason for that is, that the OF is based on a linearization of the pulse time dependence. For larger values of t_{cell} higher orders getting more and more important and hence corrupt the t_{cell} measurement. For further information see

Ref. [32].

To allow precise time measurements a time calibration is needed. The calibrations done for the ATLAS Tile Calorimeter are described in Ref. [33]. Corrections are mostly applied, due to differences in the fiber lengths.

β Estimation

With the time-of-flight information from the TileCal signal a β estimation for each passed cell can be done with Eq. 3.15.

$$\beta_{cell} = \frac{d_{cell}}{t_{cell}c + d_{cell}} \quad (3.15)$$

As the TileCal consists of three layers of cells the particles are expected to transverse several cells as can be seen in Fig. 3.16. The particles deposit energy in each cell passed due to the energy loss in the detector material. Due to that, several beta measurements for a given particle are possible. To obtain the most precise β estimation, these measurements are combined to a mean $\bar{\beta}$. The single β measurements have very different uncertainties due to the energy deposit and the distance of the cell to the IP. Therefore it is essential to use a weighted mean estimation. For the weights the uncertainties of the β measurements have to be calculated. The main contribution to the β estimation is the $\sigma_{t_{cell}}(E_{dep})$ according to the energy deposit in the cell. The timing resolution can be parametrized from data, shown in Fig. 3.17.

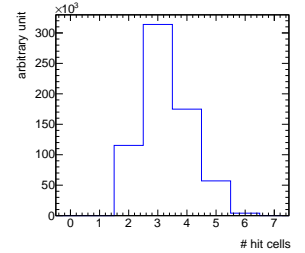


Figure 3.16: The number of passed TileCal cells for muons.

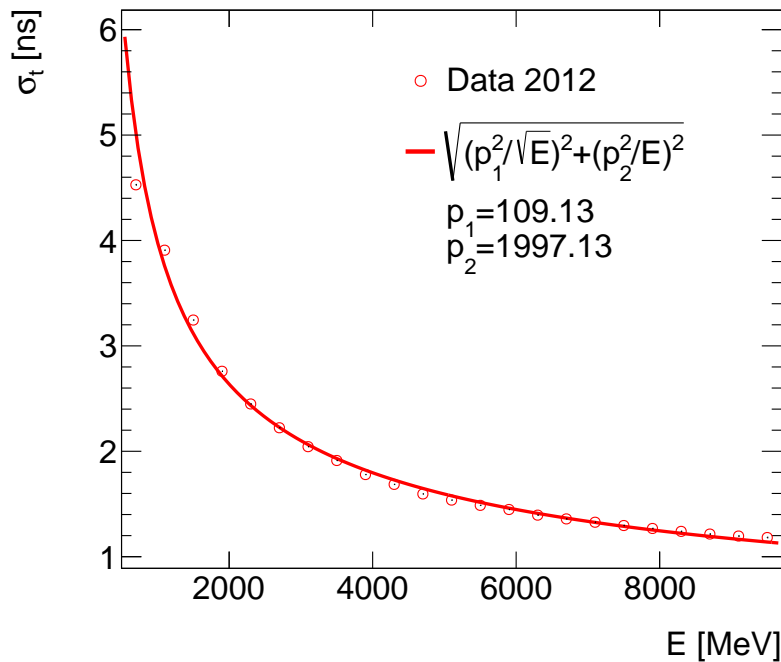


Figure 3.17: Functional parametrization of $\sigma_{t_{cell}}(E)$ for muons.

The $\sigma_{t_{cell}}$ values are obtained from the t_{cell} distribution as a function of the energy deposit in the cell. The distribution is divided into slices in E . Each slice is fitted with a Gaussian and the σ of the Gaussian is used as uncertainty of t_{cell} . This can be done as muons are expected to be produced with almost the speed-of-light and therefore no bias is expected. More details on this will be given in Sec. 4.2.7. To ensure a reasonable t_{cell} measurement and to suppress detector noise, only cells passed with an energy deposit $E > 500$ MeV, are included in the averaging. The mean is calculated for β^{-1} as it ensures, due to the proportionality to t_{cell} , that it is also normally distributed. Hence it is allowed to calculate the mean by

$$\beta^{-1} = \frac{\sum_{i=0}^N \beta_i^{-1} / \sigma_{\beta_i^{-1}}^2}{\sum_{i=0}^N 1 / \sigma_{\beta_i^{-1}}^2}, \quad (3.16)$$

where

$$\sigma_{\beta_i^{-1}} = \frac{\sigma_{t_{cell}}}{d}. \quad (3.17)$$

The overall uncertainty of β^{-1} is accordingly given by

$$\sigma_{\beta^{-1}}^2 = \frac{1}{\sum_{i=0}^N 1 / \sigma_{\beta_i^{-1}}^2}. \quad (3.18)$$

From that the uncertainty of β is obtained through error propagation as $\sigma_{\beta} = \beta^2 \sigma_{\beta^{-1}}$.

3.5 Summary

The LHC with the ATLAS detector was described in this section as the experimental setup for the studies presented in the following chapter. It was further motivated that heavy LLPs would be mainly pair produced with high momenta at the LHC. The high mass leads to slow velocities of the LLPs, compared to SM particles. Further the signatures of LLPs compared to SM particles have been discussed. From that a motivation for the MAg search was given being sensitive to SMPs and in particular to R -hadrons undergoing a charge-flip. Finally the dE/dx measurement with the pixel detector and β estimation with the TileCal were introduced. These observables allow two independent velocity measurements, which therefore are able to be less affected by detector mis-measurements constituting the main background for the search for SMPs. With the reconstructed velocities and a momentum measured in the ID a mass estimation is possible.

Chapter 4

Search for Stable Massive Particles

4.1 Data and Simulated Event Samples

Several samples are needed for the studies on β estimation with the TileCal as well as for the Muon Agnostic search. These samples are presented in this section.

4.1.1 Data Event Samples

The data used for the validation of the corrections on the β estimation and for the MAg analysis were taken at a $\sqrt{s} = 8$ TeV in 2012.

Events excepted by a subset of triggers are stored in a stream, e.g. events accepted by muon triggers are stored in the muon stream. Also event pre-selection requirements can be applied to events stored in a stream. For the validation of the β estimation a dedicated $Z \rightarrow \mu\mu$ stream is used. In the MAg analysis data events stored in the JetTauEtmiss stream are used. In the nominal analysis also the HadDelayed stream was used, which states an important difference between this analysis and the nominal one.

$Z \rightarrow \mu\mu$ Stream

For the validation of the studies on the β estimation the $Z \rightarrow \mu\mu$ stream is used. Muons from $Z \rightarrow \mu\mu$ are good to identify in data and, as muons are the main backgrounds for the search for SMPs, suitable for the validation of the β corrections. The integrated luminosity of the $Z \rightarrow \mu\mu$ enriched data samples is $\int L dt \approx 19.3 \text{ fb}^{-1}$

In the $Z \rightarrow \mu\mu$ stream an event pre-selection is applied. In each event at least one vertex with three associated tracks is required. The vertex position in z -direction has to be within $-150 \text{ mm} < z_{vertex} < 150 \text{ mm}$ from the origin of the ATLAS coordinate system. Furthermore at least

one muon, reconstructed with the StacoMuon or the Muid algorithm, with $p_T > 20$ GeV is required. An invariant mass of the two $Z \rightarrow \mu\mu$ muon candidates larger than 55 GeV is required.

RPVLL JetTauEtmis Stream

In the JetTauEtmis stream all events accepted by either a jet, a tau or a \cancel{E}_T trigger are stored. The integrated luminosity of the JetTauEtmis samples is $\int Ldt \approx 18.8 \text{ fb}^{-1}$. For this analysis the RPVLL JetTauEtmis stream is used, which has a event pre-selection applied. The events are required to have at least one ID track with $p_T > 80$ GeV, at least six hits in the SCT and at least two hits in the pixel detector.

HadDelayed stream

In the nominal MAg analysis, beside the JetTauEtmis stream, also the HadDelayed stream was used. Due to technical reasons this was not possible for this analysis. In the HadDelayed stream a 20 GeV lower unrescaled \cancel{E}_T trigger threshold is available. The rate of events accepted by the lower \cancel{E}_T threshold would be too high for the event processing. To enable the lower threshold, events are kept in the pipeline to be processed in time windows with no normal processing.

4.1.2 Simulated Samples

For the studies on the β estimation as well as for the MAg analysis several MC simulated samples are needed, which are presented in the following.

$Z \rightarrow \mu\mu$ Samples

For the studies on the improvement of the β estimation a sample is used containing ~ 1 million $Z \rightarrow \mu\mu$ events. The events are generated with PYTHIA6 [34].

Signal Samples

The signal samples contain events of pair produced gluino, sbottom and stop R -hadrons, respectively. Each signal point gluino R -hadron sample contains 20,000 events, whereas the sbottom and stop R -hadron samples contain only 10,000 events. The events are generated with PYTHIA6 using special routines for the modeling of the hadronization [35]. The "gluinoball" fraction is assumed to be 10% for all gluino mass hypotheses. The interaction of R -hadrons with the detector is simulated with GEANT4 [36] using different scattering models. For gluino R -hadrons the generic scattering model is used, whereas for sbottom and stop R -hadrons the regge scattering model is used. An explanation of both scattering

models can be found in Ref. [10]. The gluino R -hadron samples are produced for mass hypotheses between 100 GeV and 1600 GeV. For sbottom and stop R -hadrons samples are produced, for mass hypotheses between 100 GeV and 1200 GeV.

To be able to compare MC events with data, the MC events have to be weighted according to the expected cross section of the signal and the integrated luminosity of the used data samples. The weight w is given by

$$w = \frac{\int L dt \cdot \sigma}{N} \quad (4.1)$$

with σ being the cross section of the process and N being the number of events in the signal sample.

The signal cross sections are taken from the nominal analysis [1] and are shown in Tab. 4.1.

Mass [GeV]	σ gluino R -hadrons [pb]	σ sbottom/stop R -hadrons [pb]
100	$2.93 \cdot 10^4$	$5.60 \cdot 10^2$
200	$9.35 \cdot 10^2$	$1.85 \cdot 10^1$
300	$9.87 \cdot 10^1$	$2.00 \cdot 10^0$
400	$1.77 \cdot 10^1$	$3.57 \cdot 10^{-1}$
500	$4.21 \cdot 10^0$	$8.56 \cdot 10^{-2}$
600	$1.21 \cdot 10^0$	$2.48 \cdot 10^{-2}$
700	$3.92 \cdot 10^{-1}$	$8.11 \cdot 10^{-3}$
800	$1.39 \cdot 10^{-1}$	$2.89 \cdot 10^{-3}$
900	$5.27 \cdot 10^{-2}$	$1.09 \cdot 10^{-3}$
1000	$2.11 \cdot 10^{-2}$	$4.35 \cdot 10^{-4}$
1100	$8.76 \cdot 10^{-3}$	$1.79 \cdot 10^{-4}$
1200	$3.74 \cdot 10^{-3}$	$7.62 \cdot 10^{-5}$
1300	$1.64 \cdot 10^{-3}$	
1400	$7.25 \cdot 10^{-4}$	
1500	$3.24 \cdot 10^{-4}$	
1600	$1.46 \cdot 10^{-4}$	

Table 4.1: Cross sections for gluino, sbottom and stop R -hadrons.

4.2 Studies on β Estimation

The calorimeters are in primarily not built for precise time measurements. Consequently not much optimization has been done until 2012. Therefore corrections on t_{cell} are discussed in this section. Furthermore possible corrections on the β estimation will be presented.

4.2.1 $Z \rightarrow \mu\mu$ candidate selection

For the validation of the corrections $Z \rightarrow \mu\mu$ candidates in data are used. The selection criteria for the candidates are shown in Tab. 4.2 and are be discussed in the following. The selection criteria follow the recommendations of the ATLAS Muon Combined Group.

Description	Value
Track to Muon match	$N_{\mu}^{track} (\Delta R_{track, \mu} < 0.1) = 1$
Minimum transverse momentum track	$p_T^{track} > 20.0 \text{ GeV}$
Sensible momentum	$20.0 \text{ GeV} < p^{track} < 4.0 \text{ TeV}$
Isolation from high momentum jet	$\Delta R_{jet, p_T > 40.0 \text{ GeV}} > 0.3$
Isolation from high momentum track	$\Delta R_{track, p_T > 10.0 \text{ GeV}} > 0.25$
Central longitudinal and radial vertex position	$ z_0 < 10.0 \text{ mm}, d_0 < 2.0 \text{ mm}$
At least six SCT hits or passed dead sensors	$N_{SCT}^{hits} + N_{SCT}^{dead} > 5$
At least two pixel hits or passed dead sensors	$N_{PIX}^{hits} + N_{PIX}^{dead} > 1$
Less than three pixel and SCT holes	$N_{PIX}^{holes} + N_{SCT}^{holes} < 3$
At least six TRT hits	$N_{TRT}^{hits} > 5$
Two muon candidates	$N_{\mu} = 2$
Invariant mass muons in Z mass window	$ m(\text{cand}(m = m_{\mu}), \mu) - m_Z < 10 \text{ GeV}$

Table 4.2: The $Z \rightarrow \mu\mu$ candidate selection.

Beside the general track quality requirements, described in detail for the MAg analysis in Sec. 4.3.2, some specific criteria are applied for the $Z \rightarrow \mu\mu$ selection. The candidate tracks are required to have exactly one muon candidate reconstructed by the StacoMuon algorithm with $\Delta R < 0.1$. Two candidates with $p_T > 20 \text{ GeV}$ are required in each event. From the two candidates the invariant mass is reconstructed and is required to be within a 10 GeV mass window of the Z boson mass.

4.2.2 Cell-Time Smearing

Motivation

To be able to compare data and MC it is essential that the simulated and measured quantities behave similar. The uncertainty on the t_{cell} measurement estimated from $Z \rightarrow \mu\mu$ MC and data show quite large discrepancies. The t_{cell} distributions for the cell BC8 is shown in Fig. 4.1.

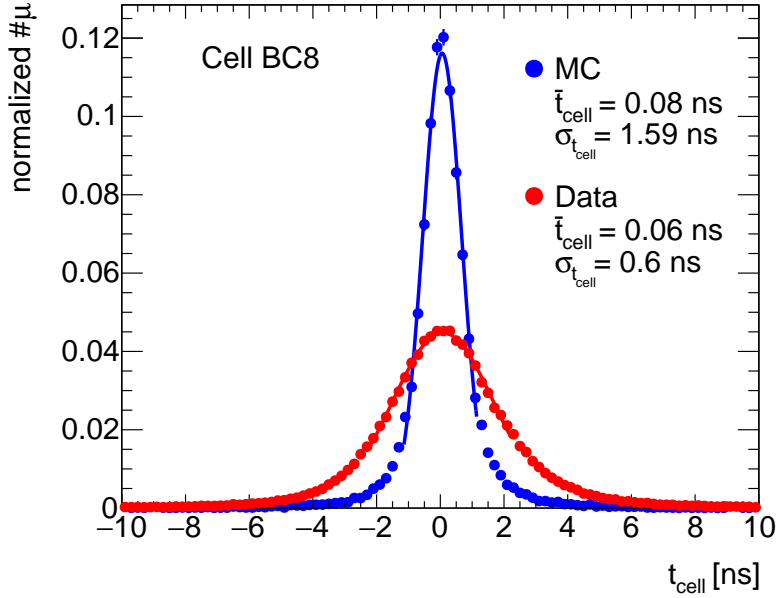


Figure 4.1: t_{cell} distributions for muons from $Z \rightarrow \mu\mu$ MC and data .

For cell BC8 the width of the t_{cell} distribution in data is more than twice the width seen in MC. It is therefore essential to introduce a smearing of t_{cell} . The discrepancy might be due to an incorrect modeling of the produced photons in the tiles and in the wavelength-shifting fibers.

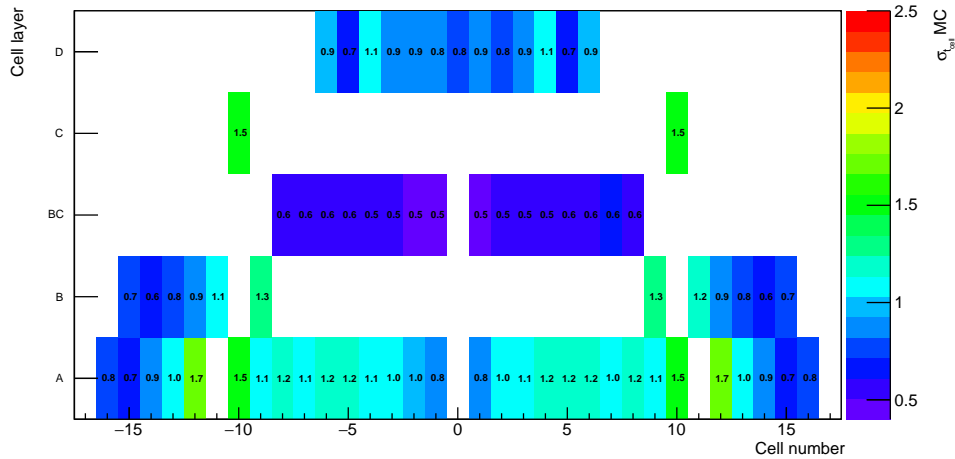


Figure 4.2: Uncertainty on t_{cell} in each cell for MC muons. The labeling of the cells is according to the names in Fig. 3.14.

The differences between data and MC depend on the cell that is considered. This can be seen in Fig. 4.2 and Fig. 4.3. For example for cell D6 the uncertainties differ only by a factor of 1.8, whereas for cell A15 they differ by a factor 3.0. Thus a smearing of t_{cell} has to be done in each cell.

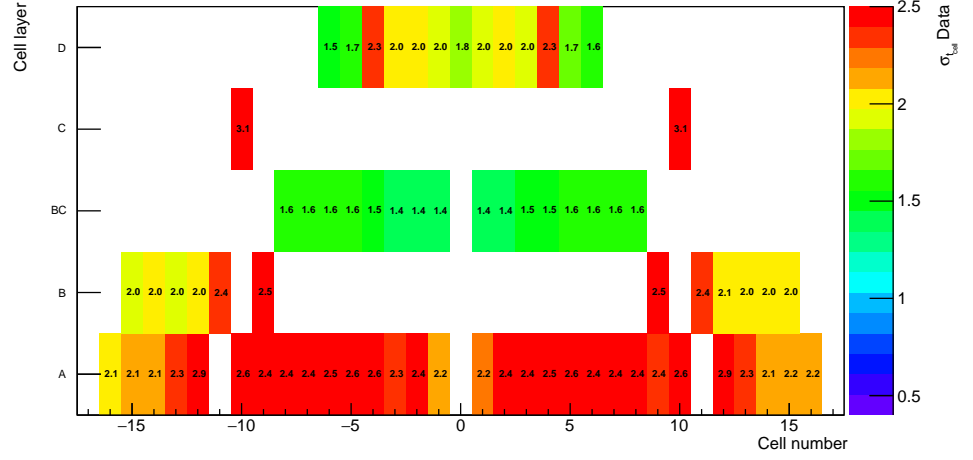


Figure 4.3: Uncertainty on t_{cell} in each cell for data muons. The labeling of the cells is according to the names in Fig. 3.14.

Implementation

The smeared t_{cell} distributions have to have the same Gaussian shape as the initial t_{cell} distribution. It is further assumed that the mis-measurements are normally distributed. Therefore it can be used, that the sum of two independent normally distributed random variables is also normally distributed. For the smearing this means, that the normally distributed t_{cell} in MC (Eq. 4.2) plus a normally distributed smearing factor (Eq. 4.3) should give the normally distributed t_{cell} seen in data (Eq. 4.4).

$$t_{cell,MC} \sim N(\bar{t}_{cell,MC}, \sigma_{t_{cell,MC}}^2) \quad (4.2)$$

$$t_{smear} \sim N(\bar{t}_{smear}, \sigma_{t_{smear}}^2) \quad (4.3)$$

$$t_{cell,MC} + t_{smear} = t_{cell,Data} \sim N(\bar{t}_{cell,MC} + \bar{t}_{smear}, \sigma_{t_{cell,MC}}^2 + \sigma_{t_{smear}}^2) \quad (4.4)$$

Accordingly the smeared $t_{cell,MC}$ can be calculated with

$$t_{cell,smear} = t_{cell,MC} - (\bar{t}_{cell,MC} - \bar{t}_{cell,Data}) + RndGaus(0, \sigma_{t_{smear}}), \quad (4.5)$$

where

$$\sigma_{t_{smear}} = \sqrt{\sigma_{t_{cell,Data}}^2 - \sigma_{t_{cell,MC}}^2}. \quad (4.6)$$

The *RndGaus* gives a random number following a Gaussian with mean at zero and $\sigma_{t_{smear}}$ as spread. The smeared t_{cell} is consequently obtained from the previously measured mean and uncertainty of t_{cell} in data and MC for each cell.

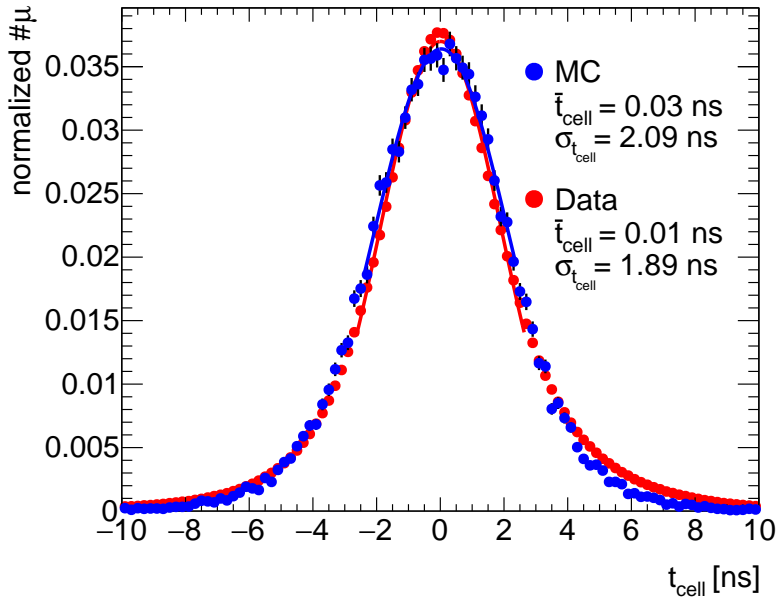


Figure 4.4: The t_{cell} distributions for data and smeared MC for all measurements.

Results

The resulting t_{cell} distribution for all cells is shown in Fig. 4.4.

The distributions for MC and data are in good agreement after the smearing of MC. Some issues still remain as the two distributions have not exactly the same shape. The reason for that is the incorrectly modeled η dependence, which will be discussed later in this section. The smearing is applied similar to the smearing in the nominal analysis [1].

This smearing can also be applied for the signal samples, as the discrepancies seem to arise due to a mis-modeling of the detector and are thus independent of the particle type.

4.2.3 Cell-Time Correction

Motivation

As previously mentioned the t_{cell} estimation using the OF algorithm is optimized for $t_{cell} < 10$ ns. As SMPs are expected to have also longer t_{cell} , the behavior of the estimated β for longer t_{cell} has to be studied. Therefore gluino R -hadron samples are used. The R -hadron candidate tracks are matched to truth particles. This allows a comparison of the truth β_{truth} and the estimated β_{est} . The behavior of $\beta_{est} - \beta_{truth}$ as a function of t_{cell} is shown in Fig. 4.5. For a better visualization $\beta_{est} - \beta_{truth} = \Delta\beta$ is normalized to β_{truth} .

For $t_{cell} < 20$ ns the estimated β looks reasonable. The fluctuations to higher values in the very low t_{cell} region and to lower values in the higher t_{cell} region are due to pile-up. To validate this the events are split in

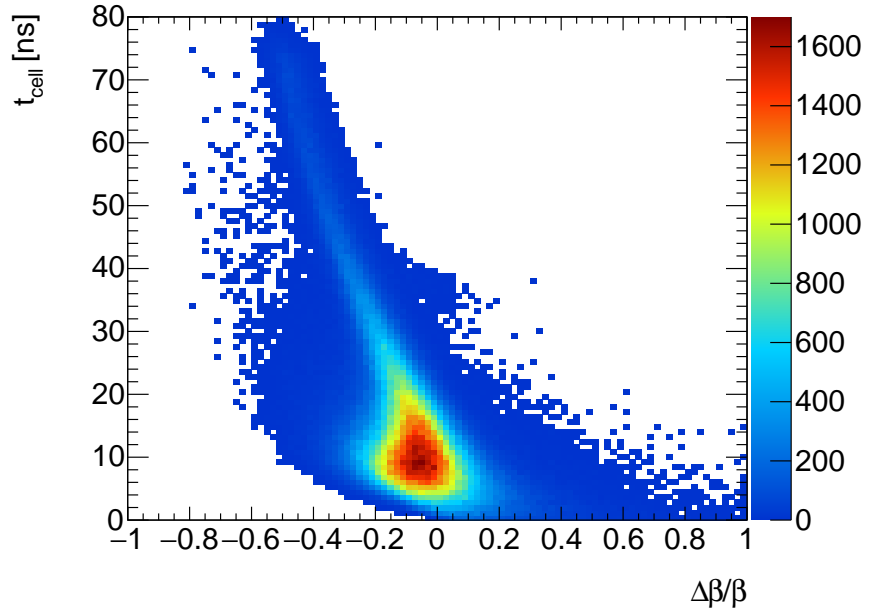


Figure 4.5: $\Delta\beta/\beta$ as function of the cell time. For low cell times the estimated β is reasonable and has only some fluctuations due to pile-up. Whereas for higher cell times the estimated β is to low.

events with high and low pile-up, respectively. High pile-up events are events with more than 23 interactions per bunch-crossing, whereas low pile-up events are required to have less than 23 interactions per bunch-crossing. For events with high pile-up $0.98 \pm 0.02\%$ of all β measurements are in the tail, where $\Delta\beta/\beta > 0.3$, whereas for the events with low pile-up only $0.81 \pm 0.02\%$ are in this region.

For $t_{cell} > 20$ ns a bias of $\Delta\beta/\beta$ can be seen. This is due to the worse performance of the OF for higher values of t_{cell} . Using a functional parametrization to correct for the deviation from $\Delta\beta = 0$ was suggested in Ref. [3]. The implementation of this correction will be presented in the following.

Implementation

To correct for the tail seen in Fig. 4.5 the form has to be functionally parametrized. To use the parametrization for the correction, $\beta_{est} - \beta_{truth}$ is not normalized by β_{truth} , as shown in Fig. 4.6 (left). The histogram is divided into slices along the t_{cell} axis. Each slice is fitted with a Gaussian function, shown in Fig. 4.6 (right). The mean of the Gaussian is used as point for the parameterization $f(t_{cell})$ of the deviation from $\Delta\beta = 0$. The computer program *Eureqa* [37] is used to obtain $f(t_{cell})$. *Eureqa* combines user given mathematical blocks as $+$, $-$, $*$, $/$, \cos , ... to fit multidimensional data points. The combination of these blocks is performed by genetic algorithms. These algorithms optimize the fit on the basis of complexity and fit quality by mating, mutating and terminating the expressions. The best compromise between fit quality and complexity for

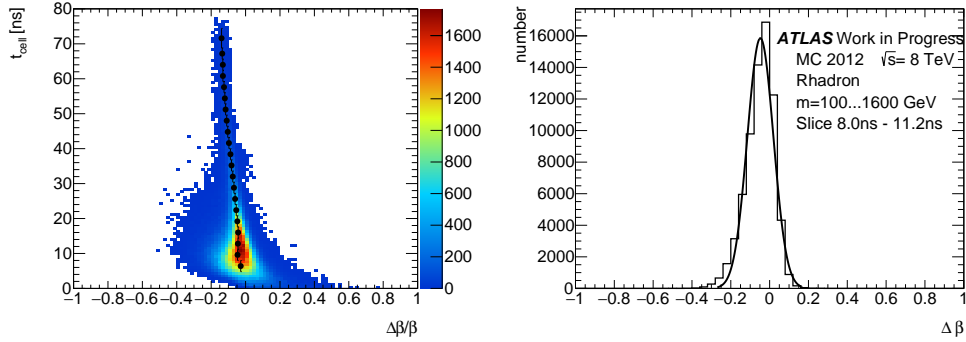


Figure 4.6: $\beta_{est} - \beta_{truth}$ as function of the cell time with the points of the gaussian fits (left). The Gaussian fit of one slice in t_{cell} (right).

the fit to the points shown in Fig. 4.6 (left) represents

$$f(t_{cell}) = -0.0212 - 0.00175t_{cell} - 0.00579\cos(-0.127t_{cell}). \quad (4.7)$$

This is used to calculate the corrected β with

$$\beta_{cor}(t_{cell}) = \beta_{est} - f(t_{cell}). \quad (4.8)$$

Results

The corrected distribution is shown in Fig. 4.7. The β -resolution is now centered around zero and thus no bias of β is left. For the combined β estimation (Fig. 4.8) it can be seen, that this correction is important, as the long tail to low β_{est} is gone as expected. Further the mean of the distribution is almost at zero for the corrected β . The influence of this correction on the β estimation for muons as main background is shown in Fig. 4.9. In data as well as in MC the width of the β distributions are slightly smaller.

All in all the time correction applied to β improves the estimate significantly for signal and also slightly for background candidates.

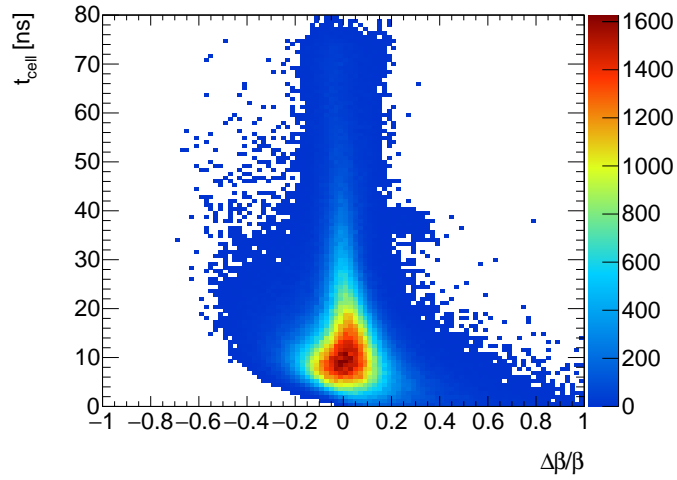


Figure 4.7: $\Delta\beta/\beta$ as function of the cell time for the time corrected β .

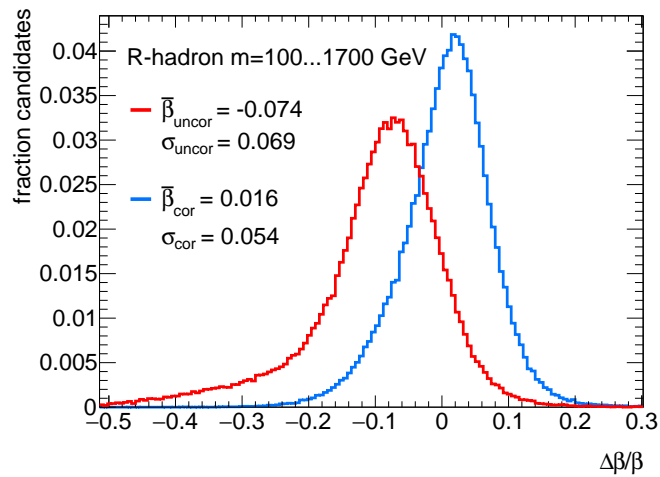


Figure 4.8: β resolution for Rhadron candidates with and without time correction.

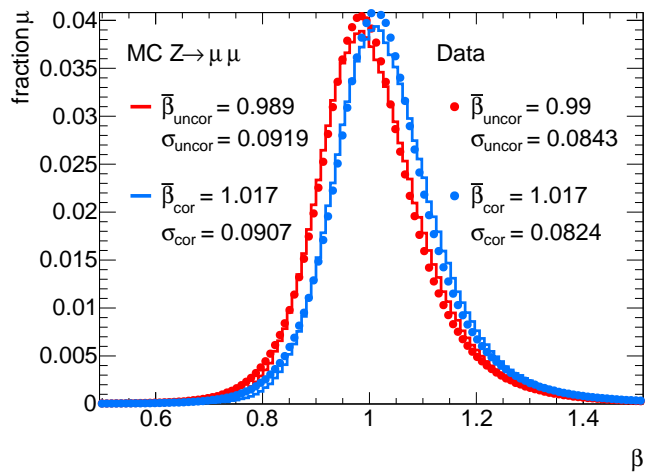


Figure 4.9: β distribution for muon candidates from $Z \rightarrow \mu\mu$ in MC and data with and without the time correction. The β distribution looks basically the same as the β -resolution distribution for muons as they are expected to have $\beta_{truth} = 1$.

4.2.4 Dimension Correction

Motivation

One assumption of the standard β estimation is, that the particles fly through the center of the cell. Accordingly the t_{cell} is assumed to be measured at the cell center. For cells with a size up to $1 \text{ m} \times 1.5 \text{ m}$ this does not hold and a dependence of β_{est} on the incidence angle is expected.

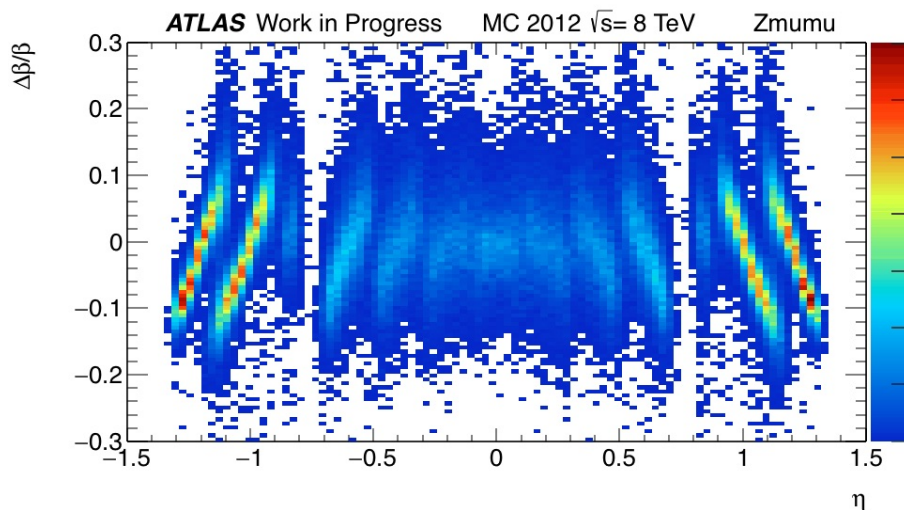


Figure 4.10: The β -resolution as a function of η for the cells of the D layer.

This dependence is shown in Fig. 4.10 for the cells of the outermost layer. The variation is most pronounced for the outer cells $\pm D5$ and $\pm D6$. This is in good agreement with the expectations as these are the largest cells. In Ref. [3] a fit correction for the bias of β_{est} as function of η in each cell is suggested. I developed a correction that is based on the length of the track in the cell, which does not need any previous parametrization for the correction. The implementation of both methods will be explained in the following.

Implementation

The fit correction for the η dependence works similar for the fit correction for the time dependence. The histogram of $\Delta\beta$ as a function of η is divided into slices in η . Each slice is fit with a Gaussian function. The means of the Gaussians are parametrized with

$$f(\eta) = \frac{-p_0 + p_1 + \eta}{p_1}. \quad (4.9)$$

The parameters are estimated for each cell separately. β is then corrected with Eq. 4.10 according to the cell passed.

$$\beta_{cor} = \beta_{est} - f_{cell}(\eta) \quad (4.10)$$

The correction that uses the length of the tracks in the cell is from now on referred to as DistCor. The DistCor uses the trajectory of the track to reconstruct the position where t_{cell} is actually measured. For a particle with speed-of-light traversing the center of the cell, the center is the position, where the time is measured. The idea is, that the position, where t_{cell} is actually measured, is at the same phase of the track in the cell, as the cell center on a track through the center of the cell. This

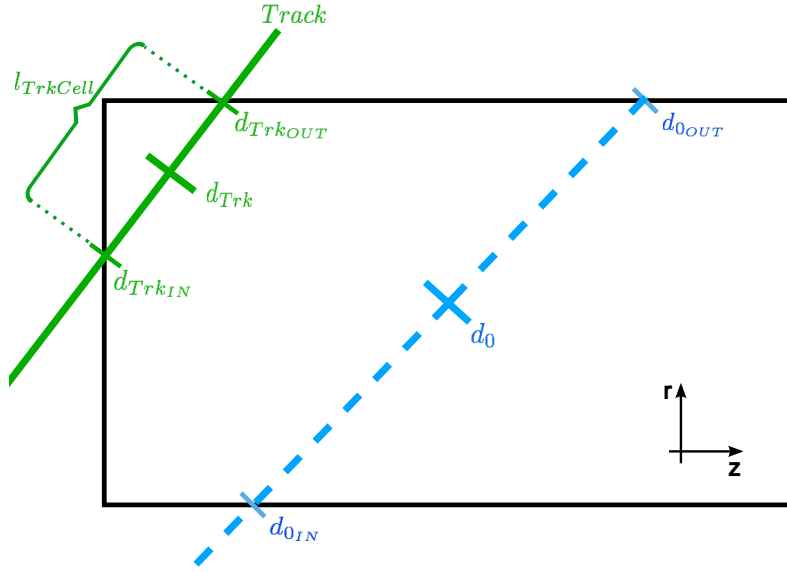


Figure 4.11: The reconstructed position d_{trk} of the time measurement for a particle following the green track. The blue dashed line refers to a particle traveling with the speed-of-light traversing the cell center.

is illustrated in Fig. 4.11. As the cells have a rectangular shape, the center of the cell is always at the half length of the track in the cell. The position, where t_{cell} is measured, is therefore at the half length of the track in the cell. For the new distance two things have to be calculated: The length of the track in the cell ($l_{TrkCell}$) and the distance of the IP to entrance point of the particle in the cell ($d_{Trk,In}$). The exact positions and the dimensions of the cells are known. From the dimension and the position of the cell, the length of the track as well as $d_{Trk,In}$ can be calculated from geometrical considerations. The new distance for the β measurement is given by

$$d_{cor} = d_{Trk,In} + \frac{l_{TrkCell}}{2}. \quad (4.11)$$

This works well for all cells except the cells those in sampling 13 due to their different shape. The cells of sampling scheme 13 (see Fig. 3.14) are basically two shifted rectangular cells, as illustrated in Fig. 4.12. It can be seen, that a track of a particle can have two separated parts in the cell. To estimate the new distance in that case, two signal pulses are considered shifted by the time difference between the peaks in the two cells. The new distance can be estimated from the peak of the summed

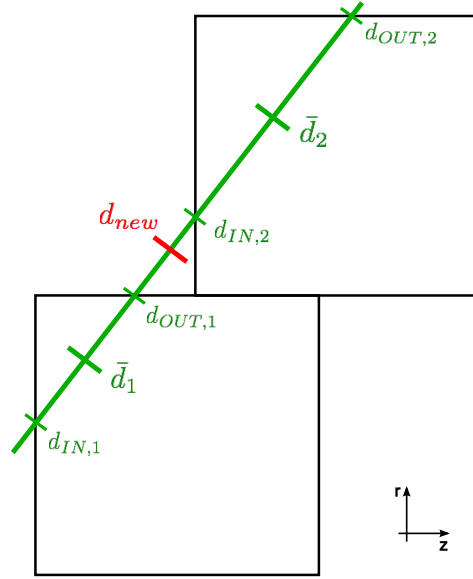


Figure 4.12: The shape of a cell of sampling scheme 13 (see Fig. 3.14) with a particle track traversing the cell. All important positions on the track for the estimation of d_{new} are labeled.

pulse signals. The signal pulse shape is measured in dedicated calibration runs. The pulse shape was functionally parametrized using Eureqa. The resulting parametrization for a signal amplitude of one is

$$f(t) = e^{\frac{-t^2}{(41.5+0.16t)^2}} \quad (4.12)$$

As the estimation of the peak with this parametrization is only possible numerically, a Gaussian function was used instead. The parametrization with a Gaussian is given by

$$f(t) = e^{\frac{-t^2}{44.4^2}}. \quad (4.13)$$

That this simplification is reasonable can be seen in Fig. 4.13. It shows

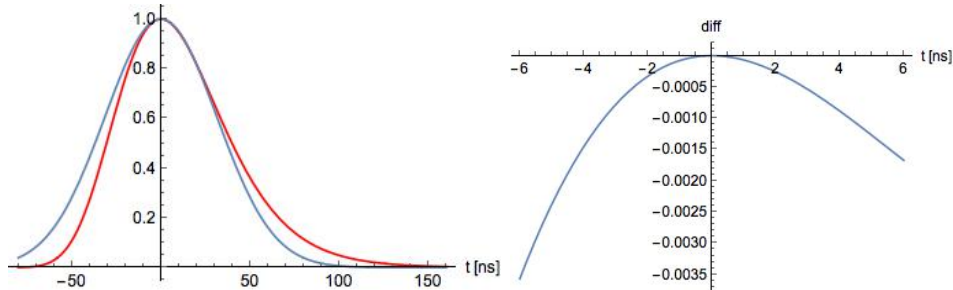


Figure 4.13: The pulse shape obtained with Eureqa (red) and the Gaussian (blue) in the left figure. The difference between the shape from Eureqa and the Gaussian in the right figure.

the two considered pulse shape functions in the left plot. It can be seen, that the deviation in the peak region is very small whereas the differences in the tails are larger. The difference in the peak region is shown in the right figure. As the distance between the peaks does not exceed 0.5 m

the time difference between the peaks for a particle flying with $0.3 c$ is about 5 ns. From Fig. 4.13 right it can be seen that for this case the deviation is far below 1 %. The assumption to use a Gaussian is hence reasonable. The combined pulse is accordingly given by

$$f_{comb}(t) = Ae^{\frac{-t^2}{44.4^2}} + Be^{\frac{-(t-b)^2}{44.4^2}}, \quad (4.14)$$

with A the amplitude of the first pulse, B the amplitude of the second pulse and b the time difference between the pulses. The peak of the first pulse is set to zero as only the difference between the pulses is of interest. The peak can be calculated from the derivative of the combined pulse function with

$$\frac{df_{comb}(t)}{dt} = -\frac{2At}{44.4^2}e^{\frac{-t^2}{44.4^2}} - \frac{2B(t-b)}{44.4^2}e^{\frac{-(t-b)^2}{44.4^2}} \stackrel{!}{=} 0. \quad (4.15)$$

The difference between the single pulses should not be significantly more than 5 ns as previously mentioned. Thus the peak of f_{comb} should not differ more than 3 ns from the single peaks. This allows to set the exponential parts to one as the exponents are almost zero. Therefore Eq. 4.15 reduces to

$$-At - B(t-b) \stackrel{!}{=} 0. \quad (4.16)$$

The time of the combined peak is then given by

$$t_{Peak} = \frac{bB}{A+B}. \quad (4.17)$$

The amplitudes of the signals are a measure for the energy deposit in the cell. With the assumption of a constant dE/dx in the cell, the length of the track in the cell can be used instead of the amplitude in Eq. 4.17. It is further assumed, that β does not change significantly in the cell. With $d_{new} = \beta t_{peak}$ and $\bar{d}_2 - \bar{d}_1 = \beta b$, the new distance for the β estimation is given by

$$d_{new} = \bar{d}_1 + \frac{(\bar{d}_2 - \bar{d}_1)l_2}{l_1 + l_2}. \quad (4.18)$$

Where $l = d_{OUT} - d_{IN}$ states the length of the track in the cell. Hence an estimation of a corrected distance for all cells of the TileCal is possible. The corrected β can be estimated by

$$\beta_{cor} = \frac{d_{new}}{t_{cell}c + d_{cell}}. \quad (4.19)$$

Results

To understand the influence of the corrected distance, Figs. 4.14 and 4.15 show d_{new} and d_{center} in the direction of the trajectory of the particle. The dimension of the cell are shown with the entrance and exit points of

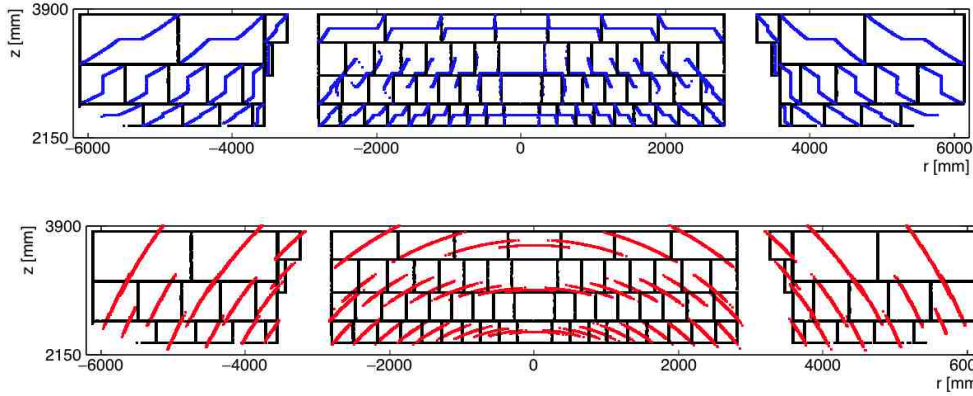


Figure 4.14: The TileCal cells in z - r -plane in black and in blue d_{new} in the direction of the trajectory of the particle.

Figure 4.15: The TileCal cells in z - r -plane in black and in red the distance of the IP to the cell center in direction of the trajectory of the particle.

the particles in the cell (black).

The new distance as a function of η in each cell has three different regions according to the side of the entrance and exit, respectively. It can be further seen, that for the cells of sampling scheme 13 (see Fig. 3.14) some of the d_{new} values seem to fluctuate. This is due to tracks hitting only one part of the two-parted cell. The signal stops at a certain angle in cell $\pm A16$. The reason for that is the requirement for the candidates to have $\eta < 1.65$.

It is further interesting to consider the difference between d_{center} and d_{new} as a function of η , shown in Fig. 4.16.

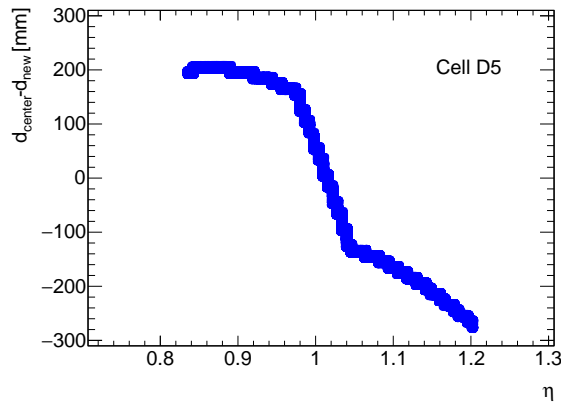


Figure 4.16: Difference between d_{center} and d_{new} as a function of η for cell D5.

It shows the difference between the actual position where t_{cell} is measured and the position that was used for the β estimation in the nominal analysis. It can be seen, that the distribution is asymmetric in $d_{center} - d_{new}$. The high η region differs by up to ~ 300 mm, whereas the low η region only differs by up to ~ 200 mm. The cell times are accordingly quite asymmetric especially in the outer cells. This means, that the mean of t_{cell} is expected to be shifted for these cells.

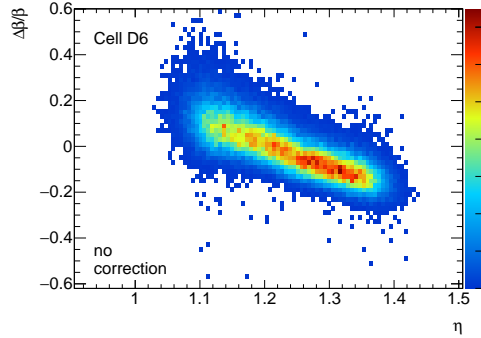


Figure 4.17: Distribution of the uncorrected $\Delta\beta/\beta$ as function of η for cell D6 in MC.

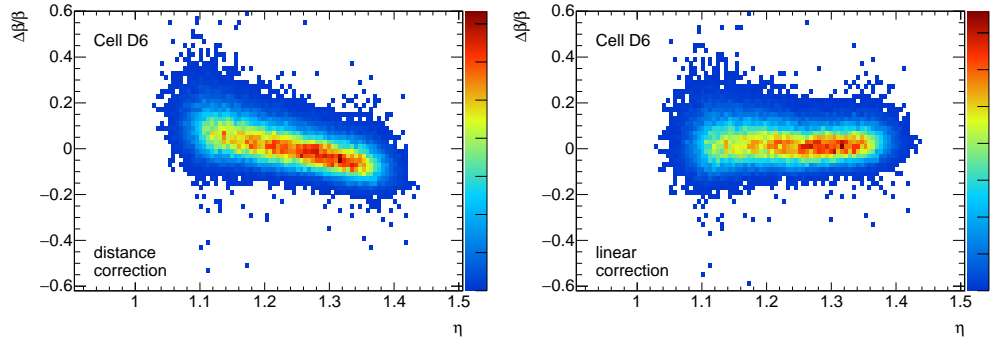


Figure 4.18: Distribution of $\Delta\beta/\beta$ with the distance correction (left) and the linear correction (right) as function of η for cell D6 in MC.

As the effect of the distance correction on the β estimation is strongest for the outermost cells, D6 is used for the interpretation of the results of the corrected β . The uncorrected β shows a bias as a function of η , shown in Fig. 4.17. The influence of the linear correction and the distance correction on the β estimation in MC is shown in Fig. 4.18. It can be seen, that for the linear correction no bias remains, whereas the distance correction only slightly improves the β estimation as the deviations are smaller, but a correlation between $\beta_{DistCor}$ and η remains.

The correlation between β and η can be also seen in data for muons passing the $Z \rightarrow \mu\mu$ selection. The uncorrected β as a function of η is shown

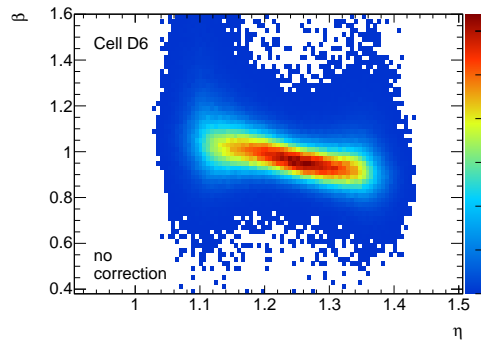


Figure 4.19: Distribution of uncorrected β as function of η for cell D6 in Data.

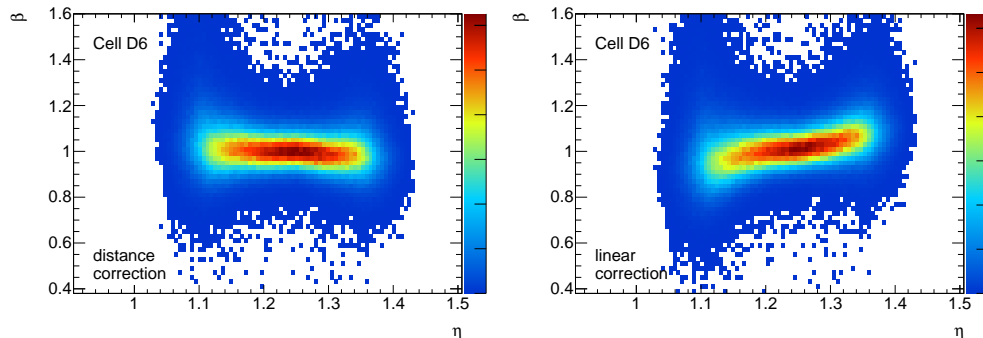


Figure 4.20: Distribution of β with the distance correction (left) and the linear correction (right) as function of η for cell D6 in Data.

in Fig. 4.19. Also in data it can be seen, that β differs from β_{truth} which is basically one for muons. In data the bias can be corrected with the distance correction, shown in Fig. 4.20 (left). The linear correction corrects too much, so that the slope is overcompensated, shown in Fig. 4.20 (right). It can be further seen, that the distributions of β uncorrected and β_{LinCor} have different slopes in the high and low η region compared to the middle region, as expected from the distance correction.

Consequently, the distance correction works fine, the problem is more the incorrect simulation of t_{cell} in MC. The problem might be the correct modeling of the photon path in the tiles as well as in the wavelength-shifting fibers. To understand these differences a dedicated simulation of a particle in a TileCal cell should be performed. This was not possible as a part of this work. As the discrepancy between data and MC might be a mis-modeling of the readout the deviation is assumed to be model independent and therefore similar for muons and R -hadrons .

Fig. 4.21 shows the β -resolution with (right) and without (left) time correction for R -hadrons in cell D6. It can be seen that the fluctuations to smaller values of β are corrected with the time correction. For $\beta_{DistCor}$, shown in Fig. 4.22, a very similar bias as shown in Fig. 4.20 (left) for muons remains. Fig. 4.23 shows β_{LinCor} with (right) and without (left) time correction. Also for R -hadrons , the linear correction overcompensates the bias. This is expected as the DistCor takes into account that a R -hadron with a significantly lower β needs a different time for the distance between d_{new} and d_{center} . The LinCor by contrast is only a correction on β and therefore corrects equally for all particles.

The combined β for muons and R -hadrons is shown in Fig. 4.24 and Fig. 4.25, respectively. It can be seen that for both particles the β resolution is improved using DistCor. The agreement between data and MC is reasonable for the distance corrected β due to the distance corrected smearing that will be introduced in the following section.

Figure 4.21: $\Delta\beta/\beta$ with β_{uncor} (left) and $\beta_{TimeCor}$ (right) as function of η in cell D6 for R -hadrons $m_{\tilde{g}} = 100 \text{ GeV} \dots 1600 \text{ GeV}$.

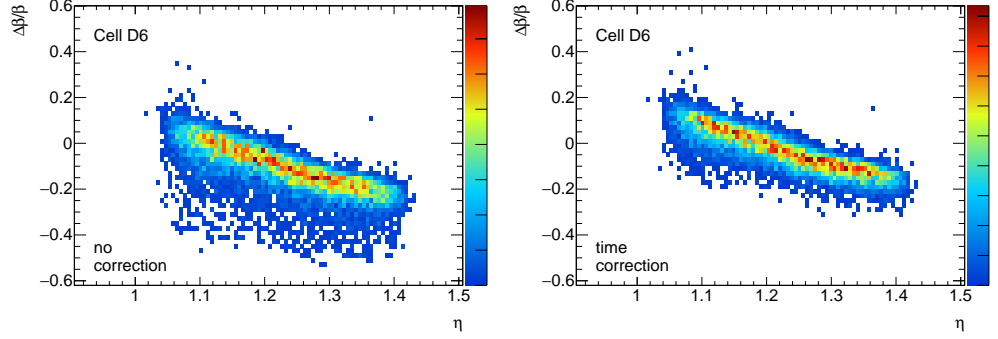


Figure 4.22: $\Delta\beta/\beta$ with $\beta_{DistCor}$ (left) and $\beta_{DistCor+TimeCor}$ (right) as function of η in cell D6 for R -hadrons $m_{\tilde{g}} = 100 \text{ GeV} \dots 1600 \text{ GeV}$.

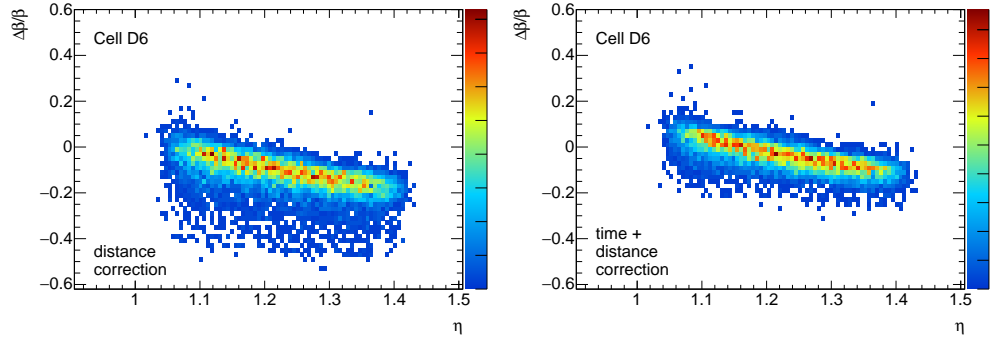
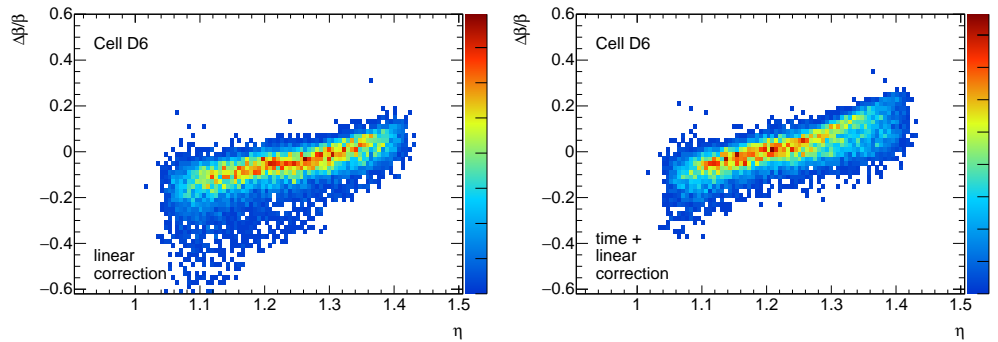


Figure 4.23: $\Delta\beta/\beta$ with β_{LinCor} (left) and $\beta_{LinCor+TimeCor}$ (right) as function of η in cell D6 for R -hadrons $m_{\tilde{g}} = 100 \text{ GeV} \dots 1600 \text{ GeV}$.



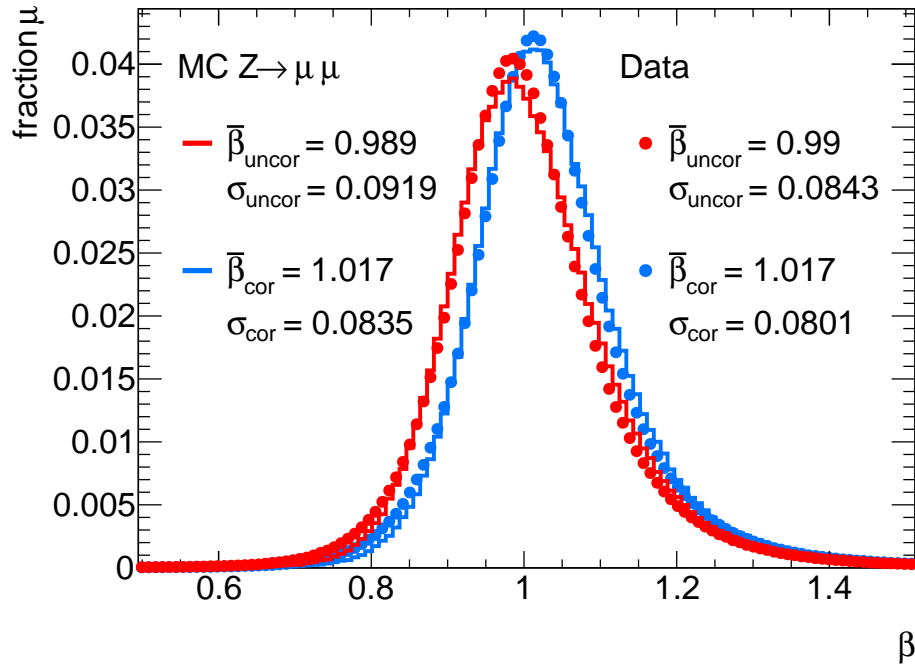


Figure 4.24: β distribution for $Z \rightarrow \mu\mu$ muon candidates in data and MC with and without DistCor + TimeCor.

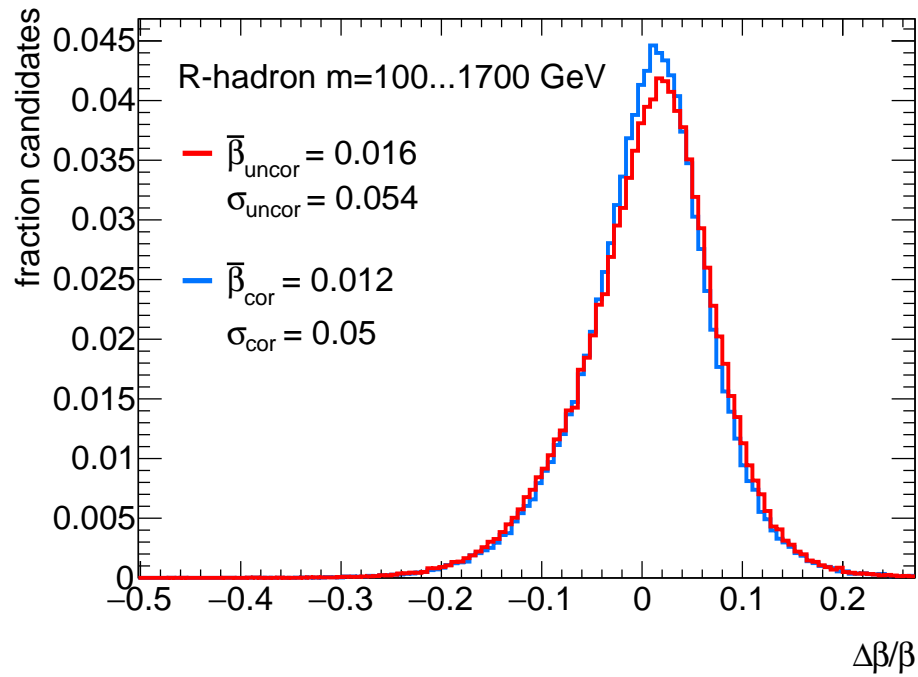


Figure 4.25: β resolution for time corrected R-hadron candidates with and without DistCor.

4.2.5 Distance Corrected Smearing

Motivation and Implementation

The agreement between data and MC with the smearing introduced in Sec. 4.2.2 is not good as the bias of t_{cell} is not correctly modeled. This can be seen in Fig. 4.26. In particular the distribution of $\beta_{DistCor}$ differs

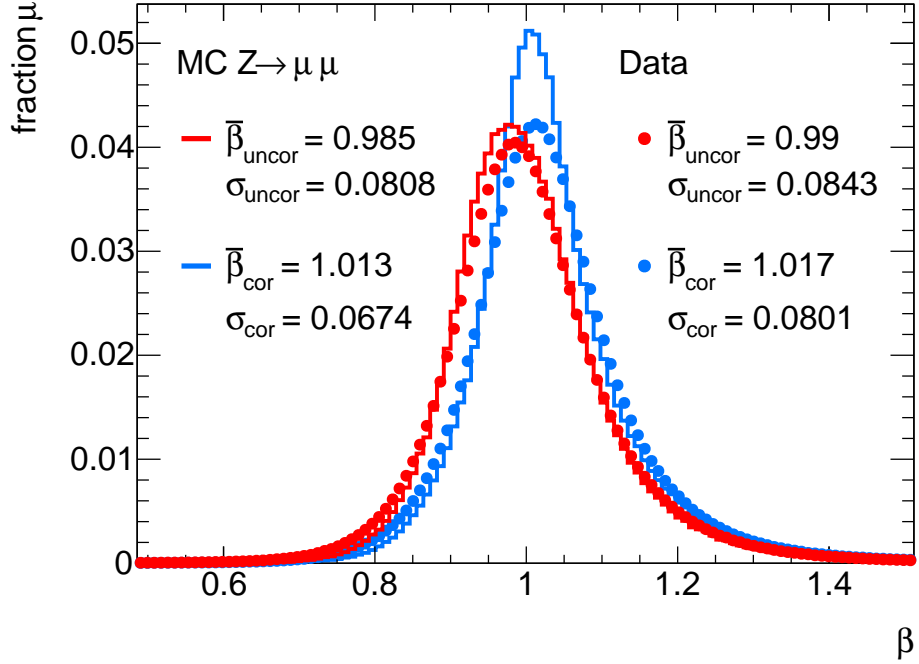


Figure 4.26: β distribution for $Z \rightarrow \mu\mu$ muon candidates in data and MC with and without DistCor + TimeCor. For MC the nominal smearing is used.

significantly between MC and data.

t_{cell} is not measured at the same distances. This means, that t_{cell} also has a bias. One nice side effect of the distance correction is, that it also allows to correct the bias of t_{cell} . The idea is to correct t_{cell} to be measured for all incident angles at the distance of the cell center. The time-of-flight for the distance between d_{new} and d_{center} is therefore subtracted from t_{cell} to obtain $t_{cell,cor}$. Using β_{est} , $t_{cell,cor}$ can be calculated as

$$t_{cell,cor} = t_{cell} + \frac{d_{new} - d_{center}}{\beta_{est}c}. \quad (4.20)$$

The t_{cell} smearing is then applied with the mean and RMS values obtained from the $t_{cell,cor}$ distributions.

Results

The distributions of t_{cell} corrected and uncorrected in MC and data are shown in Fig. 4.27. The $t_{cell,uncor}$ distribution in MC has a double peak.

This is understandable, as the difference between d_{new} and d_{center} as a function of η is more flat in the upper and lower region in η as in the middle, shown in Fig. 4.16. Therefore also in high and low t_{cell} region more measurements are expected than in the central region. For $t_{cell,cor}$ the distribution has one narrow peak. Also in data the correction reduces the t_{cell} uncertainty.

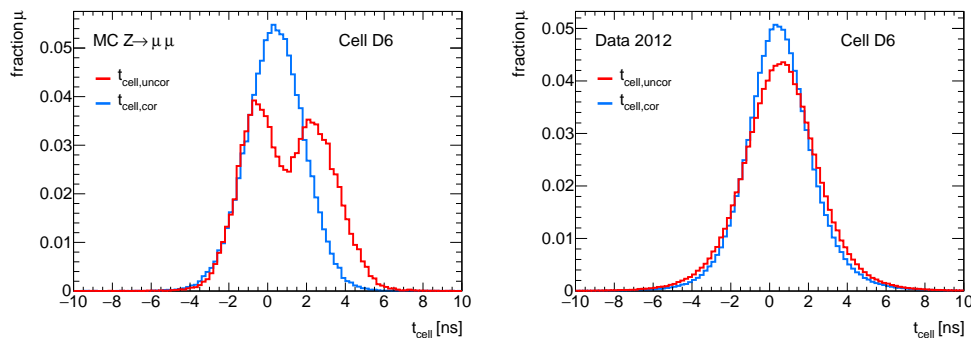


Figure 4.27: The distribution of $t_{cell,uncor}$ and $t_{cell,cor}$ in cell D6 for $Z \rightarrow \mu\mu$ muons in MC (left) and data (right).

The results of the time corrected smearing on the estimated β are shown in Fig. 4.24. It can be seen, that the β -resolution in MC is worse than in data. This ensures that the β -resolution in the signal samples is not underestimated. In the analysis MC is only used for the limit setting with the signal samples. The signal is expected to be at lower β , this means that especially the tail to high values of β should not be underestimated in MC. Also this is accomplished with the distance corrected smearing. All in all the distance corrected smearing is a conservative method ensuring no overestimation of the signal β resolution.

4.2.6 Primary Vertex Shift Correction

Motivation and Implementation

The length used for the β estimation can not only differ due to the incident angle in the cell, also the starting point of the track can differ as the vertex associated to the track of the particle can differ from the origin of the ATLAS coordinate system. The spread of the primary vertices in x and y is of the order of $15 \mu\text{m}$ due to the beam size $\sigma^* = 16.6 \mu\text{m}$, whereas the spread in z direction is a few cm due to the length of the bunches $\sigma_z = 7.55 \text{ cm}$. Hence a significant spread for the origin of the tracks in z -direction is expected, whereas the differences in x - and y -direction are negligible. The z_0 position for candidate tracks is shown in Fig. 4.28. It can be seen, that the z_0 position of tracks varies by up to 15 cm. Therefore it makes sense to include the z_0 -position into the estimation of d_{new} . This is done by calculating the path in the cell for the trajectory starting at the actual z_0 position. The z_0 -corrected distance

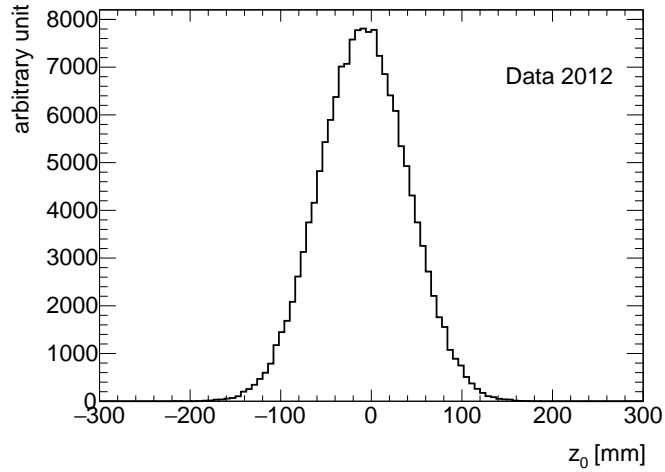


Figure 4.28: z_0 spread of candidate tracks.

is then calculated the same way as d_{new} for the DisCor and can be used for a corrected β estimate.

Results

The resulting β distribution in MC and $Z \rightarrow \mu\mu$ enriched data is shown in Fig. 4.29. It can be seen, that the distance corrected β distribution and the z_0 -distance corrected β distribution have only very little differences. The correction does not play an important role, as not only the end of the track at the IP is shifted also the peak position in the cell is shifted. Therefore the correction for the distance is basically only the relative d_{new} difference between the unshifted peak position and the z_0 shifted peak position. Anyway a slightly improved β resolution can be seen. Consequently the z_0 correction can, but not necessarily must be applied at the moment. As the bunch length might be elongated to achieve higher luminosities for the LHC, this correction may play a more important role in future runs.

4.2.7 Cell Time Uncertainty

Motivation and Implementation

The distance corrected t_{cell} has further possible applications. One possibility is to estimate a corrected t_{cell} uncertainty. Therefore the scatter plot of the corrected t_{cell} as a function of the energy deposit in the cell E is divided into slices. Each slice is fitted with a Gaussian function and the standard deviation is used as the uncertainty of t_{cell} . The time uncertainty can be parametrized following Ref. [22] with

$$\sigma_{t_{cell}} = \sqrt{\left(\frac{p_1}{\sqrt{E}}\right)^2 + \left(\frac{p_2}{E}\right)^2}. \quad (4.21)$$

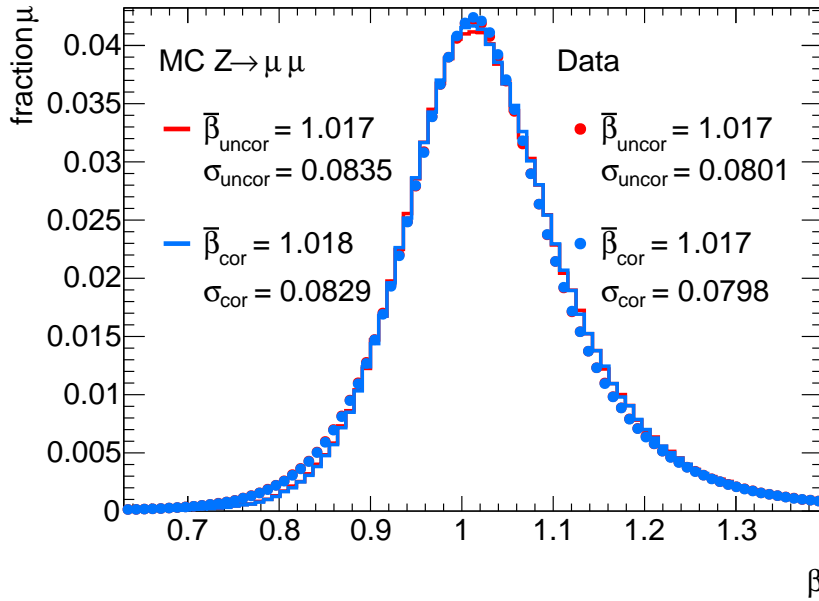


Figure 4.29: β distribution for $Z \rightarrow \mu\mu$ muon candidates in data and MC with and without z_0 correction.

The two contributions to Eq. 4.21 are the statistical uncertainties (first term) and electronics noise (second term).

Results

The differences between the uncorrected and the corrected $\sigma_{t_{cell}}$ as a function of the energy deposit in the cell are shown in Fig. 4.30. The relative difference between the uncorrected and the corrected $\sigma_{t_{cell}}$ is more than 5 % for very high energy deposits, while for low energy deposits almost no differences occur. The reason for that is, that the correction is more important for larger cells. For larger cells the path inside the cell is longer and thus also the expected energy deposit is larger.

The resulting functional parametrization of the corrected $\sigma_{t_{cell}}$ as a function of the energy deposit is shown in Fig. 4.31. The error on the single measurements is too small to be seen. In the tail the fit is reasonable, but for low energies the agreement between data and fit is worse. Another possibility would be to use an uncertainty according to each energy bin, but as the discrepancies between data and fit are smaller than the discrepancies due to the bin width, I decided to use the functional parametrization.

The influence on the β estimation is negligible. For the combination with other β measurements a correct estimation of the β uncertainties is essential. Therefore the distance corrected time uncertainty may be worth considering for the combination of β measurements from different detector systems.

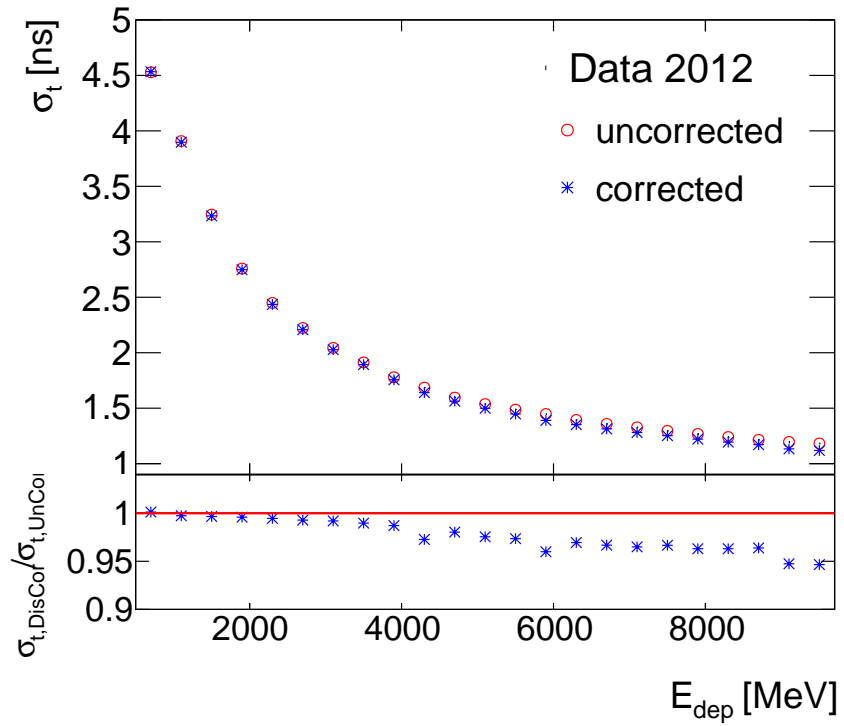


Figure 4.30: $\sigma_{t_{\text{cell}}}$ as a function of E for t_{cell} corrected and t_{cell} uncorrected.

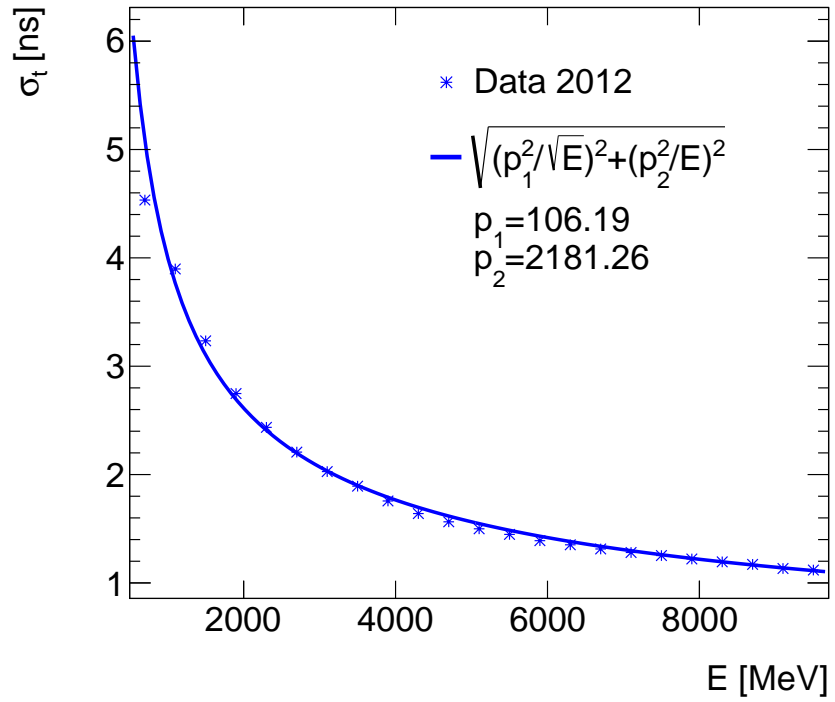


Figure 4.31: $\sigma_{t_{\text{cell}}}$ as a function of E for the corrected t_{cell} with functional parametrization.

4.2.8 Cell-Time Calibrations

Energy-Layer Calibration

In the nominal analysis [1] a calibration of the t_{cell} according to energy deposit in the cell and cell layer is applied. This is done by dividing the measured t_{cell} times in the $Z \rightarrow \mu\mu$ data samples into energy-layer bins. For each of the bins the means are used as calibration constants, and are subtracted from the same energy-layer bins in MC/data samples. A detailed description of the energy-layer calibration can be found in Ref. [38].

This calibration can be dropped as it is redundant with the distance correction. The reason for that is, that the energy is proportional to the length of the tracks in the cell and therefore the bias arises due to the different length from the IP to the t_{cell} measurement point. The layer binning takes the varying cell dimensions in the different layers into account. This means the DistCor delivers a physical interpretation for the energy-layer calibration and further enables to use this calibration. This is very helpful, as it makes the analysis faster and easier.

Runwise t_{cell} shift calibration

Due to a misalignment of the LHC and ATLAS clocks, t_{cell} can have a bias. This is measured with the $Z \rightarrow \mu\mu$ enriched data samples from all t_{cell} measurements with energy deposit $E_{dep} > 500$ MeV in one ATLAS run, shown in Fig. 4.32. It can be seen, that the distribution is slightly

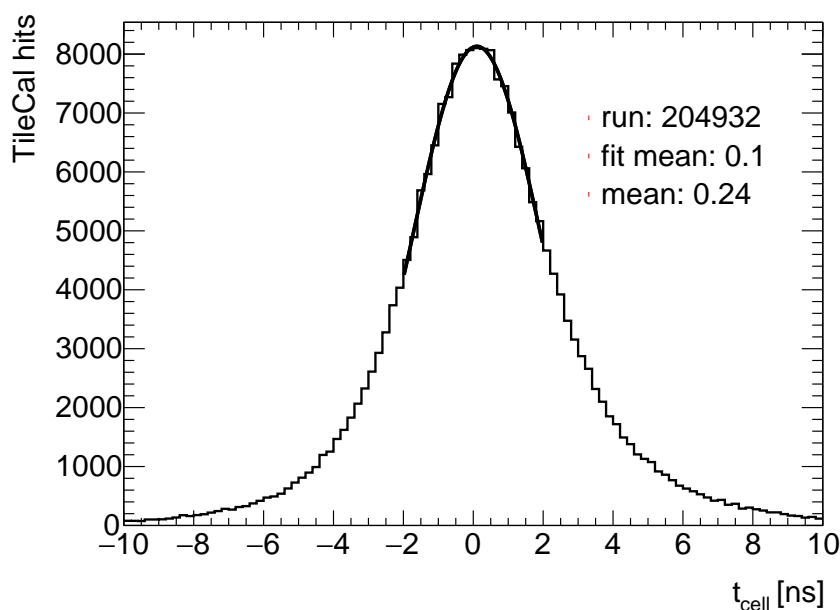


Figure 4.32: t_{cell} distribution for all TileCal hits in run 204932.

asymmetric. This is understandable as on the one hand some cells are expected to have asymmetric t_{cell} distributions according to the asymmetric bias of the distance to the t_{cell} measurement point. On the other hand the mis-measurements due to pileup can cause an asymmetry in the t_{cell} distribution. To introduce no bias, instead of the overall average as used in the nominal analysis, the mean of a Gaussian fit is used as measure for the mis-alignment. The fit is less influenced by the asymmetry and ensures, that no bias is introduced. The means of the Gaussian are centered around zero, as shown in Fig. 4.33, whereas the average means have an average bias of almost 0.15 ns, as shown in Fig. 4.34. Therefore I decided to use the Gaussian fit means for the runwise calibration.

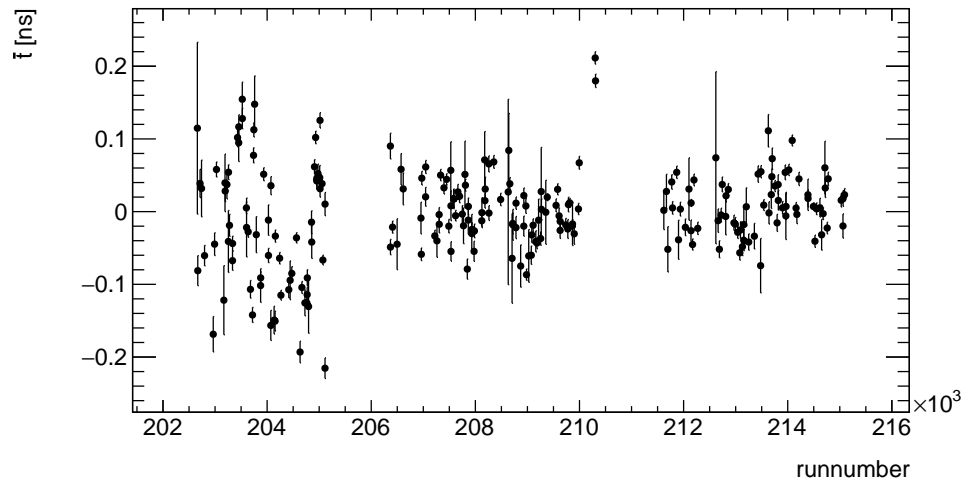


Figure 4.33: Gaussian mean of the t_{cell} distributions as a function of the runnumber.

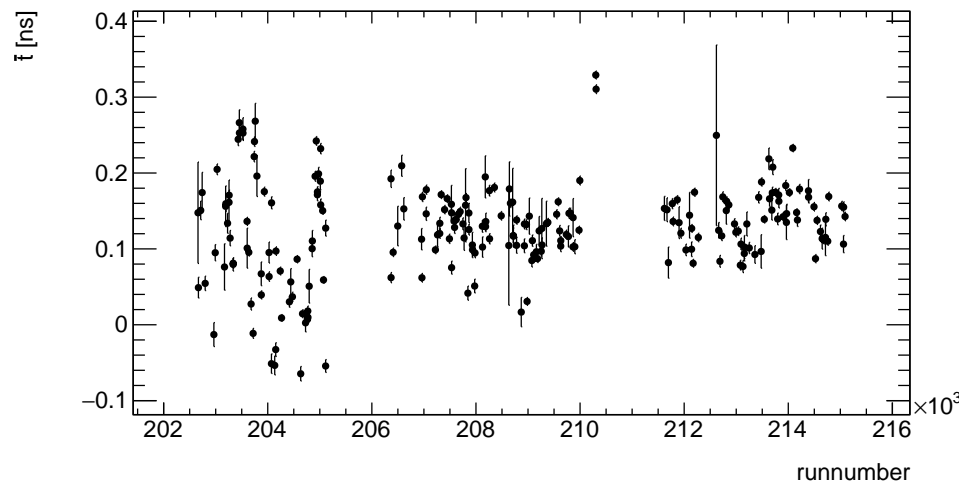


Figure 4.34: Average mean of the t_{cell} distributions as a function of the runnumber.

4.2.9 Liquid Argon Calorimeter β estimation

One possibility to have more β measurements is to include the LAr calorimeter cells in the β estimate. The LAr calorimeter cells are smaller and closer to the IP. Therefore a significantly worse β -resolution is expected for LAr cells. The β distributions with and without LAr cells included is shown in Fig. 4.35. For the LAr no dimension corrections

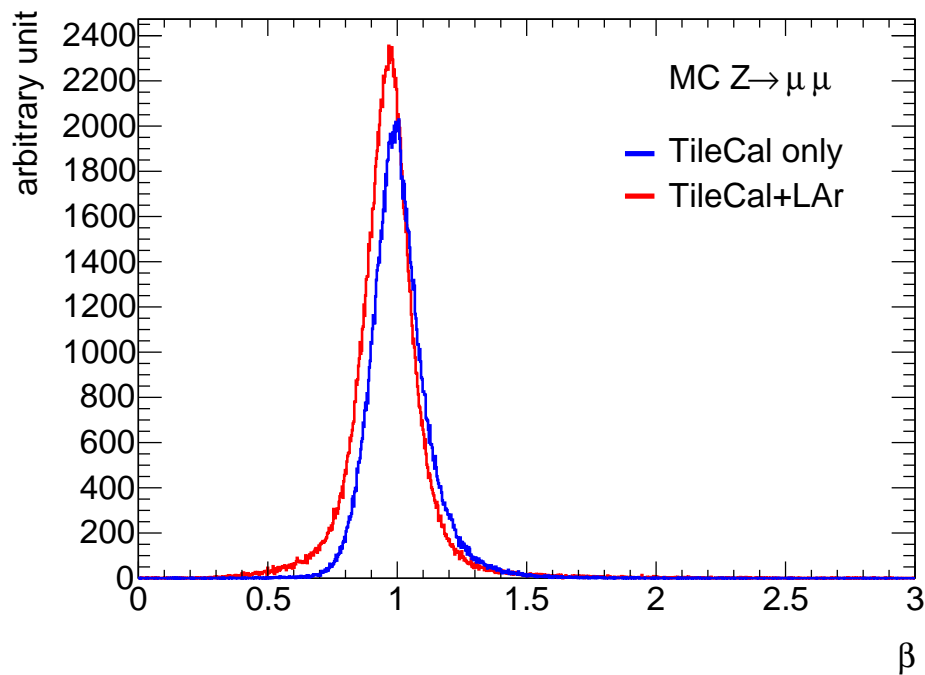


Figure 4.35: β distribution for the TileCal only and with the LAr included.

are applied. Due to their projective design and the small cell size this is not necessary. It can be seen, that more candidates with the LAr cells included in the β estimation survive the pre-selection. But especially in the low- β region the LAr-included β estimate has way more entries. All in all more outliers can be seen for the LAr-included β estimate. Consequently I decided to not use the LAr cells for the β estimate. Dedicated studies on the LAr β measurement could improve estimate, so that it might make sense to include them in the future.

4.2.10 Summary

Several improvements for β estimation with the calorimeters were considered. A parametrization of the bias for high values of t_{cell} was applied. Further the differences in the point of the t_{cell} measurement were corrected. According to this a distance corrected smearing was introduced enabling a good agreement between data and MC. Also the z_0 position of the track was included in the β estimation. The influence of the t_{cell}

distance correction on the parametrization of $\sigma_{t_{cell}}$ as a function of the energy deposit was studied and found to be almost negligible. Further the influence of the corrections on the time calibration in the nominal analysis was studied. The energy-layer calibration can be dropped as it is redundant with the DistCor. Also the runwise t_{cell} calibration due to the unsynchronized ATLAS clock with respect to the LHC clock is improved, as the nominal method is influenced by expected asymmetries in the tails. All in all, the β resolution, including the considered improvements, is 0.08. Compared with the β -resolution in the nominal analysis of 0.79 this is almost the same, but in the nominal analysis the β -consistency requirement was implemented, which was dropped for these studies. The drop of the consistency cut will be discussed later on. The β distribution including the β -consistency cut for data candidates is shown in Fig. 4.36. Consequently with comparable candidate selection the β -resolution was improved by 17% compared to the nominal analysis.

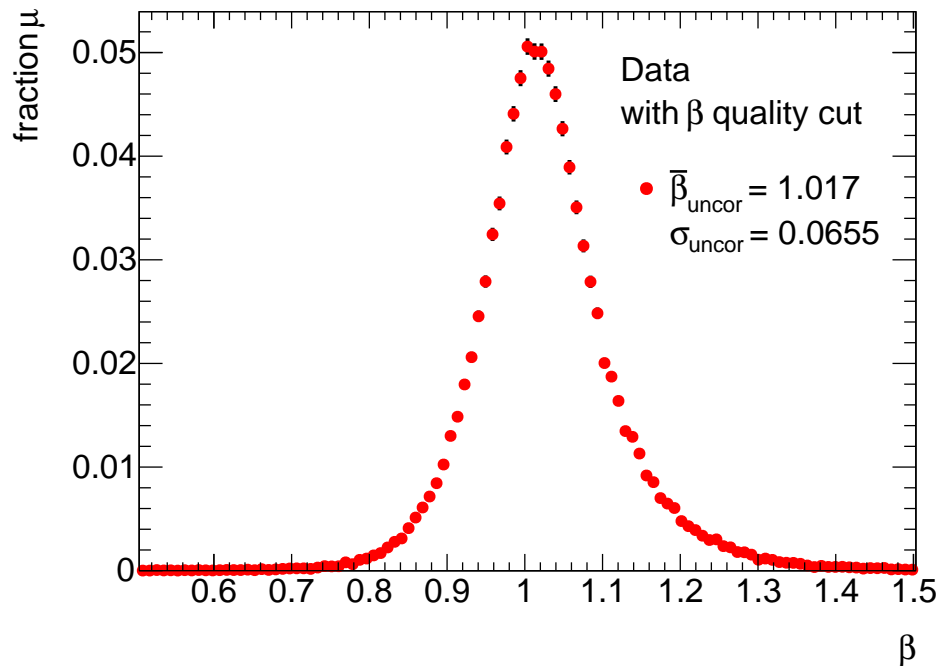


Figure 4.36: β distribution $Z \rightarrow \mu\mu$ muons in data with the β quality requirement.

4.3 Muon Agnostic Analysis

In this section the MAg analysis [1], which is redone with the new β corrections explained in the previous section, is presented. The analysis uses data taken in 2012, whereby the data taking period A is excluded due to differences in the available triggers. The amount of statistics used is $\int Ldt \approx 18.8 \text{ fb}^{-1}$. First the event selection is discussed. The following part is about the candidate pre-selection, based on requirements on the track quality as well as requirements on the dE/dx and β measurement. The final selection cuts are discussed in the next part. A data driven background estimated has been chosen to accomplish good statistics in the tails of the β spectrum presented in the fourth section. This is followed by a description of the systematic uncertainties considered. Finally the results are presented and interpreted.

4.3.1 Event Selection

The requirements on events used for the analysis are shown in Tab 4.3 and will be discussed in the following.

Description	Requirement
Trigger selection	<i>EF_xe80_tclcw_loose</i>
Detector flags	GRL LAr veto
RPVLL preselection (MC)	$N_{trkpt5} > 0$ with: $p_T > 80 \text{ GeV}$ and $N_{SCT}^{Hits} > 5$ and $N_{Pix}^{Hits} > 1$

Table 4.3: The event selection for the MAg analysis.

Trigger selection: The trigger used for the analysis are the lowest unscaled \cancel{E}_T trigger chains available. The events have to be accepted by the *EF_xe80_tclcw_loose* trigger. \cancel{E}_T triggers can be used, as R -hadrons contribute to the \cancel{E}_T due to their moderate energy deposits. In principle no high \cancel{E}_T would be expected. But through the recoil from jets caused by Initial State Radiation, the R -hadron system can get a boost, resulting in larger \cancel{E}_T . As ISR does not occur in every event, the efficiencies of \cancel{E}_T triggers for the search for R -hadrons are not very high ($\sim 20\% - 25\%$). The MAg does not include informations from the muon spectrometer, therefore \cancel{E}_T triggers are the only triggers that can be used for this analysis.

Detector flags: The ATLAS detector is a very complex system. Therefore some of the subsystems can have defects. The ATLAS Data Quality team produces from all reported defects of the subsystems a Good Run List (GRL) that states for two minute intervals, if the detector delivered trustworthy data. To further ensure good running conditions of the detector the LAr veto is prompted. This rejects events where defects in the

LAr calorimeter appeared.

Preselection: The RPVLL JetTauEtmisss stream used for the data has a pre-selection. This has to be accomplished in MC. The selection criteria used for the RPVLL pre-selection are therefore applied to MC events as well. In the events, at least one ID track, with a $p_T > 80$ GeV, at least five hits in the SCT and at least one hit in the pixel detector, is required.

4.3.2 Candidate Pre-selection

The candidate pre-selection criteria are shown in Tab. 4.4 and will be explained in the following.

Description	Value
At least four tracks from any vertex	$N_{tracks}^{vertex} > 3$
Minimum transverse momentum	$p_T^{track} > 50.0$ GeV
Sensible momentum	0.0 TeV $< p^{track} < 4.0$ TeV
Isolation from high momentum jet	$\Delta R_{jet, p_T > 40.0 \text{ GeV}} > 0.3$
Isolation from high momentum track	$\Delta R_{track, p_T > 10.0 \text{ GeV}} > 0.25$
At least six SCT hits or passed dead sensors	$N_{SCT}^{hits} + N_{SCT}^{dead} > 5$
At least six TRT hits	$N_{TRT}^{hits} > 5$
Central longitudinal and radial vertex position	$ z_0 < 10.0$ mm, $ d_0 < 2.0$ mm
No shared pixel cluster	$N_{PIX}^{sharedhits} = 0$
At least two good pixel clusters	$N_{PIX}^{hits \text{ good } dE/dx} > 5$
Sensible pixel dE/dx	$0 \text{ MeVg}^{-1}\text{cm}^2 < dE/dx < 20 \text{ MeVg}^{-1}\text{cm}^2$
Sensible pixel $\beta\gamma$	$0.204 < \beta\gamma < 10$
Eta cut	$ \eta < 1.65$
Z veto	$ m(\text{cand}(m = m_\mu), \mu) - m_Z > 10$ GeV
Cosmic veto	$Q(\text{cand}) \cdot Q(\text{trk}) > 0$ & $ \eta(\text{cand}) + \eta(\text{trk}) > 0.005$ & $ \phi(\text{cand}) - \phi(\text{trk}) - \pi > 0.005$
Sensible TileCal β	$0.2 < \beta < 2$
Quality β	$\sigma_\beta < 0.12$

Table 4.4: The candidate pre-selection for the MAg analysis.

At least four tracks from any vertex: This ensures that no cosmic particles contaminate the events. The reason for that is, that cosmic particles reconstructed in the ID are two absolutely back-to-back tracks. For more than two associated tracks to the vertex additional cosmic particles would be needed to fake it.

Minimum transverse momentum: The minimum transverse momentum ensures a reasonable cutflow, but as in the final selection hard requirements on the momentum are applied, it has almost no influence on the selection.

Sensible momentum: For one particle produced at the LHC with $\sqrt{s} = 8$ TeV the absolute momentum for pair-produced particles is lim-

ited to 4 TeV according to energy and momentum conservation. Consequently the limit for a sensible momentum rejects mis-measurements of the detector.

Isolation from high momentum jet: To ensure that no particles from jets corrupt the time measurement in the TileCal an isolation between the candidate and any jet in the event with $p_T > 40.0$ GeV is required. For the separation in the $\eta - \phi$ -plane $\Delta R = \sqrt{\eta^2 + \phi^2}$ is used. It is necessary to claim isolation only from high momentum jets, as SMPs deposit smaller amounts of energy in the calorimeters and therefore may be reconstructed as low momentum jets.

Isolation from high momentum track: Comparable to the isolation from jets also an isolation from other high momentum tracks is required.

At least six SCT hits or dead sensors passed: The requirements on the minimum SCT hits ensures a good track quality.

At least six TRT hits: Also the TRT hits requirement is used to achieve a good track quality.

Central longitudinal and radial vertex position: Due to the high momenta of the SMPs they are expected to originate almost in any case from the Primary Vertex PV. The requirements on the longitudinal z_0 and the transverse impact parameter d_0 ensure that the candidates come from the primary vertex and therefore have a well determined origin. It further ensures that the candidate origins from a primary particle.

No shared pixel cluster: Further particles could also deposit charge in the candidate pixel cluster. To prevent this corruption, no shared pixel clusters are allowed for candidates.

At least two good pixel clusters As the main background for the search for SMPs are mis-measurements in the detector, and fluctuations are more probable for one measurement as for more measurements simultaneously, at least two good pixel clusters for each candidate track are required.

Sensible pixel dE/dx: For the dE/dx measurement candidates with an unexpected high energy loss as well as with a unphysical energy gain are rejected.

Sensible pixel $\beta\gamma$: An upper limit of the $\beta\gamma$ range is used to reduce the muon background, whereas the lower limit is used to suppressed mis-measurements in the detector, as SMPs with the considered masses are not expected to have $\beta\gamma < 0.2$. A further reason for the lower limit is the readout window of the TileCal cells, since candidates with lower velocities are expected to exceed the readout window of 75 ns. As for this case the β measurement in the TileCal is corrupted, the pixel $\beta\gamma$ can be used to reject candidates with lower velocities.

Eta cut: The TileCal covers the range of $\sim \eta < 1.7$, but as for the highest η region only one cell is hit, the upper limit for η is set to 1.65. Also a wider range could be considered, but due to the different detector systems in the end-caps and the worse β resolution only the TileCal

region is used.

Z veto: High momentum muons produced at the LHC predominantly originate from Z -bosons, the candidates are rejected, if the invariant mass of the candidate and the hardest muon is within a 10 GeV mass window of the Z -boson mass. For candidates the muon mass is assumed for the calculation of the invariant mass. If the track of the candidate can be matched to the hardest muon, the second hardest muon is used. The ID track and muon track are matched if $\Delta R_{Track,\mu} < 0.1$.

Cosmic veto: Candidates are rejected with signatures compatible with cosmic particles in the detector. The signatures of a cosmic particle are two back-to-back tracks. As a cosmic particle would travel one of the tracks revers in the frame of the detector, the bend of the tracks in the magnetic fields is in opposite direction. This means, that cosmic particle associated tracks would have different reconstructed charges. Consequently candidates having a back-to-back track with different estimated charge are rejected.

Sensible TileCal β : As previously mentioned, candidates with $\beta < 0.2$ exceed the readout window of the TileCal t_{cell} measurement. Therefore a lower β limit is set. An upper limit suppresses muon background.

β Quality: If the uncertainty on the β measurement is too large, the estimated β is not trustworthy. Hence candidates with an uncertainty $\sigma_\beta > 0.12$ are rejected.

Consistency β : In the nominal analysis a further selection criterion was applied, the β -consistency check. The β consistency check requires the probability of χ_β^2 for N Degrees of Freedom (NDF) to be larger than 0.001. $P(\chi_\beta^2, NDF)$ is the nearer to zero, the more inconsistent the measurements. χ_β^2 can be calculated with

$$\chi^2 = \sum_i \frac{(\beta^{-1} - \beta_i^{-1})}{\sigma_{\beta_i^{-1}}^2}. \quad (4.22)$$

NDF is given by the number of β measurements as $NDF = N_\beta - 1$, where N_β states the number of β measurements. I decided to drop the β consistency check. It does not ensure that the β is measured correctly only that the agreement between the single measurements is sensible within their uncertainties. It has further more or less similar efficiencies in data and signal and therefore mainly reduces the statistics. The high-mass R -hadron signal regions have only very little statistics and as the improved β estimation reduces the background further, it makes sense to not apply the β consistency check.

In R -parity conserving models, R -hadrons are always produced in pairs. Nevertheless in only 10% of the events both R -hadrons are reconstructed as candidates. The reason for that is, that $\sim 50\%$ of sparticles hadronize to uncharged R -hadrons. Also the candidate pre-selection rejects $\sim 40\%$ of the candidates leading to the low number of events ex-

pected with two R -hadrons reconstructed as candidates. As the theoretical production cross section is per event, for the case of more candidates per event, one of the R -hadron candidates is randomly selected and rejected. It would be also possible to use a two candidate signal region, but this only reduces the background. As this analysis has anyway almost no background a two candidate region is not used.

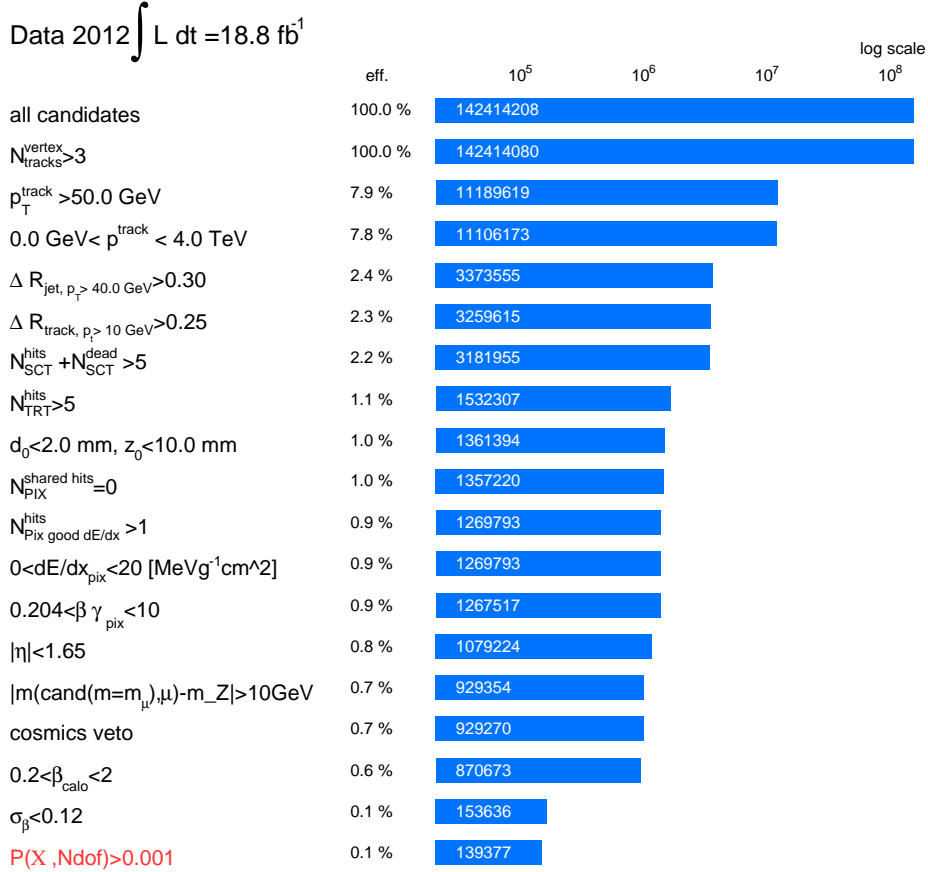


Figure 4.37: Cutflow for data candidates. In red the β -consistency check which is not applied in the analysis

The cutflows for data candidates and weighted candidates from a 1300 GeV gluino R -hadron signal sample are shown in Fig. 4.37 and Fig. 4.38, respectively.

4.3.3 Final Selection

For the final selection, which is specific for each signal masspoint, momentum, β , $\beta\gamma$, m_{β} and $m_{\beta\gamma}$ are used as discriminators. For the optimization the data driven background estimate described in the following section and the signal samples are used.

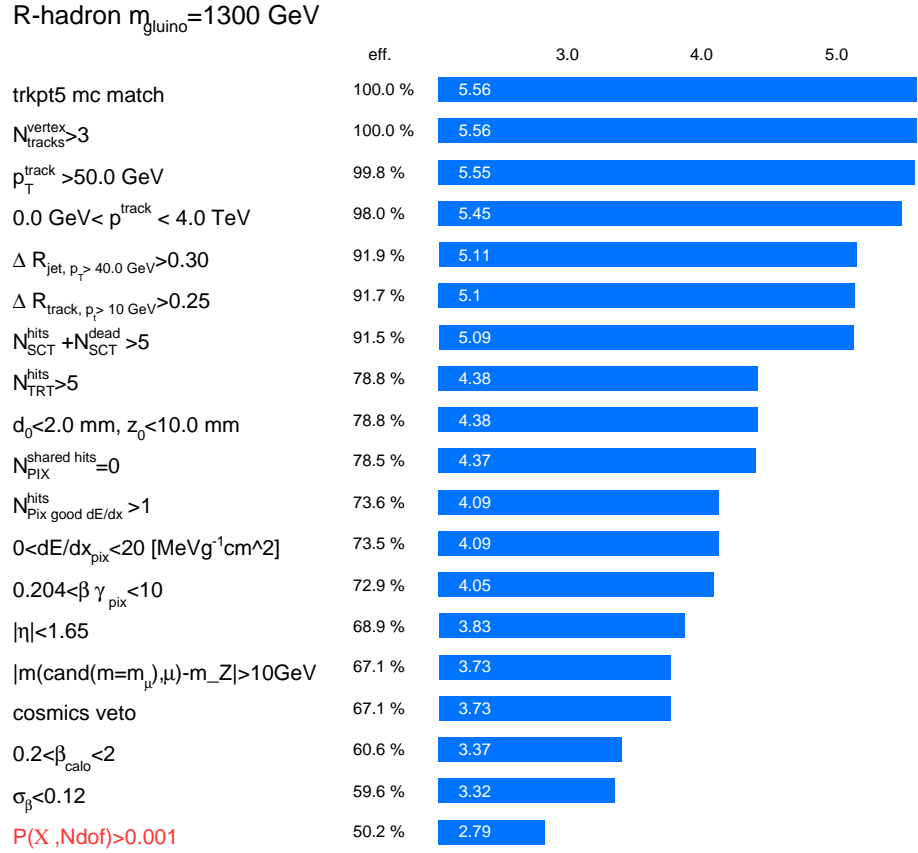


Figure 4.38: Cutflow for candidates for gluino R -hadron 1300 GeV hypothesis. In red the β -consistency check which is not applied in the analysis.

Momentum

As no corrections are applied on the momentum the requirements for the different \tilde{g} , \tilde{b} and \tilde{t} masspoints from the nominal analysis are used unchanged for this analysis.

β and $\beta\gamma$

For the β and $\beta\gamma$ selection criteria an optimization has to be applied to accomplish the best available signal purity in the signal region. To evaluate the signal purity two different measures were considered

$$P_1 = \frac{S}{\sqrt{B}} \quad (4.23)$$

and

$$P_2 = \frac{S}{\sqrt{B+S}}. \quad (4.24)$$

For the significance problems arise if the number of background events is almost zero. This is the case for the high mass signal regions. Hence

as measure for the purity Eq. 4.24 is used.

For the optimization of the β and $\beta\gamma$ requirements the cuts applied in the nominal analysis are used as starting point. They are varied until the best purity in the signal region is achieved.

m_β and $m_{\beta\gamma}$

The very final cuts are on the mass estimates. The method is the same as in the nominal analysis. The cuts are set according to the peak and the width of the expected signal mass distributions. The estimated masses have to be higher than the peak minus two times the width σ of the respective mass distribution. The final mass cuts for a 1300 GeV gluino R -hadron hypothesis are shown in Fig. 4.39.

The search is divided into a final selection optimized for gluinos and a final selection optimized for sbottom/stop, as the lower cross section of the sbottom/stop case requires harder cuts.

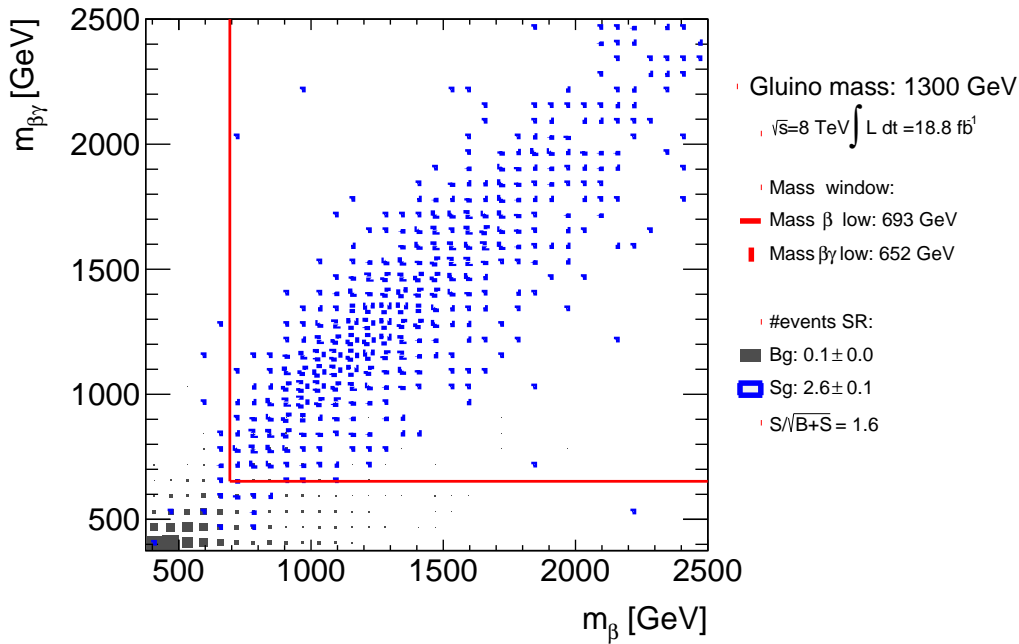


Figure 4.39: Signal and background candidate masses in the m_β - $m_{\beta\gamma}$ -plane.

4.3.4 Background Estimation

The main backgrounds for the MAg search are high momentum muons which have mis-measured β and $\beta\gamma$ values. Also non-collision backgrounds may fake SMPs in the detector as for example electronic noise or cosmic particles. The non-collision background should be heavily suppressed by the candidate pre-selection. The remaining non-collision back-

grounds are negligible and included in the data-driven background estimate.

On the one hand the data-driven background estimate is used, because especially in the low- β tail high statistics are needed, which would require enormous amounts of MC. On the other hand the data driven method does not rely on the modeling of the readout, which is shown to be not perfect. The method is the same as used in the nominal analysis.

The final selection is on the estimated masses m_β and $m_{\beta\gamma}$. β , $\beta\gamma$ and p are uncorrelated, as the main background are mis-measurements of energy loss and t_{cell} , which are measured in different detector subsystems. Probability density functions are produced from data for β , $\beta\gamma$ and p . The PDFs are produced from all candidates passing the pre-selection. To compensate a small correlation due to their dependence on η the PDFs are produced in five η bins. For the β and $\beta\gamma$ PDFs a momentum between 70 GeV and 180 GeV is required and the final selection cuts on β and $\beta\gamma$ respectively are applied. Consequently different PDFs are produced for each mass hypothesis. For the momentum PDF the final momentum cuts are applied. The candidates further have to fulfill $\beta < 0.90$ and $\beta\gamma < 2.5$. The PDFs of β and $\beta\gamma$ for a gluino ($m_{\tilde{g}} = 500$ GeV) in the η region $0.99 < \eta < 1,32$ are shown in Fig. 4.40.

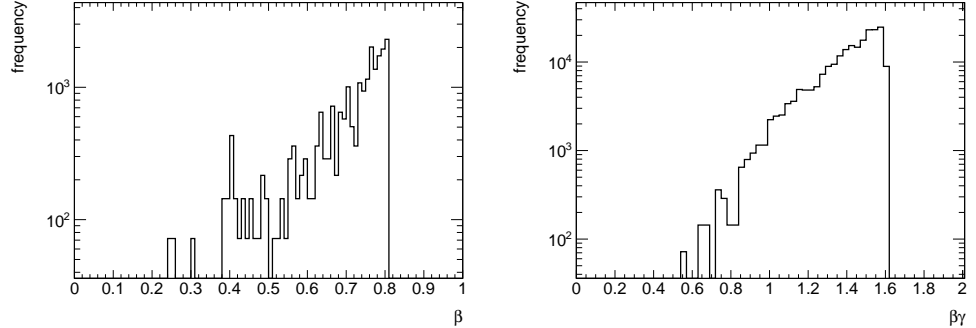


Figure 4.40: PDF for the β and $\beta\gamma$ in the η region $0.99 < \eta < 1.32$.

From the 2D-PDF of the momentum as a function of η a (p, η) pair is sampled. The according $PDFs(\eta, \beta/\beta\gamma)$ are used to sample values for β and $\beta\gamma$. From p and $\beta/\beta\gamma$ the masses m_β and $m_{\beta\gamma}$ are calculated. This is done 2500 times for each candidate passing the selection. Consequently, a weight of $1/2500$ is used for the background events.

The resulting background distribution, with the superimposed MC and data distributions in the m_β - $m_{\beta\gamma}$ -plane for a 500 GeV gluino mass hypothesis, is shown in Fig. 4.41 for m_β and in Fig. 4.42 for $m_{\beta\gamma}$. It can be seen, that the agreement between data and background is reasonable.

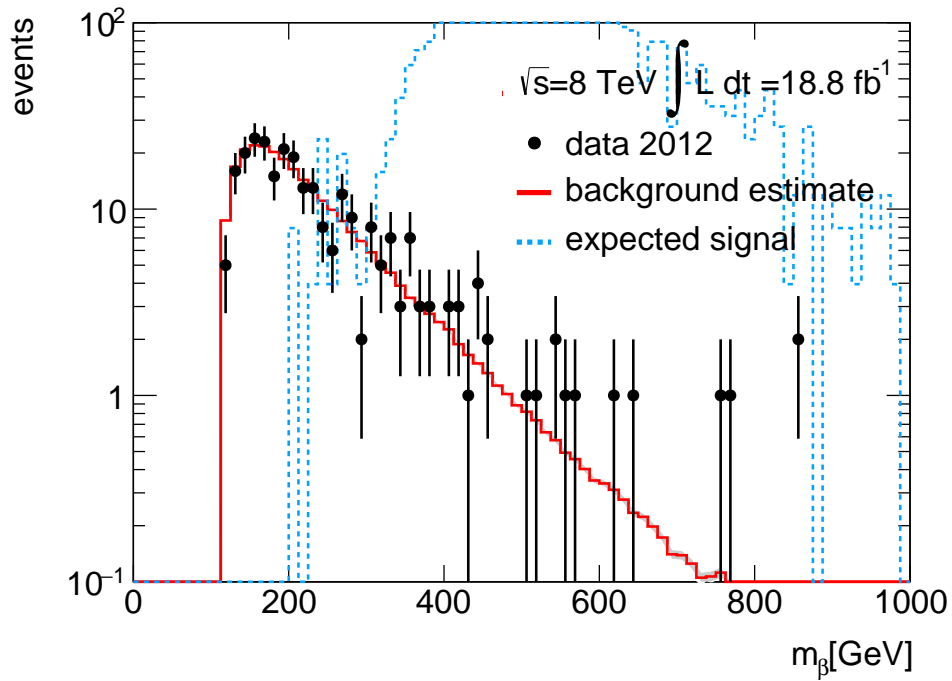


Figure 4.41: $m_{\beta\gamma}$ distribution in data, background and signal for a 500 GeV gluino R -hadron mass hypothesis.

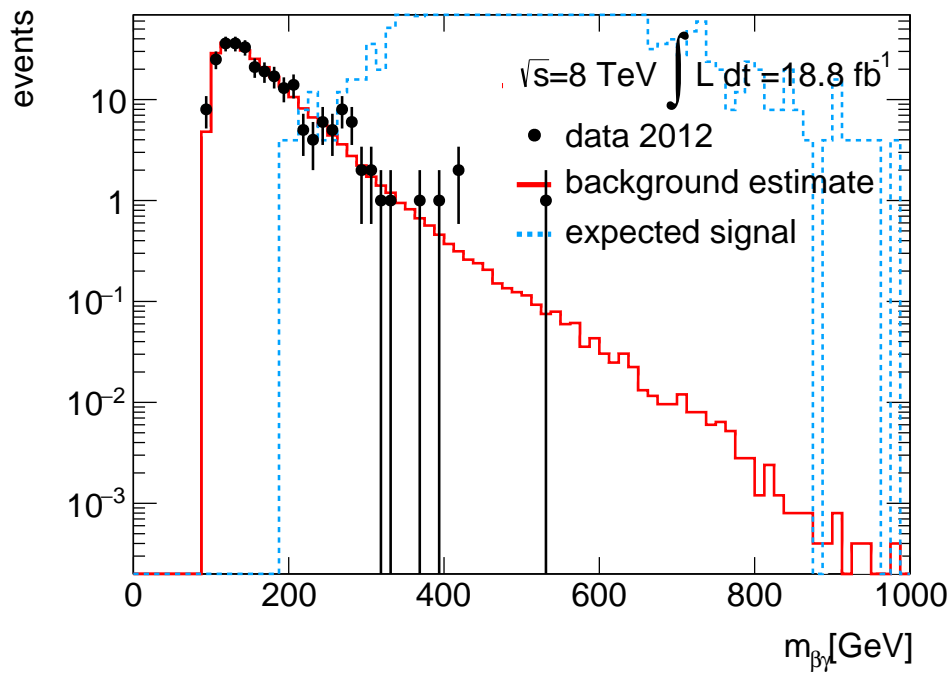


Figure 4.42: $m_{\beta\gamma}$ distribution of data, background and signal for a 500 GeV gluino R -hadron mass hypothesis.

4.3.5 Systematic Uncertainties

Several sources of systematic uncertainties have to be considered for the MAg analysis. Some of the uncertainties estimated for the nominal analysis have not changed or did not change significantly. These uncertainties are therefore taken over for this analysis. The systematic uncertainties taken from the nominal analysis are thus for the theoretical cross section, the trigger efficiency, the ISR, the pixel dE/dx calibration and the the luminosity of the data samples. The uncertainties that are estimated new for this analysis are those for the β calibration and for the background estimate.

Uncertainty on the Theoretical Cross Section

The theoretical cross section and the uncertainty are obtained from a set of different cross section predictions using different PDFs, factorization and renormalization scales following Ref. [23]. The resulting uncertainties are 15% for gluinos with $m = 100$ GeV and go up to 52% for $m = 1700$ GeV gluinos.

Uncertainty on Trigger Efficiency

For the uncertainty on the trigger efficiency the turn-on curve of the each used trigger was parametrized with Eq. 4.25 for $Z \rightarrow \mu\mu$ events in data and MC.

$$\varepsilon(\cancel{E}_T) = \frac{A}{2} \left[1 + \operatorname{erf} \left(\frac{\cancel{E}_T - B}{\sqrt{2}C} \right) \right] \quad (4.25)$$

$Z \rightarrow \mu\mu$ events are used as they are similar to R -hadrons as muons are not included in the \cancel{E}_T calculation on trigger level. Furthermore muons from $Z \rightarrow \mu\mu$ can be easily identified in data. The uncertainty is calculated from the differences in the efficiency seen in data and MC and from the 1σ up and down variation of the parameters B and C. The resulting uncertainty on the signal trigger efficiency is less than 3.9 % conservatively used for all mass and sparticle hypotheses.

ISR Uncertainty

R -hadron events are accepted by the \cancel{E}_T triggers mostly due to ISR. Variations in the modeling of the ISR radiation are therefore critical for the signal efficiency and have to be taken into account as a systematic uncertainty. The ISR level in the generator (PYTHIA6) is scaled up and down. The resulting uncertainty on the signal efficiency is 9.6% conservatively used for all mass and sparticle hypotheses.

Uncertainty on Pixel dE/dx

The difference between dE/dx of the MC and data R -hadron candidates are considered as systematic uncertainty. Furthermore the variation of the proton mass over time and the offset of the average proton mass are taken into account. The uncertainty on the signal efficiency for the pixel dE/dx is 1.1%.

Luminosity

The uncertainty on the luminosity of the used data sample is 2.8 % [39].

Uncertainty on Calorimeter-Time Smearing

The uncertainty on the signal efficiency due to the t_{cell} smearing is estimated by scaling the smearing 5% up and down. The influence of this variation on the β distribution for $Z \rightarrow \mu\mu$ muons in MC compared with the distribution obtained from data is shown in Fig. 4.43. This variation

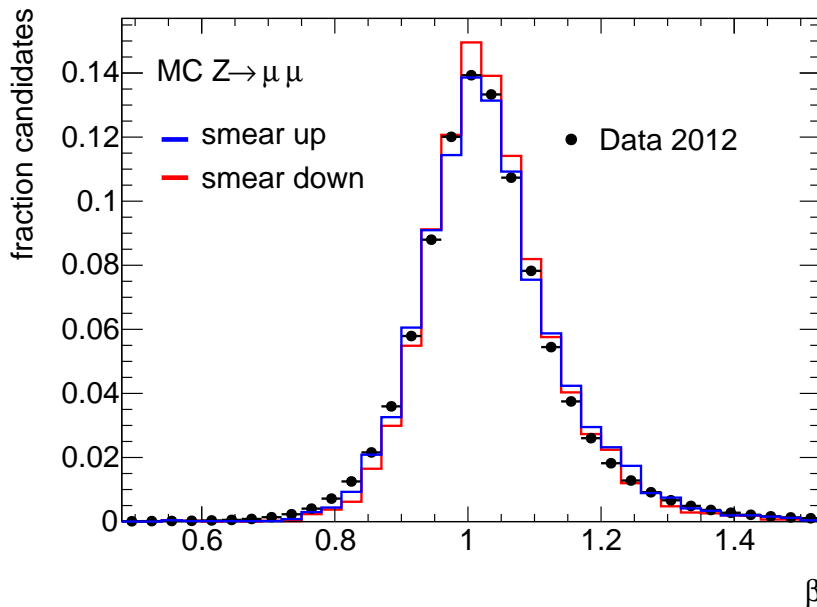


Figure 4.43: β distribution for $Z \rightarrow \mu\mu$ muons for smearing scaled up and down MC and for data.

is then applied to the signal samples and the RMS between the scaled up, scaled down and nominal signal efficiency is used as uncertainty. The maximum variation is found to be 1.4% and used for all signal points as a conservative estimation.

Background uncertainty

For the uncertainty on the background estimate a tight and a loose selection for producing the PDFs is applied, as shown in Tab. 4.5.

Table 4.5: Tight loose and baseline selection for the production of the PDFs.

Selection	p PDF	β and $\beta\gamma$ PDF
Baseline	$\beta < 0.90$ and $\beta\gamma < 2.5$	$70 \text{ GeV} < p < 180 \text{ GeV}$
Tight	$\beta < 0.88$ and $\beta\gamma < 2.4$	$80 \text{ GeV} < p < 150 \text{ GeV}$
Loose	$\beta < 0.92$ and $\beta\gamma < 2.6$	$60 \text{ GeV} < p < 200 \text{ GeV}$

Again the RMS between the background efficiencies obtained for the the different selections is used as systematic uncertainty. As for higher masses, the background estimate in the signal region relies more on the tails of the PDFs, it is expected, that the systematic uncertainty increases with mass. This is shown in Fig. 4.44. As the uncertainty grows more or

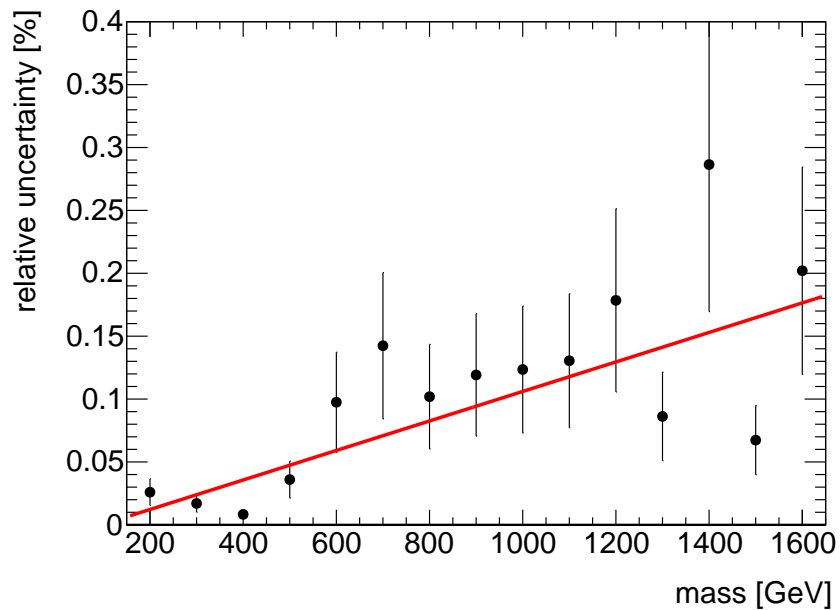


Figure 4.44: Systematic uncertainty on the background as a function of the mass for the gluino optimized search.

less linear with mass a linear fit to the uncertainty as a function of mass is used to estimate the systematic uncertainty on the background. This is done for the sbottom/stop optimized search and the gluino optimized search separately. A summary of all considered systematic uncertainties is given in Tab. 4.6.

Source	Systematic uncertainty [%]
Theoretical cross section	15–52
Trigger efficiency	3.9
ISR	9
Pixel dE/dx	1.1
Calorimeter time smearing	1.4
Luminosity	2.8
Background estimate	3.0–17.6

Table 4.6: Summary of considered systematic uncertainties.

4.3.6 Results and Interpretation

An experimental evidence for new particles would be a significant excess of observed data over the expected background. The distributions for background, expected signal and data in the m_β - $m_{\beta\gamma}$ plane for the gluino $m_{\tilde{g}}=1300$ GeV, the sbottom $m_{\tilde{b}}=800$ GeV and the stop $m_{\tilde{t}}=800$ GeV R -hadron hypothesis are shown in Figs. 4.45, 4.46 and 4.47, respectively. No excess over the expected background was observed for all signal regions optimized for the different mass hypotheses.

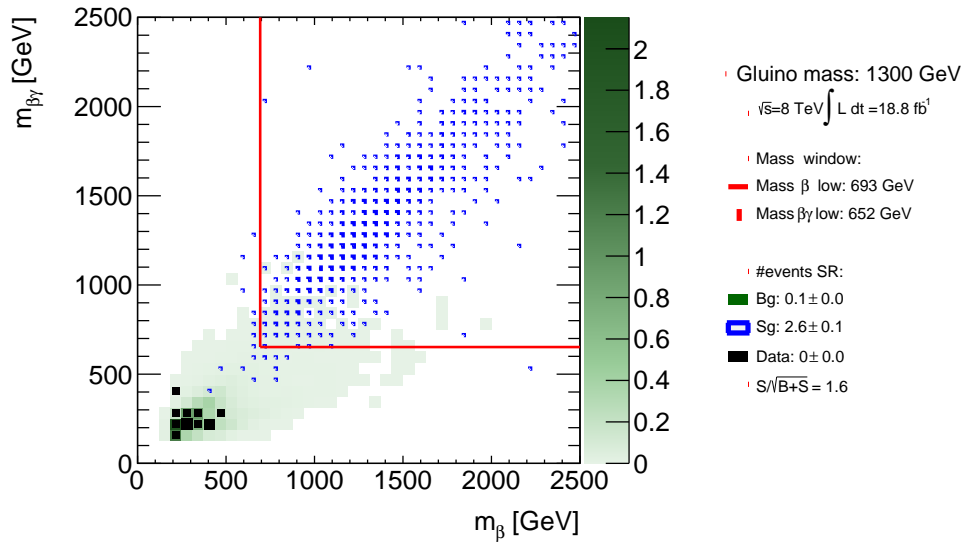


Figure 4.45: Estimated background, data and expected signal distribution in the m_β - $m_{\beta\gamma}$ -plane for a 1300 GeV gluino hypothesis.

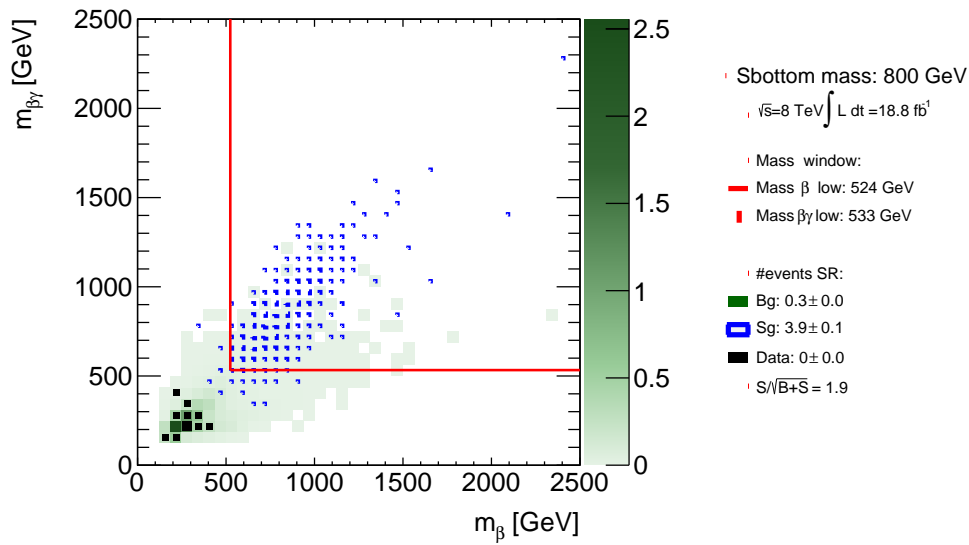


Figure 4.46: Estimated background, data and expected signal distribution in the m_β - $m_{\beta\gamma}$ -plane for an 800 GeV sbottom hypothesis.

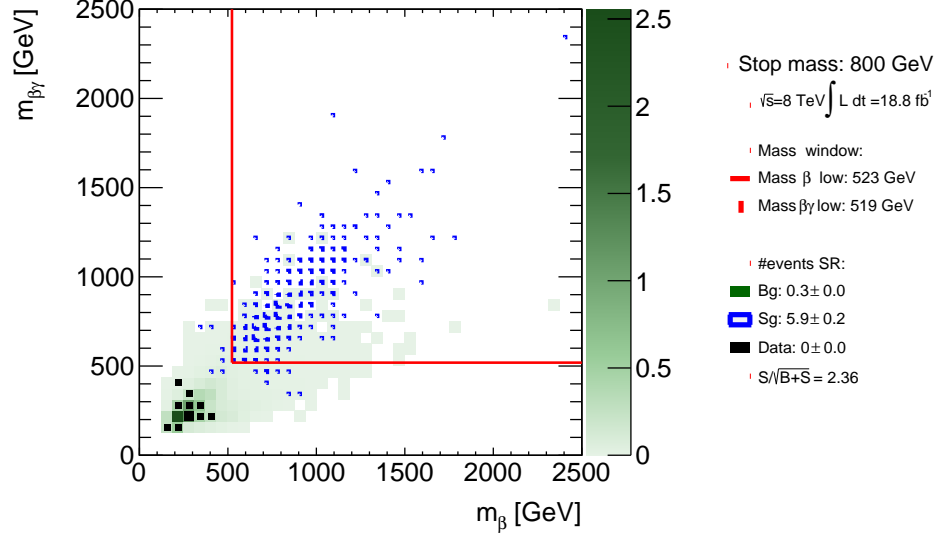


Figure 4.47: Estimated background, data and expected signal distribution in the m_β - $m_{\beta\gamma}$ -plane for a 800 GeV stop hypothesis.

As no evidence for new particles was observed, the results can be used to set cross section limits for the different hypotheses.

The upper limits on the cross sections are calculated using the HistFitter package [40] by simple counting of background, signal and data events in the signal region. The limit setting is based on a frequentist analysis using a likelihood ratio as test statistic. First a likelihood probability density function for the expectations has to be constructed. A Poisson counting model is assumed for the number of observed events N_{obs} . The systematic uncertainties are taken into account as nuisance parameters θ and are assumed to be Gaussian distributed. The likelihood ratio is given by

$$Q = -2 \ln \left(\frac{L(\mu, \hat{\theta})}{L(\hat{\mu}, \hat{\theta})} \right), \quad (4.26)$$

with the signal strength μ , a scaling factor for the number of expected signal events s . $\hat{\theta}$ is the value of θ , which maximizes L for a specific μ , called the conditional maximum-likelihood estimation. $\hat{\theta}$ and $\hat{\mu}$ are the parameters for which the unconditional likelihood maximizes. Hence the numerator is always smaller or equal to the denominator. This means, that the ratio is between one and zero, with a ratio near one stating a good agreement between the model and the hypothesis. The CL_{s+b} is given by

$$CL_{s+b} = 1 - p_{s+b}(Q \geq Q_{obs}) = 1 - \int_{Q_{obs}}^{\infty} f(Q|\mu) dQ, \quad (4.27)$$

with p being the p-value, Q_{obs} being the value of the test statistic observed in the experiment and f being the probability density function. The CL_{s+b}

is the probability to get a value of the likelihood ratio, which is equal or higher than Q_{obs} . This integral can be solved with the asymptotic formula described in Ref. [41]. To be less affected by fluctuations of the background CL_s is used for the limit setting, which is given by

$$CL_s = \frac{CL_{s+b}}{CL_b}, \quad (4.28)$$

with CL_b , being the confidence level under the background only hypothesis. In particle physics it is convenient to use a CL of 95% for the exclusion of a signal. This means that a fluctuation to equal or more than s+b events is less than 5%. By increasing or decreasing the signal strength the value of μ can be obtained for which the CL_s is 5%. This is illustrated in Fig. 4.48. The limit on the signal strength can be converted

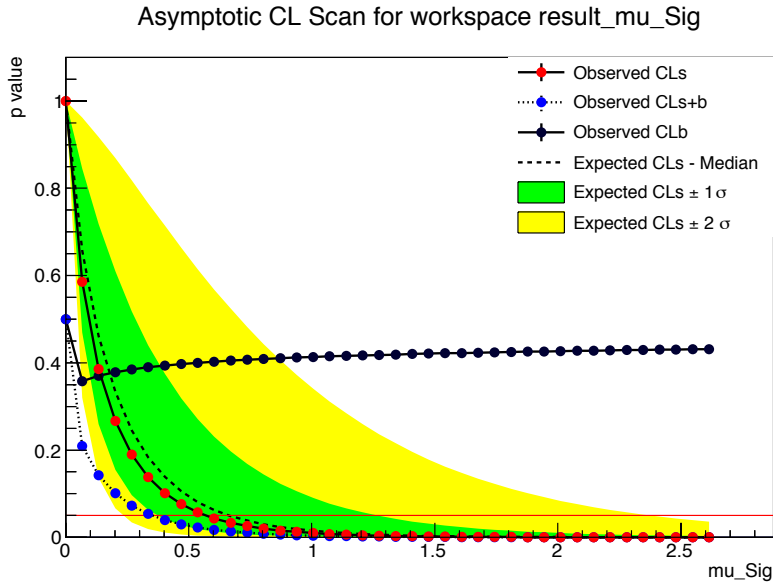


Figure 4.48: P-value as function of the signal strength for CL_{s+b} , CL_s and CL_b in the sbottom 800 GeV signal region.

into an upper limit on the cross section using

$$\sigma_{Lim} = \frac{\mu S}{\varepsilon_s \int L dt}, \quad (4.29)$$

with ε_s , the signal efficiency. The signal efficiency is estimated as the ratio of events with a candidate in the signal region divided by the number of events in the signal sample.

The resulting limits for the gluino, sbottom and stop models are shown

in Fig. 4.49, Fig. 4.50 and Fig. 4.51, respectively. With this search for R -hadrons a lower mass limit at 95% CL is obtained for gluinos at 1241 GeV, for sbottoms at 760 GeV and for stops at 800 GeV. The limits from the nominal MAg search are 1262 GeV for gluinos, 758 GeV for sbottoms and 868 GeV for stops. The limits obtained in this analysis are worse for the stop/gluino models, but slightly improve the limit on the sbottom mass. The limit on the gluino mass is higher than the limit on the squark masses due to the higher cross section. Sbottom and stop have the same cross section. The difference between the sbottom and stop limits arises as sbottoms hadronize to neutral states more often than stops. The lower limits for gluino/stop compared to the nominal analysis are understandable, as less statistics are used. This analysis does not include period A of the data taking and is therefore only based on an integrated luminosity of 18.8 fb^{-1} instead of 19.1 fb^{-1} . Besides the RPVLLJetTauEtmisstream the nominal analysis also used the HadDelayed stream, which has a 20 GeV lower unrescaled \cancel{E}_T trigger. For R -hadrons not in each event large \cancel{E}_T is expected, as it relies on ISR. Hence a lower \cancel{E}_T trigger threshold improves the statistics significantly. For example for gluino R -hadrons with $m_{\tilde{g}} = 1300 \text{ GeV}$, 23% more candidates are left after the event selection. This is predominantly because of the lower \cancel{E}_T trigger threshold. The limits on the stop and gluino masses are mostly dominated by the low statistics. They are located in the high mass region where almost no background is left. Therefore no improved mass limits are expected. The sbottom limit is at lower masses, where the background plays a more important role. With the discussed improvements of the β estimate and the according suppression of the background, more or less the same limit on the sbottom mass could be obtained with significantly less statistics ($\mathcal{O}(25\%)$).

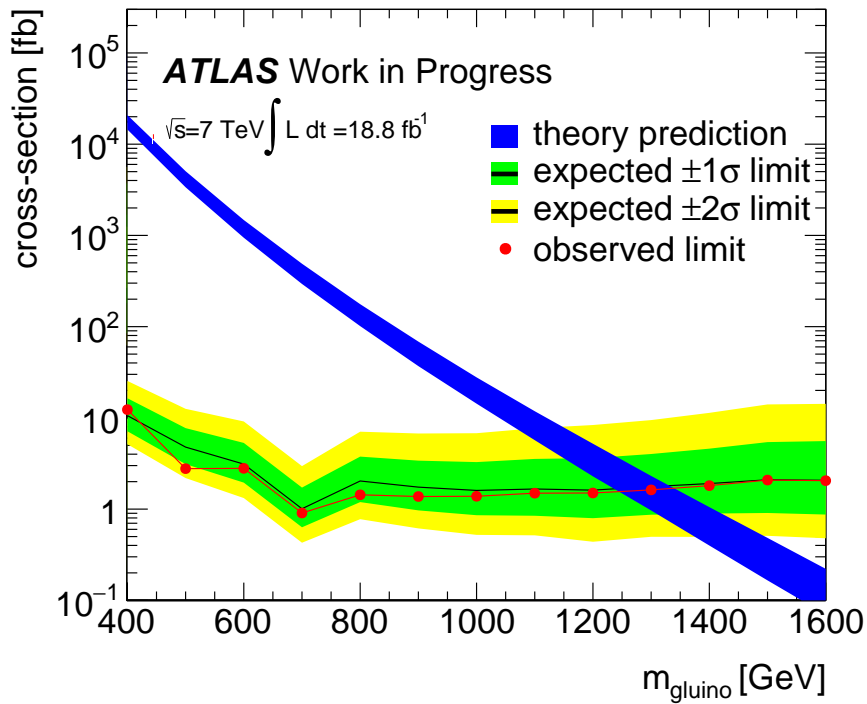


Figure 4.49: Limits on the cross section for the different gluino mass hypotheses as well as theoretical cross section.

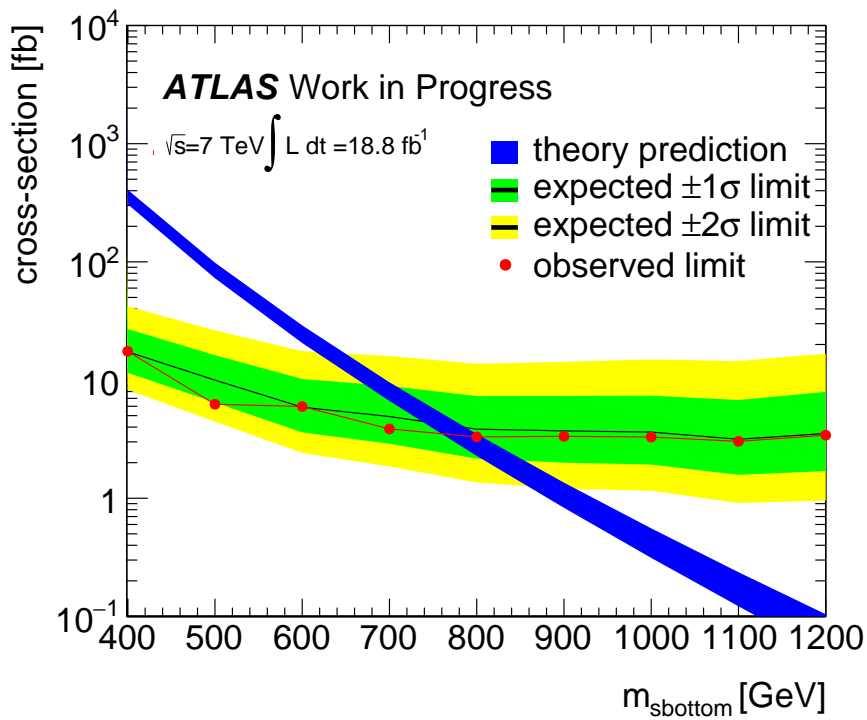


Figure 4.50: Limits on the cross section for the different sbottom mass hypotheses as well as theoretical cross section.

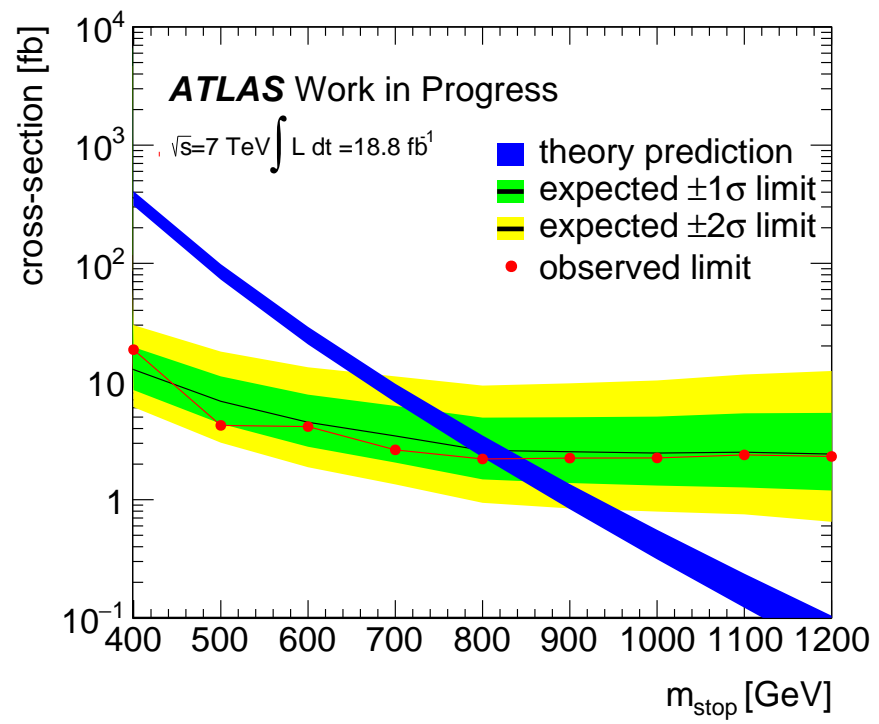


Figure 4.51: Limits on the cross section for the different stop mass hypotheses as well as theoretical cross section.

Chapter 5

Conclusion and Outlook

5.1 Conclusion

Studies on the β estimation with the ATLAS calorimeters were performed. The time correction for the bias seen at high t_{cell} is able to improve the β resolution especially for R -hadrons. In data the DistCor is able to correct the bias of β as a function of η in each cell, whereas the linear correction overcompensates the bias. This is in conflict with the studies performed in MC, which therefore seems to have incorrectly modeled t_{cell} . The DistCor is further used to correct t_{cell} to be measured at the same distance of the particles from the IP. This is used to obtain a more reasonable smearing of t_{cell} in MC, which is necessary to have a good agreement between MC and data. Including the distance z_0 of the particle track to the IP in the DistCor slightly improves the β -resolution. The influence of the correction of t_{cell} on $\sigma_{t_{cell}}$ as a function of the energy deposit in the cell is shown to have a more than 5% lower $\sigma_{t_{cell}}$ for high energy deposits. The influence of the new parametrization of $\sigma_{t_{cell}}$ as a function of the energy deposit is found to be negligible for the β estimation. The energy-layer time calibration used in the nominal analysis does not have to be applied as this is corrected by the DistCor. This is an important improvement as it makes the analysis simpler and faster. In the runwise time calibration due to mis-alignment of the ATLAS clock with respect to the LHC clock, a fit with a Gaussian function of the t_{cell} distributions is shown to be less influenced by asymmetries in the tails. With this method no bias of t_{cell} is introduced through the calibration. Furthermore including the LAr calorimeter in the β estimation was evaluated, but was, as the resulting β distribution has more outliers, not included in the final β estimate. The overall improvement of the β -resolution compared to the nominal analysis is 17%.

The influence on the search for SMPs was tested by redoing the MAG search with the improved β estimate. The considered R -hadron sparticles are gluinos, sbottoms and stops, whereby different mass hypotheses were

tested (100 GeV–1600 GeV for gluinos and 100 GeV–1200 GeV for sbottoms/stops). No excess over the expected background for all signal regions was observed. The results are used to set upper limits on the cross section of the sparticles considered. Comparing these with the theoretically predicted cross sections lower limits on the particle masses can be estimated. The obtained mass limits are 1241 GeV for gluinos, 800 GeV for stops and 760 GeV for sbottoms. Compared with the nominal analysis, the limits for the gluino/stop mass are worse, whereas the limit on the sbottom mass slightly improves the published limit. As for this analysis only a 20 GeV higher \cancel{E}_T trigger threshold was available, significantly less statistics in the signal regions is obtained. Therefore the results are promising and justify, that the improved β estimation is a useful improvement for the search for SMPs.

5.2 Outlook

Further ideas for improving the β estimation and the search for R -hadrons came into my mind, which might be interesting for future studies. One essential part would be to investigate in the modeling of R -hadrons in the TileCal. Therefore dedicated studies on the interaction of one particle with the detector might be helpful. Furthermore the behavior of $\sigma_{t_{cell}}$ for low energy deposits should be investigated. It might be useful to introduce a further term in the parametrization of t_{cell} as function of the energy deposit describing the behavior in the low energy deposit region. A very powerful variable for the suppression of the background for the search for R -hadrons might be the dE/dx estimated with the TileCal. As R -hadrons are expected to have a significantly higher energy loss they would deposit, because of the long track in the TileCal, much more energy as muons. The resolution of the dE/dx measurement with the TileCal is not sufficient for a reasonable mass reconstruction, but using dE/dx as selection requirement might be quite powerful to suppress the expected background.

List of Figures

2.1	The extrapolation of the coupling constants to the scale of GUT for the energy transfer in an interaction. It can be seen that the different couplings do not intersect in one point.	5
2.2	First order quantum loop correction Feynman diagram of a virtual fermion f to the Higgs boson H	6
2.3	Particle content of the Minimal Supersymmetric Standard Model (MSSM).	7
2.4	Loop corrections to the Higgs mass from a fermion (a) and a boson (b).	8
2.5	Feynman diagram for a toy theory decay of a particle A into the particle B , C and D over a virtual heavy intermediate particle I^*	11
2.6	Feynman diagram of the decay of a muon into an electron over a virtual W^* boson.	12
2.7	Feynman diagram of a β decay of a neutron.	13
2.8	Qualitative mass spectrum of a Split-Supersymmetry scenario. The mass of the gluino is in the low mass region, whereas the squarks are in the high mass region.	14
3.1	The parton distributions for the LHC [17].	16
3.2	The integrated luminosity delivered by the LHC as well as the taken data and the data good for physics from the ATLAS experiment are shown against the date in 2012 Ref. [20].	17
3.3	The ATLAS detector with labeled subsystems, taken from Ref. [22]. The ATLAS detector is the largest general-purpose particle detector built so far with a length of 44 m and a height of 25 m	18
3.4	The coordinate system for the ATLAS detector with the nominal Interaction Point (IP) and the Beam Pipe (BP).	18
3.5	Examples for Feynman graphs of the leading production processes for LLPs. The processes shown are pair production of squarks (left), gluinos (middle) and sleptons (right) via $q\bar{q}$ -annihilation. Also gg -fusion or qg -annihilation are possible.	21

3.6	The left diagram shows the Rhadron kinetic energy (E_{kin}) spectrum for different gluino mass points. The momentum distributions for different gluino mass points are shown in the right diagram.	21
3.7	Momentum as a function of the rest mass for $E_{kin} = 100$ GeV.	22
3.8	The β distributions for $\tilde{\tau}$ particles, \tilde{g} Rhadrons and muons.	22
3.9	The signatures of SM particles in the detector. Quarks hadronize due to the quark confinement leading to jet objects in the detector. Dashed lines indicate particles which are not detectable.	24
3.10	Signatures of LLPs in the detector. Most of the mentioned scenarios also provide slightly different signatures due to different finale state particles. For this cases one specific is displayed, whereas the others are mentioned in the text. Dashed lines indicate particles which are not detectable.	25
3.11	The energy loss reconstructed with the pixel detector for tracks as a function of momentum times charge (left). The most probable value distributions of pions (solid), kaons (dashed) and protons (dotted) are superimposed. The expected distributions for Rhadrons with several \tilde{g} masses are shown in the right diagram [1].	28
3.12	The cluster dE/dx measurements for 2010 Data and Monte Carlo [31].	29
3.13	Design of a ATLAS Tile Calorimeter module [22].	31
3.14	Layout of the TileCal cells and their labeling. The design of the cells in negative z -direction is symmetric.	31
3.15	The TileCal signal pulse with the seven samplings (dots) [32].	32
3.16	The number of passed TileCal cells for muons.	33
3.17	Functional parametrization of $\sigma_{t_{cell}}(E)$ for muons.	33
4.1	t_{cell} distributions for muons from $Z \rightarrow \mu\mu$ MC and data	39
4.2	Uncertainty on t_{cell} in each cell for MC muons. The labeling of the cells is according to the names in Fig. 3.14.	39
4.3	Uncertainty on t_{cell} in each cell for data muons. The labeling of the cells is according to the names in Fig. 3.14.	40
4.4	The t_{cell} distributions for data and smeared MC for all measurements.	41
4.5	$\Delta\beta/\beta$ as function of the cell time. For low cell times the estimated β is reasonable and has only some fluctuations due to pile-up. Whereas for higher cell times the estimated β is too low.	42
4.6	$\beta_{est} - \beta_{truth}$ as function of the cell time with the points of the gaussian fits (left). The Gaussian fit of one slice in t_{cell} (right).	43
4.7	$\Delta\beta/\beta$ as function of the cell time for the time corrected β	44
4.8	β resolution for Rhadron candidates with and without time correction.	44

4.9	β distribution for muon candidates from $Z \rightarrow \mu\mu$ in MC and data with and without the time correction. The β distribution looks basically the same as the β -resolution distribution for muons as they are expected to have $\beta_{truth} = 1$	44
4.10	The β -resolution as a function of η for the cells of the D layer.	45
4.11	The reconstructed position d_{trk} of the time measurement for a particle following the green track. The blue dashed line refers to a particle traveling with the speed-of-light traversing the cell center.	46
4.12	The shape of a cell of sampling scheme 13 (see Fig. 3.14) with a particle track traversing the cell. All important positions on the track for the estimation of d_{new} are labeled.	47
4.13	The pulse shape obtained with Eureka (red) and the Gaussian (blue) in the left figure. The difference between the shape from Eureka and the Gaussian in the right figure.	47
4.14	The TileCal cells in z - r -plane in black and in blue d_{new} in the direction of the trajectory of the particle.	49
4.15	The TileCal cells in z - r -plane in black and in red the distance of the IP to the cell center in direction of the trajectory of the particle.	49
4.16	Difference between d_{center} and d_{new} as a function of η for cell D5.	49
4.17	Distribution of the uncorrected $\Delta\beta/\beta$ as function of η for cell D6 in MC.	50
4.18	Distribution of $\Delta\beta/\beta$ with the distance correction (left) and the linear correction (right) as function of η for cell D6 in MC.	50
4.19	Distribution of uncorrected β as function of η for cell D6 in Data.	50
4.20	Distribution of β with the distance correction (left) and the linear correction (right) as function of η for cell D6 in Data.	51
4.21	$\Delta\beta/\beta$ with β_{uncor} (left) and $\beta_{TimeCor}$ (right) as function of η in cell D6 for R -hadrons $m_{\bar{g}} = 100$ GeV...1600 GeV.	52
4.22	$\Delta\beta/\beta$ with $\beta_{DistCor}$ (left) and $\beta_{DistCor+TimeCor}$ (right) as function of η in cell D6 for R -hadrons $m_{\bar{g}} = 100$ GeV...1600 GeV.	52
4.23	$\Delta\beta/\beta$ with β_{LinCor} (left) and $\beta_{LinCor+TimeCor}$ (right)) as function of η in cell D6 for R -hadrons $m_{\bar{g}} = 100$ GeV...1600 GeV.	52
4.24	β distribution for $Z \rightarrow \mu\mu$ muon candidates in data and MC with and without DistCor + TimeCor.	53
4.25	β resolution for time corrected R -hadron candidates with and without DistCor.	53
4.26	β distribution for $Z \rightarrow \mu\mu$ muon candidates in data and MC with and without DistCor + TimeCor. For MC the nominal smearing is used.	54

4.27	The distribution of $t_{cell,uncor}$ and $t_{cell,cor}$ in cell D6 for $Z \rightarrow \mu\mu$ muons in MC (left) and data (right).	55
4.28	z_0 spread of candidate tracks.	56
4.29	β distribution for $Z \rightarrow \mu\mu$ muon candidates in data and MC with and without z_0 correction.	57
4.30	$\sigma_{t_{cell}}$ as a function of E for t_{cell} corrected and t_{cell} uncorrected.	58
4.31	$\sigma_{t_{cell}}$ as a function of E for the corrected t_{cell} with functional parametrization.	58
4.32	t_{cell} distribution for all TileCal hits in run 204932.	59
4.33	Gaussian mean of the t_{cell} distributions as a function of the runnumber.	60
4.34	Average mean of the t_{cell} distributions as a function of the runnumber.	60
4.35	β distribution for the TileCal only and with the LAr included.	61
4.36	β distribution $Z \rightarrow \mu\mu$ muons in data with the β quality requirement.	62
4.37	Cutflow for data candidates. In red the β -consistency check which is not applied in the analysis	67
4.38	Cutflow for candidates for gluino R -hadron 1300 GeV hypothesis. In red the β -consistency check which is not applied in the analysis.	68
4.39	Signal and background candidate masses in the m_β - $m_{\beta\gamma}$ -plane.	69
4.40	PDF for the β and $\beta\gamma$ in the η region $0.99 < \eta < 1.32$	70
4.41	$m_{\beta\gamma}$ distribution in data, background and signal for a 500 GeV gluino R -hadron mass hypothesis.	71
4.42	$m_{\beta\gamma}$ distribution of data, background and signal for a 500 GeV gluino R -hadron mass hypothesis.	71
4.43	β distribution for $Z \rightarrow \mu\mu$ muons for smearing scaled up and down MC and for data.	73
4.44	Systematic uncertainty on the background as a function of the mass for the gluino optimized search.	74
4.45	Estimated background, data and expected signal distribution in the m_β - $m_{\beta\gamma}$ -plane for a 1300 GeV gluino hypothesis.	75
4.46	Estimated background, data and expected signal distribution in the m_β - $m_{\beta\gamma}$ -plane for a 800 GeV sbottom hypothesis.	75
4.47	Estimated background, data and expected signal distribution in the m_β - $m_{\beta\gamma}$ -plane for a 800 GeV stop hypothesis.	76
4.48	P-value as function of the signal strength for CL_{s+b} , CL_s and CL_b in the sbottom 800 GeV signal region.	77
4.49	Limits on the cross section for the different gluino mass hypotheses as well as theoretical cross section.	79
4.50	Limits on the cross section for the different sbottom mass hypotheses as well as theoretical cross section.	79

4.51 Limits on the cross section for the different stop mass hypotheses
as well as theoretical cross section. 80

List of Tables

2.1	The particle content of the SM with mass, charge and color of the particles, taken from Ref. [5]. The anti-particles differ by opposite sign in all charge like quantum numbers.	4
2.2	The strength of the forces is only a rough estimate given in Ref. [4]. In general their strength is dependent on the distance between the sources and their nature.	12
2.3	Lifetimes of selected SM particles taken from Ref. [5].	13
4.1	Cross sections for gluino, sbottom and stop R -hadrons.	37
4.2	The $Z \rightarrow \mu\mu$ candidate selection.	38
4.3	The event selection for the MAg analysis.	63
4.4	The candidate pre-selection for the MAg analysis.	64
4.5	Tight loose and baseline selection for the production of the PDFs.	74
4.6	Summary of considered systematic uncertainties.	74

Bibliography

- [1] The ATLAS Collaboration. Searches for heavy long-lived particles with the ATLAS detector in pp collisions at $\sqrt{s} = 8$ TeV. *JHEP 01 (2015) 068*, 2015.
- [2] The ATLAS Collaboration. Observation of a new particle in the search for the Standard Model Higgs boson with the ATLAS detector at the LHC. *Phys.Lett. B716 1-29*, *arXiv:1207.7214*, 2012.
- [3] Morten Dam Jørgensen. *Exotic Long-Lived Particles*. PhD thesis, University of Copenhagen, 2014.
- [4] D. Griffiths. *Introduction to Elementary Particles*. WILEY-VCH Verlag GmbH Co. KGaA, 1987.
- [5] K. Oliv et al. (Particle Data Group). Review of Particle Physics. *Chin. Phys. C*, *38*, *090001*, 2014.
- [6] A. D. Sakharov. Violation of CP invariance, C asymmetry, and baryon asymmetry of the universe. *Journal of Experimental and Theoretical Physics 5: 24-27.*, 1967.
- [7] Planck Collaboration XIII. XIII. Cosmological parameters. *arXiv:1502.01589v2*, 2015.
- [8] G. Giacomelli, L. Patrizii. Magnetic Monopole Searches. *arXiv:hep-ex/0302011*, 2003.
- [9] S. Coleman. Q-Balls. *Nuclear Physics B 262 (2): 263*, 1985.
- [10] M. Fairbairn, A.C. Kraan, D.A. Milstaed, T. Sjöstrand, P. Skands, T. Sloan. Stable Massive Particles at Colliders. *arXiv:hep-ph/0611040v2*, 2006.
- [11] John Ellis. Beyond the Standard Model for Hillwalkers. *CERN-TH-98/329*, *arXiv:hep-ph/9812235*, 1998.

- [12] Brian R. Greene. String Theory on Calabi–Yau Manifolds. *arXiv:hep-th/9702155*, 1997.
- [13] G. Servant T. Tait. Is the Lightest Kaluza-Klein Particle a Viable Dark Matter Candidate. *ANL-HEP-PR-02-032, EFI-02-74, arXiv:hep-ph/0206071*, 2002.
- [14] The ATLAS Collaboration. Search for long-lived, heavy particles in final states with a muon and a multi-track displaced vertex in proton-proton collisions at $\sqrt{s} = 8$ TeV with the ATLAS detector. *ATLAS-CONF-2013-092*, 2013.
- [15] G.F. Giudice, A. Romanino. Split Supersymmetry. *Nucl.Phys.B699:65-89, arXiv:hep-ph/0406088*, 2004.
- [16] A M Cooper-Sarkar et al. PDF Fits at HERA. *arXiv:1112.2107*, 2011.
- [17] A.D. Martin, W.J. Stirling, R.S. Thorne, G. Watt. Parton distributions for the LHC. *Eur.Phys.J.C63:189-285, arXiv:0901.0002*, 2009.
- [18] S. Kurokawa, E. Kikutani. Overview of the KEKB accelerators. *Nuclear Instruments and Methods in Physics Research Section A. Vol. 499, Nr. 1, S. 1–7*, 2003.
- [19] H.-U. Wienands, M.E. Biagini, F.-J. Decker, M.H. Donald, S. Ecklund, A. Fisher, R.L. Holtzapple, R.H. Iverson, P. Krejcik, A.V. Kulikov, T. Meyer, J. Nelson, A. Novokhatski, I. Reichel, M. Sullivan, J.T. Seeman, J. Turner. PEP-II Status and Outlook. *Lawrence Berkeley National Laboratory*, 2011.
- [20] <https://twiki.cern.ch/twiki/bin/view/AtlasPublic/LuminosityPublicResults>, May 2015.
- [21] *LHC Design Report*. European Organization for Nuclear Research, 2004.
- [22] The ATLAS Collaboration. The ATLAS Experiment at the CERN Large Hadron Collider. *JINST 3 S08003*, 2008.
- [23] W.Beenakker, Röpker, M.Spira, P.M. Zerwas. Squark and Gluino Production at Hadron Colliders. *Nucl.Phys.B492:51-103, arXiv:hep-ph/9610490*, 1996.
- [24] B. Andersson et al. *Phys.Rept. 97 31*, 1983.
- [25] OPAL, G. Alexander et al. *Z. Phys. C69 543*, 1996.
- [26] The ATLAS Collaboration. Search for massive, long-lived particles using multitrack displaced vertices or displaced lepton pairs in pp collisions at $\sqrt{s} = 8$ TeV with the ATLAS detector. *arXiv:1504.05162v1*, 2015.

- [27] The ATLAS Collaboration. Search for charginos nearly mass-degenerated with the lightest neutralino based on a disappearing-track signature in pp collisions at $\sqrt{s} = 8$ TeV with the ATLAS detector. *Phys. Rev. D* *88*, 112006, 2013.
- [28] The ATLAS Collaboration. Search for long-lived stopped R-hadrons decaying out-of-time with pp collisions using the ATLAS detector. *Phys. Rev. D* *88*, 112003, 2013.
- [29] The ATLAS Collaboration. ATLAS Insertable B-Layer Technical Design Report. *CERN-LHCC-2010-013; ATLAS-TDR-19*, 2010.
- [30] R. D. Ryan. Precision Measurements of the Ionization Energy and Its Temperature Variation in High Purity Silicon Radiation Detectors. *IEEE Trans. Nucl. Sci. Vol. 20, Issue 1*, 473480, 1973.
- [31] The ATLAS Collaboration. dE/dx measurement in the ATLAS Pixel detector and its use for particle identification. *Tech. Rep. ATLAS-CONF-2011-016*, 2011.
- [32] The ATLAS Tile Calorimeter group. Signal Reconstruction of the ATLAS Hadronic Tile Calorimeter: implementation and performance. *Journal of Physics: Conference Series* *293* 012056, 2011.
- [33] The ATLAS Tile Calorimeter group. Time Calibration of the ATLAS Tile Calorimeter using an Integrated Laser System. *Journal of Physics: Conference Series* *219* 022015, 2010.
- [34] T. Sjostrand, S. Mrenna, and P. Skands. PYTHIA 6.4 Physics and Manual. *JHEP* *05* 026, *arXiv:hep-ph/0603175*, 2006.
- [35] A.C. Kraan. Interactions of heavy stable hadronizing particles. *Eur. Phys. J. C* *37* 91-104, *arXiv:hep-ph/0404001*, 2004.
- [36] GEANT4 Collaboration. GEANT4: A simulation toolkit. *Nucl. Instrum. Meth. A* *506* 250-303, 2003.
- [37] Schmidt M., Lipson H. Distilling Free-Form Natural Laws from Experimental Data. *Science*, Vol. *324*, no. *5923*, pp. *81 - 85.*, 2009.
- [38] Martin Spangenberg. *Calorimeter calibration and search for R-hadrons at $\sqrt{s} = 7$ TeV with the ATLAS experiment.* PhD thesis, University of Copenhagen, 2012.

- [39] The ATLAS Collaboration. Improved luminosity determination in pp collisions as $\sqrt{s} = 7$ TeV using the ATLAS detector at the LHC. *Eur.Phys.J. C* **73** 2518, *arXiv:1302.4393*, 2013.
- [40] M. Baak, G.J. Besjes, D. Cote, A. Koutsman, J. Lorenz, D. Short. HistFitter software framework for statistical data analysis. *arXiv:1410.1280 [hep-ex]*, 2014.
- [41] Glen Cowan, Kyle Cranmer, Eilam Gross, Ofer Vitells. Asymptotic formulae for likelihood-based tests of new physics. *arXiv:1007.1727*, 2010.

Danksagung

An diesem Punkt will ich einigen Leuten recht herzlich danken, die mich während meiner Masterarbeit unterstützt haben:

- Prof. Dr. Dorothee Schaile die mir die Möglichkeit geben hat an ihrem Lehrstuhl zu arbeiten
- Dr. Sascha Mehlhase für die ausgezeichnete Betreuung, das Korrektur lesen dieser Arbeit und das generell sehr angenehme Arbeitsklima in der SMP Gruppe des Lehrstuhls
- Frau Grimm-Zeidler für die Hilfe bei allen organisatorischen Fragen.
- Dr. Troels C. Petersen and Dr. Morten Dam Jørgensen for the helpful answers to questions on the previous methods used for the β estimation.
- meinen Bürokollegen Jochen Heinrich und Vincent Kitali für das angenehme Arbeitsklima und die vielen Dart Spielchen.
- allen Mitarbeitern des Lehrstuhls für die Pub Quiz Nächte, für die Grillabende, für die interessanten Diskussionen am Kaffeetisch und vieles mehr, es ist wirklich schön an diesem Lehrstuhl zu arbeiten
- meinen Eltern die mich während meines Studiums immer unterstützt haben
- und Lena Wannewetsch für die seelische und moralische Unterstützung besonders während der intensiven Zeit des Zusammenschreibens und auch für die sprachliche Korrektur meiner Arbeit.

Eigenständigkeitserklärung

Hiermit erkläre ich, Michael Adersberger, geboren am 10.12.1989 in Prien am Chiemsee, die vorliegende Arbeit mit dem Titel

**Studien zur Geschwindigkeitsmessung mit den ATLAS Kalorimetern
für die Suche nach schweren langlebigen Teilchen**

selbständig verfasst zu haben und keine anderen als die in der Arbeit angegebenen Quellen und Hilfsmittel benutzt zu haben.

München, den 22.06.2015

Michael Adersberger